

AD-A191 379

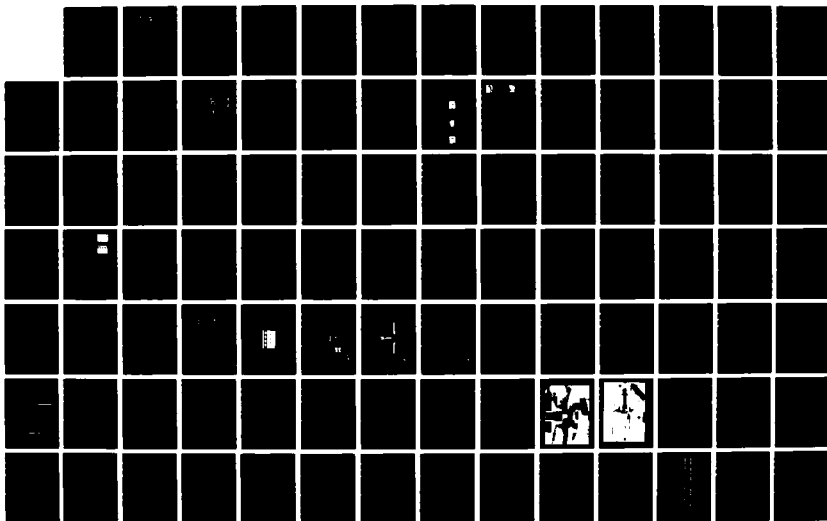
INSTRUMENTATION FOR ULTRAFAST ELECTRONICS(U) STANFORD
UNIV CA EDWARD L GINZTON LAB OF PHYSICS D M BLOOM
3 NOV 87 AFOSR-TR-88-0000 AFOSR-87-0032

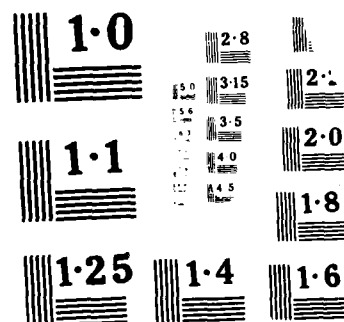
1/2

UNCLASSIFIED

F/G 9/1

ML





SECURITY CLASSIFICATION OF THIS PAGE

REPORT DOCUMENTATION PAGE

Form Approved
OMB No. 0704-0188

AD-A191 379

RT SECURITY CLASSIFICATION

DTIC
ELECTE
UNCLASSIFIED

CLASSIFICATION / DOWNGRADING SCHEDULE

FEB 25 1988

MONITORING ORGANIZATION REPORT NUMBER(S)

1b. RESTRICTIVE MARKINGS

3. DISTRIBUTION / AVAILABILITY OF REPORT

Approved for public release,
distribution unlimited

5. MONITORING ORGANIZATION REPORT NUMBER(S)

AFOSR-TR- 88-0008

NAME OF PERFORMING ORGANIZATION

Stanford University

ADDRESS (City, State, and ZIP Code)

Stanford, CA 94305

6b. OFFICE SYMBOL
(if applicable)

7a. NAME OF MONITORING ORGANIZATION

AFOSR/NE

7b. ADDRESS (City, State, and ZIP Code)

Bldg 410
Bolling AFB, DC 20332-6448NAME OF FUNDING / SPONSORING
ORGANIZATION

AFOSR

8b. OFFICE SYMBOL
(if applicable)

NE

9. PROCUREMENT INSTRUMENT IDENTIFICATION NUMBER

AFOSR-87-0032

8c. ADDRESS (City, State, and ZIP Code)

Bldg 410

Bolling AFB, DC 20332-6448

10. SOURCE OF FUNDING NUMBERS

PROGRAM
ELEMENT NOPROJECT
NOTASK
NOWORK UNIT
ACCESSION NO

61102E

2917

A3

11. TITLE (Include Security Classification)

Instrumentation for Ultrafast Electronics

12. PERSONAL AUTHOR(S)

Bloom

13a. TYPE OF REPORT

FINAL

13b. TIME COVERED

FROM 1/10/86 TO 30/09/87

14. DATE OF REPORT (Year, Month, Day)

15. PAGE COUNT

16. SUPPLEMENTARY NOTATION

17. COSATI CODES

FIELD

GROUP

SUB-GROUP

18. SUBJECT TERMS (Continue on reverse if necessary and identify by block number)

19. ABSTRACT (Continue on reverse if necessary and identify by block number)

Increasing numbers of III-V compound semiconductor devices and circuits operate in a regime where internal node testing with traditional electronic means proves impossible due to circuit loading and limited time resolution. Electrooptic sampling employs picosecond infrared laser pulses to non-invasively examine internal node voltages with 100 GHz bandwidth. Under this grant, a very low phase noise synthesizer was purchased to provide stable drive to the laser mode-locker, and a microwave synthesizer was purchased to drive the device under test up to 40 GHz. In addition, a computer aided design graphics workstation was purchased to permit the design of novel ultrafast devices. In-house design, fabrication, and detailed diagnostic testing of ultrafast III-V integrated circuits are now all possible at this unique facility.

20. DISTRIBUTION / AVAILABILITY OF ABSTRACT

☐ UNCLASSIFIED/UNLIMITED ☐ SAME AS RPT ☐ DTIC USERS

21. ABSTRACT SECURITY CLASSIFICATION

UNCLASSIFIED

22a. NAME OF RESPONSIBLE INDIVIDUAL

WITT

22b. TELEPHONE (Include Area Code)

(202) 767-4932

22c. OFFICE SYMBOL

NE

Edward L. Ginzton Laboratory
W. W. Hansen Laboratories of Physics
Stanford University
Stanford, California 94305

Final Report
to
AFOSR/DoD-URIP
on
Instrumentation for Ultrafast Electronics
Grant #AFOSR-87-0032

Covering Period: October 1, 1986 through September 30, 1987

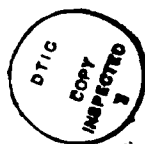
Principal Investigator:

D. M. Bloom
Associate Professor of Electrical Engineering

November 30, 1987

Table of Contents

I. Summary	3
II. Research Applications	3
III. Personnel	5
Appendix I.	6
Appendix II.	7
Appendix III.	9



Accession For
NRLS GRAM
D. C. CAR
C. C. CAR
C. C. CAR

Instrumentation for Ultrafast Electronics

I. Summary

Increasing numbers of III-V compound semiconductor devices and circuits operate in a regime where internal node testing with traditional electronic means proves impossible due to circuit loading and limited time resolution. Electrooptic sampling employs picosecond infrared laser pulses to non-invasively examine internal node voltages with 100 GHz bandwidth. Under this grant, a very low phase noise synthesizer was purchased to provide stable drive to the laser mode-locker, and a microwave synthesizer was purchased to drive the device under test up to 40 GHz. In addition, a computer aided design graphics workstation was purchased to permit the design of novel ultrafast devices. In-house design, fabrication, and detailed diagnostic testing of ultrafast III-V integrated circuits are now all possible at this unique facility.

II. Research Applications

Electrooptic sampling of high-speed GaAs circuits and devices has received increasing attention as a powerful internal-node testing technique in the microwave regime. Previous development of this system achieved bandwidths of approximately 40 GHz limited by timing instabilities in RF sources driving the laser mode-locking system. To achieve the bandwidth necessary for testing the ultrafast elements under development both here and in other laboratories, a new RF synthesizer having significantly superior phase stability was installed to drive the laser mode-locker. Having an absolute jitter of below 100 femtoseconds and significantly greater immunity to 60 Hz phase noise than a previous driver, this instrument operates in tandem with a precision phase-locked loop to stabilize the timing of the laser pulse train to better than 300 fs. Ultimate time resolution is determined by the compressed optical pulse rather than instrument weaknesses. With pulses currently 1.5 ps in width and expected to be well below a picosecond in the near future, such timing stability is critical to high-performance testing.

To apply the ultrafast measurement capabilities of the electrooptic sampler to circuits under normal operating conditions, sinusoidal microwave synthesizers are employed. Scalar and vector measurements are facilitated by the versatility and extensive features of such synthesized sweep oscillators. A computer sets the frequency of the microwave signal to be equal to a harmonic of the pulse repetition frequency of the Nd:YAG laser

offset by a small amount to walk through the signal for time-domain measurements. The high performance pulse modulator of the sweeper with short rise and fall time is used to translate the signal above the $1/f$ noise of the laser when operating in this mode. After mixing the signal down to 50 kHz, a two-channel lock-in provides a direct readout of the time waveform.

Because of low spurious and phase noise of this synthesized sweeper, high performance vector measurements can also be made. In this mode, the source is remotely controlled to set the drive frequency about 1 MHz above the multiple of the repetition rate, and then detected with a narrow band vector voltmeter configured from the same lock-in equipment used in time-domain experiments. To perform millimeter wave measurements external frequency multipliers are used in conjunction with the sweeper to extend its frequency range. Doublers have been used to make standing wave measurements to study the dispersion characteristics of uniplanar MMIC waveguides up to 40 GHz. Currently an active probe (frequency quintupler) is under development to be used in conjunction with this sweeper which would allow on-wafer measurements of millimeter wave MMIC's at W-band, 75 to 110 GHz. This will extend the vector measurement capability, including S-parameter measurements, of the electrooptic sampler into the millimeter wave region.

With such a powerful test instrument in-hand, development of specialized, novel ultrafast electronics is underway. A VAXstation 2000 GPX workstation provides the computational power and graphics interface for design of arbitrary-angle custom integrated circuits in GaAs. Subsequent mask production by an on-campus MEBES machine yields fast turnaround and .5 μm resolution. Then, facilities within the Ginzton Laboratory permit rapid custom fabrication of the unique circuits or devices. Non-linear transmission line circuits which produce 5 picosecond risetime pulses have already been fabricated in this way, as have complex test structures with 1 μm lines for characterizing the electrooptic sampler performance.

A second software package on the same host allows experimental design and modeling. Complexities in GaAs fabrication require some sort of empirical model building to achieve process reliability and optimization. RS/1, RS/Discover, and RS/Explore, from BBN Software Products Corp. provide a powerful comprehensive tool to this end. Other complex experimental systems, such as the dependencies of the electrooptic system accuracy, may also be profitably characterized in this way. A third group of software packages permits the modelling of semiconductor devices and circuits. PISCES, from Technology Modeling Associates, provides simulation of device charge profiles that can be used in designing silicon charge modulators for fiber-optic communications. Similarly, SPICE provides simulations for design of circuits like the nonlinear transmission line

described above. Together, these tools permit much more advanced research into the probing and design of novel ultrafast circuits.

III. Personnel

During the course of this project, two students were awarded degrees. Chris Madden received his M.S. Degree in Electrical Engineering in June of 1986, and Harley Heinrich received his Ph.D. in April of 1987. Dr. Heinrich's thesis was entitled "A Noninvasive Optical Probe For Detecting Electrical Signals In Silicon Integrated Circuits".

Appendix I.

Publications

October, 1986 - September, 1987

Ultrafast Electronics Laboratory

E. L. Ginzton Laboratory

Stanford University

- [1] M. J. W. Rodwell, K. J. Weingarten, D. M. Bloom, T. M. Baer, and B. H. Kolner, "Reduction of Timing Fluctuations in a Mode-Locked Nd:YAG Laser by Electronic Feedback," *Opt. Lett.* Vol. **11**, 638-640 (October 1986).
- [2] M. J. Rodwell, M. Riazat, K. J. Weingarten, B. A. Auld, and D. M. Bloom, "Internal Microwave Propagation and Distortion Characteristics of Traveling-Wave Amplifiers Studied by Electrooptic Sampling," *IEEE Trans. MTT*, Vol. **MTT-34**, (12), 1356-1361 (December 1986).
- [3] K. J. Weingarten, M. J. W. Rodwell, J. L. Freeman, S. K. Diamond, and D. M. Bloom, "Electrooptic Sampling of Gallium Arsenide Integrated Circuits," Invited paper to the 1986 Topical Meeting on Ultrafast Phenomena, Springer-Verlag (June 1986).
- [4] M. J. W. Rodwell, K. J. Weingarten, and D. M. Bloom, "Picosecond Sampling of GaAs Integrated Circuits," Invited paper to the Second Topical Meeting on Picosecond Electronics and Optoelectronics, Springer-Verlag (January 1987).
- [5] M. J. W. Rodwell, D. M. Bloom, and B. A. Auld, "Nonlinear Transmission-Line for Picosecond Pulse Compression and Broadband Phase Modulation," *Elect. Lett.* **23**, 109-110 (January 29, 1987).
- [6] K. J. Weingarten, R. Majidi-Ahy, M. J. W. Rodwell, B. A. Auld, and D. M. Bloom, "Microwave Measurements of GaAs Integrated Circuits Using Electrooptic Sampling," Invited paper to the 1987 IEEE Microwave Theory & Techniques Symposium, 1987 IEEE MTT-S International Microwave Symposium Digest, Vol. 1 (June 1987).
- [7] B. R. Hemenway, H. K. Heinrich, J. H. Goll, Z. Xu, and D. M. Bloom, "Optical Detection of Charge Modulation in Silicon Integrated Circuits Using a Multimode Laser Diode Probe," *IEEE Electron Device Letters* (August 1987).
- [8] K. J. Weingarten, M. J. W. Rodwell, and D. M. Bloom, "Picosecond Optical Sampling of GaAs Integrated Circuits," Invited paper to the special issue of *IEEE Journal of Quantum Electronics* on Ultrafast Optics and Electronics (To be published February 1988).

Appendix II.

Oral Disclosures October, 1986 - September, 1987 Stanford University

- [1] "Ultrafast Optical Electronics," Hughes Research Laboratories, Malibu, California, November 18, 1986. D. M. Bloom.
- [2] "Noninvasive Testing of Very Fast VLSI Structures," 1986 IEEE Computer Elements Workshop, Mesa, Arizona, December 2, 1986. D. M. Bloom.
- [3] "Picosecond Sampling of Integrated Circuits," Second Topical Meeting on Picosecond Electronics and Optoelectronics, Incline Village, Nevada, January 13, 1987 (Invited Paper). D. M. Bloom.
- [4] "Measurement of Charge Build Up in Resonant Tunneling Diodes," 1987 Ballistic Electrons for Transistors Conference, Santa Barbara, California, March 24, 1987. S. K. Diamond.
- [5] "Ultrafast Optical Techniques for Charge and Voltage Measurements in Semiconductor Devices and Circuits," Electrochemical Society, XEROX PARC, Palo Alto, California, April 15, 1987 (Invited talk). D. M. Bloom.
- [6] "Ultrafast Optical Techniques for Charge and Voltage Measurements in Semiconductor Devices and Circuits," 1987 Conference on Lasers and Electrooptics, Baltimore, Maryland, May 1, 1987 (Invited paper). D. M. Bloom.
- [7] "Ultrafast Optical Techniques for Charge and Voltage Measurements in Semiconductor Devices and Circuits," 31st International Symposium on Electron, Ion and Photon Beams, 1987, Woodland Hills, California, May 27, 1987 (Invited talk). D. M. Bloom.
- [8] "Microwave Measurements of GaAs Integrated Circuits Using Electrooptic Sampling," 1987 IEEE MTT-S International Microwave Symposium, Las Vegas, Nevada, June 11, 1987 (Invited talk). D. M. Bloom.
- [9] "Superlattices and Ultra High Speed Electronics," SDIO/IST Contractor Review on Reliable Advanced Electronics, Arlington, Virginia, June 16, 1987. D. M. Bloom.
- [10] "A Noninvasive Optical Probe for Detecting Electrical Signals in Silicon IC's," The Review of Progress in Quantitative Nondestructive Evaluations, Williamsburg, Virginia, June 22, 1987 (Invited paper). D. M. Bloom.
- [11] "Optical Measurements of High-Speed Devices," Meeting on Electromagnetic Simulations, Packaging and Measurements of High-Speed Devices, La Jolla, California, July 15, 1987. D. M. Bloom.
- [12] "Ultrafast Optical Techniques for Charge and Voltage Measurements in Semiconductor Devices and Circuits," 1987 Gordon Research Conference on Nonlinear Optics and Lasers, Brewster Academy, Wolfeboro, New Hampshire, July 29, 1987 (Invited talk). U. Keller.

- [13] "GaAs Integrated Circuit Testing Using Electrooptic Sampling," 11th Biennial IEEE/Cornell University Conference on Advanced Concepts in High Speed Semiconductor Devices and Circuits, Ithaca, New York, August 10-12, 1987. K. Weingarten.
- [14] "Charge Measurements of Quantum Well Devices Using a New Optical Probe," 1987 Industrial Affiliates in Solid-State Electronics, Stanford University, Stanford, California, September 17, 1987. U. Keller.
- [15] "Electrooptic Sampling of GaAs IC's Charge-Sensing Probe Silicon Light Modulators," Joint Services Electronics Program Review, Stanford University, Stanford, California, September 22, 1987. D. Bloom.

Appendix III.

Reprints and Preprints

- [1] M. J. W. Rodwell, K. J. Weingarten, D. M. Bloom, T. M. Baer, and B. H. Kolner, "Reduction of Timing Fluctuations in a Mode-Locked Nd:YAG Laser by Electronic Feedback," *Opt. Lett.* Vol. **11**, 638-640 (October 1986).
- [2] M. J. Rodwell, M. Riazat, K. J. Weingarten, B. A. Auld, and D. M. Bloom, "Internal Microwave Propagation and Distortion Characteristics of Traveling-Wave Amplifiers Studied by Electrooptic Sampling," *IEEE Trans. MTT*, Vol. **MTT-34**, (12), 1356-1361 (December 1986).
- [3] K. J. Weingarten, M. J. W. Rodwell, J. L. Freeman, S. K. Diamond, and D. M. Bloom, "Electrooptic Sampling of Gallium Arsenide Integrated Circuits," Invited paper to the 1986 Topical Meeting on Ultrafast Phenomena, Springer-Verlag (June 1986).
- [4] M. J. W. Rodwell, K. J. Weingarten, and D. M. Bloom, "Picosecond Sampling of GaAs Integrated Circuits," Invited paper to the Second Topical Meeting on Picosecond Electronics and Optoelectronics, Springer-Verlag (January 1987).
- [5] M. J. W. Rodwell, D. M. Bloom, and B. A. Auld, "Nonlinear Transmission-Line for Picosecond Pulse Compression and Broadband Phase Modulation," *Elect. Lett.* **23**, 109-110 (January 29, 1987).
- [6] K. J. Weingarten, R. Majidi-Ahy, M. J. W. Rodwell, B. A. Auld, and D. M. Bloom, "Microwave Measurements of GaAs Integrated Circuits Using Electrooptic Sampling," Invited paper to the 1987 IEEE Microwave Theory & Techniques Symposium, 1987 IEEE MTT-S International Microwave Symposium Digest, Vol. II (June 1987).
- [8] B. R. Hemenway, H. K. Heinrich, J. H. Goll, Z. Xu, and D. M. Bloom, "Optical Detection of Charge Modulation in Silicon Integrated Circuits Using a Multimode Laser Diode Probe," *IEEE Electron Device Letters* (August 1987).
- [7] M. J. W. Rodwell, C. J. Madden, B. T. Khuri-Yakub, and D. M. Bloom, "Generation of 7.8 ps Electrical Transients on a Monolithic Nonlinear Transmission Line" (Submitted to *Electronics Letters* July 20, 1987).
- [9] K. J. Weingarten, M. J. W. Rodwell, and D. M. Bloom, "Picosecond Optical Sampling of GaAs Integrated Circuits," Invited paper to the special issue of *IEEE Journal of Quantum Electronics* on Ultrafast Optics and Electronics (To be published February 1988).

Reduction of timing fluctuations in a mode-locked Nd:YAG laser by electronic feedback

M. J. W. Rodwell, K. J. Weingarten, and D. M. Bloom

Edward L. Ginzton Laboratory, Stanford University, Stanford, California 94305

T. Baer

Spectra-Physics, Inc., Mountain View, California 94039

B. H. Kolner

Hewlett-Packard Laboratories, Palo Alto, California 94304

Received May 30, 1986; accepted July 21, 1986

The timing fluctuations of a mode-locked Nd:YAG laser are reduced by electronic feedback. Timing fluctuations at rates of 50 to 250 Hz are reduced by more than 20 dB, the total timing fluctuations are reduced from 2.9 to 0.9 psec rms, and long-term drift is reduced to 0.5 psec/min. Applications include time-resolved probing experiments and synchronization of lasers.

Mode-locked laser systems in conjunction with optical-pulse compressors generate extremely short optical pulses, making these instruments attractive for time-resolved measurements of a variety of fast phenomena, including electro-optic sampling,¹ time-resolved carrier dynamics and electromagnetic transient measurements in semiconductors,²⁻⁴ measurement of optical waveforms by optical sampling,⁵ and time-resolved spectroscopy.⁶ In these experiments the system under test is pumped (excited) by the pulsed laser and subsequently probed by a delayed portion of the same optical pulse; pulse-timing fluctuations are therefore unimportant.

If excitation of the experiment with the probing laser is inconvenient or an unrepresentative experimental condition, the experiment can instead be excited by some other external source, such as a second laser or an electronic oscillator, synchronized to the pulse-repetition rate of the laser. The timing fluctuations of the laser then degrade the time resolution of the measurement and introduce noise. High scan rates can be achieved in externally synchronized experiments by introducing an offset between the excitation and probe-repetition frequencies.

Fluctuations in mode-locked Nd:YAG lasers include variations in both pulse intensity and pulse timing. If the laser produces a train of pulses described by

$$I(t) = \bar{P}T[1 + N(t)] \times \sum_{n=-\infty}^{n=+\infty} \frac{1}{\sqrt{2\pi}\sigma_t} \exp\left\{-\frac{[t - T_0 - nT - J(t)]^2}{2\sigma_t^2}\right\}, \quad (1)$$

where

$I(t)$ is the laser intensity,
 \bar{P} is the beam's average intensity,
 T is the pulse-repetition period,

σ_t is the rms pulse width,

$N(t)$ is the normalized pulse-intensity fluctuations,

$J(t)$ is the timing fluctuation of the pulse train, and

T_0 is the static timing offset of the pulse train,

then the laser intensity will have a power spectral density $S_I(\omega)$ approximated to second order in $n\omega_l\sigma_j$ by

$$S_I(\omega) \simeq \bar{P}^2 \exp(-\omega^2 \sigma_t^2) \sum_{n=-\infty}^{n=+\infty} [(1 - n^2 \omega_l^2 \sigma_j^2) \times 2\pi \delta(\omega - n\omega_l) + (1 - n^2 \omega_l^2 \sigma_j^2) S_N(\omega - n\omega_l) + n^2 \omega_l^2 S_J(\omega - n\omega_l)], \quad (2)$$

where σ_j is the standard deviation of $J(t)$ = rms timing jitter, $\omega_l = 2\pi/T$, $S_N(\omega)$ is the power spectral density of $N(t)$, and $S_J(\omega)$ is the power spectral density of $J(t)$.

Thus the spectrum of the laser intensity is a series of lines at multiples of ω_l plus spectra associated with timing and amplitude fluctuations, referred to as phase-noise sidebands [$S_J(\omega - n\omega_l)$] and amplitude-noise sidebands [$S_N(\omega - n\omega_l)$]. The jitter attenuates the pulse train's spectrum at high frequencies, as indicated by the $(1 - n^2 \omega_l^2 \sigma_j^2)$ term, and degrades the rms time resolution $\sigma_{\text{experiment}}$ of externally synchronized probing experiments:

$$\sigma_{\text{experiment}} = (\sigma_t^2 + \sigma_j^2)^{1/2}. \quad (3)$$

The phase-noise sidebands represent random fluctuations in the phase of the frequency components of the laser pulse train; in externally synchronized probing experiments the jitter introduces noise proportional to the time derivative of the experimental response.

The phase-noise sidebands, having power proportional to n^2 , predominate for harmonics of moderate

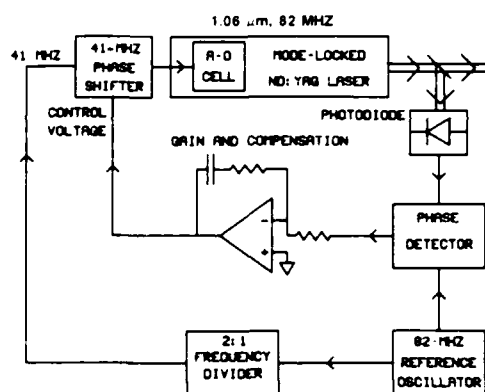


Fig. 1. System for laser-timing stabilization.

order (5–100); at higher harmonics the expansion is inaccurate both because of higher-order terms in $n\omega/\sigma_J$ and because of spectral terms associated with pulse-width fluctuations.⁷ Monitoring the laser with a photodiode and a spectrum analyzer and measuring the relative powers of the laser harmonic and its associated sidebands at some harmonic of moderate order, we can infer $S_J(\omega)$. The total jitter can then be found:

$$\sigma_J = \left[\frac{1}{2\pi} \int_{-\infty}^{+\infty} S_J(\omega) d\omega \right]^{1/2}. \quad (4)$$

Spectrum analyzers display the spectra of random signals as the noise power integrated over the analyzer resolution bandwidth. Correction factors associated with the difference between spectral densities expressed as a function of hertz rather than as a function of radian frequency, resolution bandwidths expressed by half-power bandwidth rather than by equivalent noise bandwidth, and noise measurement by envelope detection rather than by power detection must be included.⁸ Three Nd:YAG lasers tested showed jitter in the range of 2–10 psec rms, while a Rhodamine dye laser synchronously pumped by an argon-ion laser had 20-psec rms jitter.

We have reduced the pulse-timing fluctuations of a mode-locked Nd:YAG laser by using a system similar to that of Cotter⁹ (Fig. 1). A photodiode monitors the 82-MHz laser pulse train, and the phase of its 82-MHz component is compared with that of a stable reference oscillator, generating a phase error signal. The 41-MHz signal required for driving the laser's mode-locking acousto-optic (A-O) cell is generated by frequency division from the 82-MHz reference; its timing (phase) is adjusted with a voltage-controlled phase shifter controlled by the amplified and filtered phase error signal. Given an error-free phase detector and a stable-feedback loop having high loop gain, the phase of the laser pulse train will be continuously adjusted to equal the phase of the reference oscillator, suppressing the laser-timing fluctuations. Jitter suppression is limited by phase-detector spurious outputs, by reference-oscillator phase noise, and by the limited loop gain achievable in a stable-feedback loop.

Initially we used a double-balanced mixer as a simple phase detector (Fig. 2). Given a sinusoidal reference oscillator input, the phase-detector output voltage is, to first order in $N(t)$ and $J(t)$,

$$V_{\text{detector}} = k\bar{P}[1 + N(t)]T_0 + J(t) + V_{\text{os}}, \quad (5)$$

where V_{os} is the dc offset of the mixer and the subsequent amplifier. Given a feedback loop having high loop gain, V_{detector} is forced to zero, and the laser timing becomes

$$T_0 = -V_{\text{os}}/k\bar{P}, \quad (6)$$

$$J(t) = T_0 N(t). \quad (7)$$

Thus, in addition to causing timing drift with changes in mixer offset, V_{os} introduces a static phase offset T_0 , causing first-order variation in phase-detector output with variations in laser intensity, thus producing residual timing jitter. Sensitivity to laser-intensity fluctuations also results from spurious coupling of the baseband amplitude fluctuations $S_N(\omega)$ from the photodiode to the mixer output owing to finite mixer isolation. Because of these spurious outputs, the output of the phase detector within the timing stabilizer is not a reliable measure of stabilizer-jitter suppression.

An improved phase detector (Fig. 2B) suppresses mixer offset by taking the difference between successive phase measurements taken with the photodiode signal phase shifted $\pi/2$ and $-\pi/2$ rad.¹⁰ A mixer phase modulates the photodiode signal $\pm\pi/2$ rad at a 100-kHz rate. The signal is filtered, removing spurious mixer products, amplified, and applied to a second mixer serving as a phase detector. The output of the second mixer, a 100-kHz square wave whose amplitude is proportional to $J(t)$, is filtered, amplified, and synchronously detected with a third mixer. Spurious coupling of the baseband amplitude fluctuations is prevented by the 82-MHz bandpass filter. Offset voltages arising in the third (precision low-frequency) mixer and in the subsequent amplifier are small, and their relative effect is further reduced by the gain of the 100-kHz amplifier.

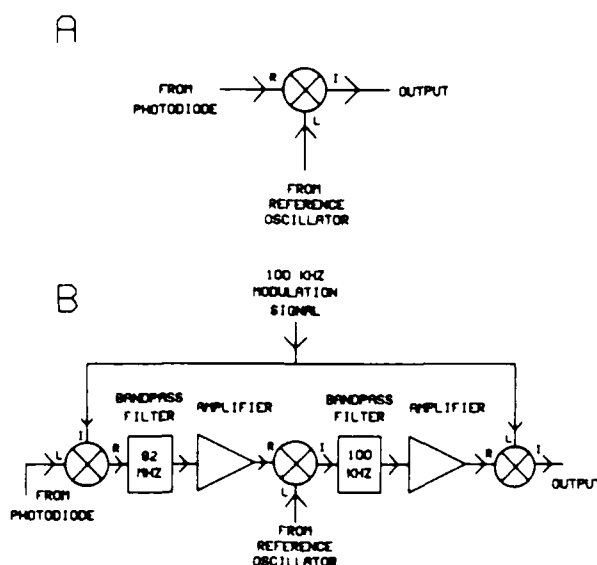
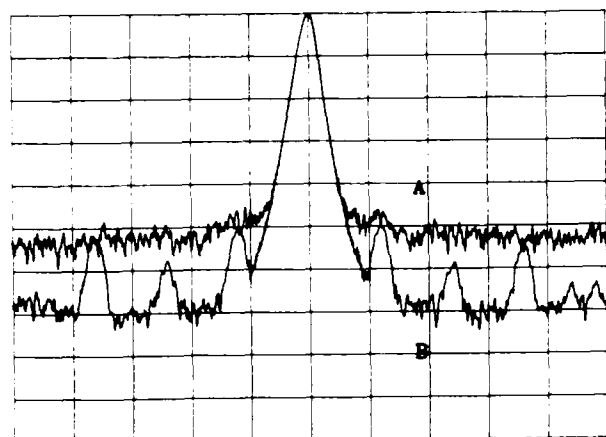
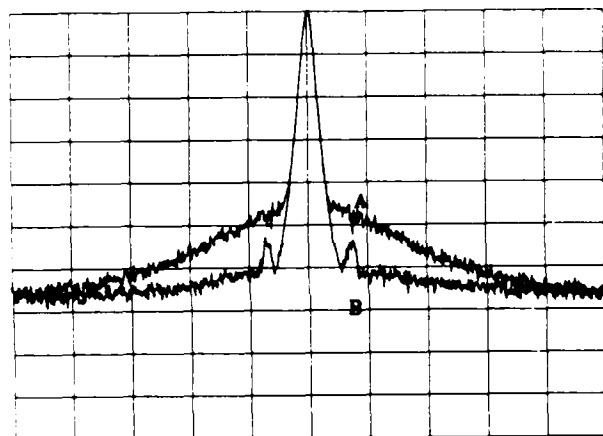


Fig. 2. Phase detectors: A, double-balanced mixer; B, chopper-stabilized mixer (R's, L's, and I's denote the mixer radio-frequency, local-oscillator, and intermediate-frequency ports).



Center 1.64 GHz 50 Hz/div. 10 Hz Resolution

Fig. 3. 0–250-Hz phase-noise sidebands at the laser's 20th harmonic: A, stabilizer off; B, stabilizer on. 10 dB per vertical division.



Center 1.64 GHz 1 kHz/div. 100 Hz Resolution

Fig. 4. 0–5-kHz phase-noise sidebands at the laser's 20th harmonic: A, stabilizer off; B, stabilizer on. 10 dB per vertical division.

Given an accurate phase measurement, the jitter suppression of the timing stabilizer is set by the gain of the feedback loop $G(\omega)$.

$$S_{\text{closedloop}}(\omega) = \left| \frac{1}{1 + G(\omega)} \right|^2 S_{\text{openloop}}(\omega), \quad (8)$$

where $S_{\text{openloop}}(\omega)$ and $S_{\text{closedloop}}(\omega)$ are the jitter spectra before and after stabilization, respectively. High $G(\omega)$, desirable at all frequencies at which $S_{\text{openloop}}(\omega)$ has significant power, is limited by stability constraints. The response of the laser phase to a step change in the phase of the driving signal is exponential with a time constant of 65 μsec , corresponding to a complex-frequency pole at 2.4 kHz. Unless compensated for, the laser pole degrades the feedback-stabilization margin. The transfer function of the gain and compensation block is an integration with an added compensating zero at 2.4 kHz, giving an overall loop gain of $G(\omega) = 2\pi(4 \text{ kHz})/j\omega$. Owing to variability in

the laser pole frequency, the compensation does not permit consistently stable operation if the frequency of unity loop gain is increased much beyond 5 kHz.

The loop's phase-noise suppression is shown in Figs. 3 and 4. In the frequency range of 500 Hz to 5 kHz the phase-noise suppression is limited by the limited loop transmission. At lower frequencies (50–250 Hz) the loop suppression is sufficient to reduce the laser's phase noise to a level limited by the reference oscillator phase noise, giving a net reduction of 20 dB. Integrating the phase-noise sidebands, we find that the total timing jitter (σ_j) is reduced from 2.9 to 0.9 psec. The small peaks in the stabilized phase-noise spectrum (Fig. 3) are power-line-induced phase-noise sidebands from the reference oscillator. Finally, long-term timing drift is stabilized to approximately 0.5 psec per minute.

In our electro-optic sampling experiments, where the signal acquisition bandwidth is between 10 and 300 Hz and the optical pulsewidth σ_t is 0.85 psec rms (2 psec FWHM), the timing stabilizer suppresses the jitter-induced noise power by 100:1 and improves the rms time resolution from 3.0 to 1.2 psec.

In summary, we have reduced the timing fluctuations of a mode-locked laser by 3.2:1 and have reduced the low-frequency phase-noise sidebands by 20 dB. Further suppression of the phase noise will require a reference oscillator having lower phase noise and will require either modification of the laser to obtain reduced prestabilization jitter or implementation of a more complex compensation scheme to permit higher loop gain over a broader frequency range.

We acknowledge the support of the U.S. Air Force Office of Scientific Research under grant number AFOSR-85-0016. M. Rodwell wishes to acknowledge an IBM fellowship.

References

1. B. H. Kolner and D. M. Bloom, *IEEE J. Quantum Electron.* **QE-22**, 79–93 (1986); J. A. Valdmanis and G. Mourou, *IEEE J. Quantum Electron.* **QE-22**, 69 (1986).
2. J. Bokor et al., in *Picosecond Electronics and Optoelectronics*, G. A. Mourou et al., eds. (Springer-Verlag, New York, 1985).
3. P. S. Panchhi and H. M. Van Driel, *IEEE J. Quantum Electron.* **QE-22**, 101–107 (1986).
4. D. H. Auston, K. P. Cheung, J. A. Valdmanis, and D. A. Kleinman, *Phys. Rev. Lett.* **53**, 1555–1558 (1984).
5. J. M. Weisenfeld, R. S. Tucker, P. M. Downey, and J. E. Bowers, *Electron. Lett.* **22**, 396–397 (1986).
6. J. A. Kash, J. C. Tsang, and J. M. Hvam, in *Picosecond Electronics and Optoelectronics*, G. A. Mourou et al., eds. (Springer-Verlag, New York, 1985).
7. J. Kluge, Ph.D. dissertation (Universität Essen, Essen, Federal Republic of Germany, 1984).
8. W. P. Robins, *Phase Noise in Signal Sources* (Peregrinus, London, 1982).
9. D. Cotter, in *Ultrafast Phenomena IV*, D. A. Auston and K. B. Eisenthal, eds. (Springer-Verlag, New York, 1984).
10. J. D. Fox and H. Schwarz, in *Digest of the 1982 IEEE Symposium on Microwave Theory and Techniques* (Institute of Electrical and Electronics Engineers, New York, 1982), pp. 334–336.

**Internal Microwave Propagation and Distortion
Characteristics of Traveling-Wave Amplifiers
Studied by Electrooptic Sampling**

M. J. W. Rodwell
M. Riazat
K. J. Weingarten
B. A. Auld
D. M. Bloom

Internal Microwave Propagation and Distortion Characteristics of Traveling-Wave Amplifiers Studied by Electrooptic Sampling

M. J. W. RODWELL, MAJID RIAZIAT, MEMBER, IEEE, K. J. WEINGARTEN, STUDENT MEMBER, IEEE,
B. A. AULD, FELLOW, IEEE, AND D. M. BLOOM, MEMBER, IEEE

Abstract—The internal signal propagation and saturation characteristics of two monolithic microwave traveling-wave amplifiers (TWA) are measured by electrooptic sampling. Gate and drain line responses are compared with theory and simulation, leading to revisions in the FET models. Drain voltage frequency dependence and harmonic current propagation together lead to more complex saturation behavior than is discussed in the literature.

I. INTRODUCTION

THE FREQUENCY RESPONSE and distortion characteristics of monolithic traveling-wave amplifiers (TWA) depend upon the propagation characteristics of microwave signals along the gate and drain transmission lines. The bandwidth and gain flatness of the amplifier are set by the finite cutoff frequencies of the periodically loaded lines, the line losses due to FET input and output conductances, and the mismatch between gate and output propagation velocities. The gain compression characteristics are set by several saturation mechanisms in the transistors, by the power at which each mechanism occurs in each FET, and by the propagation of both the amplified signal and the generated distortion products. While some of these factors are considered in the modeling and design of a TWA, the model can be verified only by measurement of the amplifier's external scattering parameters; if an amplifier does not perform to expectations, the cause is not easily identified. If the voltages at the internal nodes of the amplifier could be measured, the amplifier's characteristics would be much better understood. Such measurements are now possible using electrooptical techniques.

II. ELECTROOPTIC SAMPLING

We have developed a system for direct electrooptic sampling in GaAs integrated circuits [1]–[4]. In contrast to the external approach of Valdmanis *et al.* [5], our system,

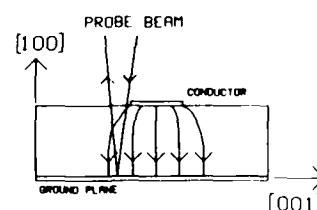


Fig. 1 Sampling geometry used for probing microstrip transmission lines.

which measures the electric-field-induced changes in polarization of picosecond pulses of subbandgap laser radiation as they pass through the GaAs substrate of the IC, can noninvasively measure the voltages at arbitrary points within the circuit. The sampler currently has a bandwidth of 80 GHz, a timing drift of 0.5 ps/min, a measured noise floor of -60 dBm (1 Hz), and a spatial resolution of 3–10 μm , depending upon the focusing lens. The sampler can be configured to emulate either a sampling oscilloscope or a network analyzer.

GaAs is electrooptic; thus, the electric fields associated with conductor voltages induce optical birefringence, causing a small change in polarization to a subbandgap optical probe beam passing through these fields. The polarization change can be detected by passing the probe beam through a polarizer and onto a photodetector. Probing geometries for measuring the voltage on microstrip and coplanar transmission lines are shown in Figs. 1 and 2, respectively.

Fig. 3 shows the sampling system. A mode-locked Nd:YAG laser is driven at 82 MHz, producing optical pulses of 1.06- μm wavelength and 100-ps duration. A fiber-grating pulse compressor reduces the pulse duration to 2 ps and a phase-lock-loop timing stabilizer reduces the laser timing jitter to 1 ps. The probe beam passes through a polarizing beamsplitter and a $\lambda/4$ waveplate whose major axis is oriented at 22.5° to the axis of the beamsplitter, producing an elliptical polarization. The ellipse major axis is aligned at 45° to the electrooptic axes of the GaAs IC substrate by a $\lambda/2$ waveplate placed between the quarter-waveplate and the circuit. The beam is focused by a $5\times$ microscope objective adjacent to or on the conductor of interest for the microstrip or coplanar geometries, respectively.

Manuscript received March 28, 1986; revised June 18, 1986. This work was supported by the Air Force Office of Scientific Research under Contract F496 20-85K-0016. M. Rodwell's research was supported by an IBM Fellowship.

M. J. W. Rodwell, K. J. Weingarten, B. A. Auld, and D. M. Bloom are with Stanford University, Edward L. Ginzton Laboratory, Stanford, CA 94305.

M. Riazat is with Varian Research Center, Palo Alto, CA 94303.
IEEE Log Number 8610555.

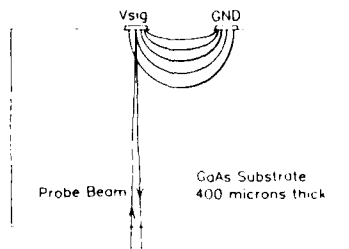


Fig. 2. Backside reflection geometry used for probing coplanar waveguide, coplanar strips, or lumped-element interconnects.

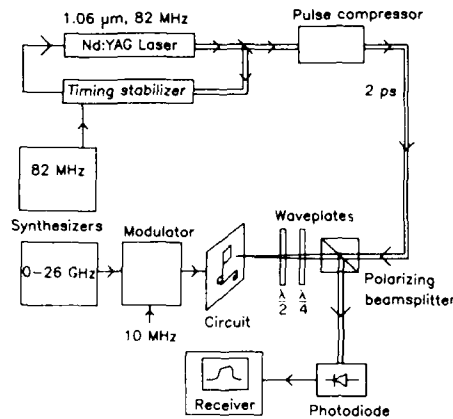


Fig. 3. Electrooptic sampling system.

The reflected beam passes back through the waveplates, producing a linear polarization rotated at 45° to the axes of the beamsplitter; the polarization component of the beam at 90° orientation is directed by the beamsplitter onto a photodiode connected to a receiver. Through the electrooptic effect, the probed conductor voltage on the IC perturbs the polarization of the returning beam, changing the intensity of the beam incident upon the photodiode.

The circuit under test is driven by a microwave synthesizer whose output is pulse modulated at 10 MHz, allowing synchronous detection with a narrow-band 10-MHz double-sideband receiver at a frequency higher than the 200 kHz $1/f$ corner frequency of the laser intensity noise. If the microwave synthesizer is tuned to exactly the N th harmonic of the laser pulse repetition frequency, the same point on the circuit waveform will be sampled every N cycles. The microwave frequency is then offset 10–100 Hz to map out the waveform at this rate. In this way, the sampler operates as a sampling oscilloscope. To use the sampler as a network analyzer, we remove the pulse modulation, offset the microwave frequency by 10 MHz, and replace the receiver with a narrow-band 10-MHz vector voltmeter. Using the sampler, we have investigated the causes of bandlimiting and gain compression in two microwave TWA's.

III. AMPLIFIERS TESTED

In a distributed amplifier, a series of small transistors are connected at regular spacings between two high-impedance transmission lines (Fig. 4). The high-impedance lines

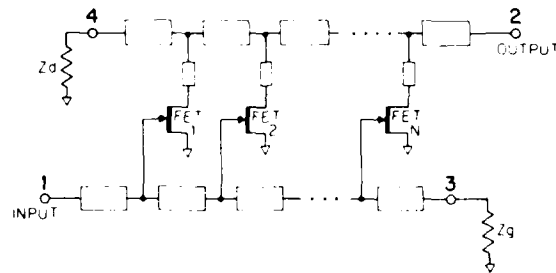


Fig. 4. Traveling-wave amplifier topology.

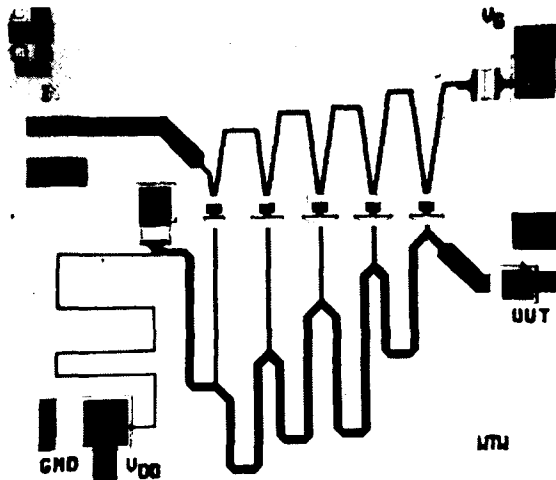


Fig. 5. 2-18-GHz TWA using microstrip transmission lines

and the FET capacitances together form synthetic transmission lines, generally of 50- Ω characteristic impedance. Series stubs are used in the drain circuit, equalizing the phase velocities of the two lines and, at high frequencies, providing partial impedance matching of the drain output impedances and thus increasing the gain. By using small devices at small spacings, the cutoff frequencies due to the periodicities of the synthetic lines can be made larger than the bandwidth limitations associated with the line attenuations arising from FET gate and drain conductances; thus, gain bandwidth products approaching f_{\max} can be attained [6]. The amplifiers studied are a five-FET TWA for 2–18 GHz that uses microstrip transmission lines (Fig. 5) and a novel five-FET TWA for 2–20 GHz designed with coplanar waveguide transmission lines [7].

IV. SMALL-SIGNAL MEASUREMENTS

By driving the TWA input with a swept-frequency sinusoid of small amplitude and then positioning the laser probe near the FET gate and drain terminals, we measure the small-signal transfer function from the input to each of these nodes, showing relative drive levels at the FET gates and output levels at the FET drains.

Packaging problems were found in testing the coplanar TWA: the amplifier chip, which showed 5.5-dB gain to 19 GHz, gave 5-dB gain to only 8 GHz when bonded to microstrip transmission lines. The long ground current path between the chip and the microstrip ground planes

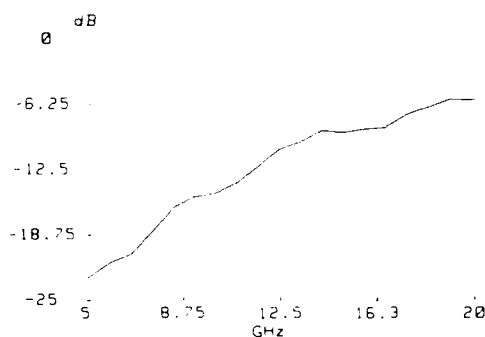


Fig. 6. Chip ground potential relative to carrier potential, as a fraction of input voltage on the coplanar TWA.

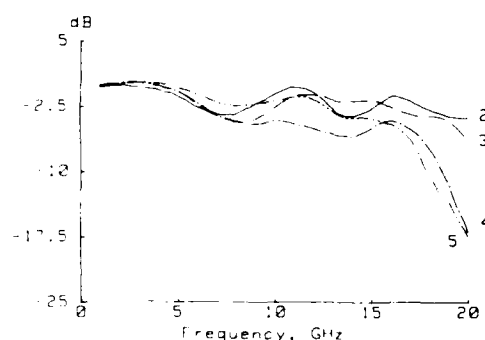


Fig. 7. Gate voltage versus frequency for the microstrip TWA, as a fraction of input voltage to amplifier; devices are numbered in order of propagation of forward wave (Gate 1 omitted for clarity.)

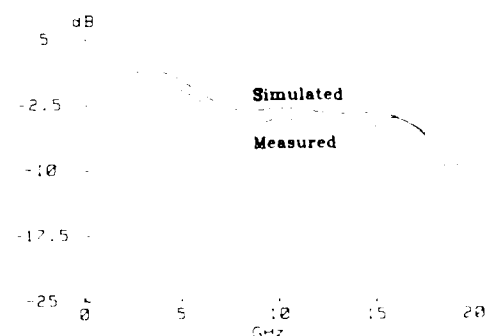


Fig. 8. Comparison between simulated and measured gate 4 voltage after adjustment of the model to obtain best fit to measurements.

was suspected; optically probing the potential between the chip and package ground planes showed that the chip ground potential is only 5 dB below the input signal at high frequency (Fig. 6), indicating substantial package ground inductance. This inductance provides feedback and thus degrades gain. A package with coplanar waveguide transmission lines gave improved performance, but has not yet been optically probed.

The microstrip amplifier provides 6-dB gain to 18 GHz, while simulation predicts 7-dB gain to 20 GHz. The gate voltage curves for this amplifier (Fig. 7) show several features: the rolloff beyond 18 GHz is the cutoff of the synthetic gate line; the slow rolloff with frequency at gates 3, 4, and 5 is gate line attenuation; and the ripples are standing waves resulting from the gate line being mis-

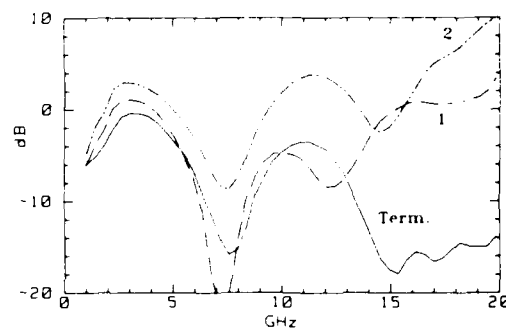


Fig. 9. Measured voltage at drain 2, drain 1, and drain reverse termination of microstrip TWA, as a fraction of input voltage.

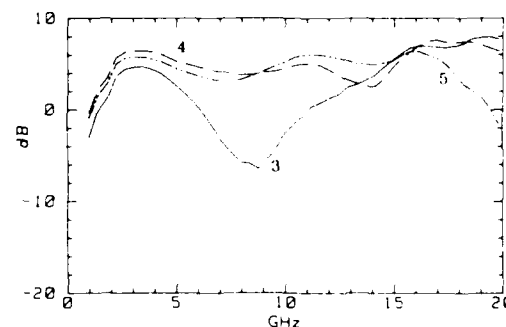


Fig. 10. Voltage versus frequency at drains 3, 4, and 5 of microstrip TWA.

terminated. These data were compared to simulations using SuperCompactTM; the simulator's optimizer was then used to adjust process-dependent circuit parameters to obtain the best fit to the measured data (Fig. 8). Model gate termination resistance increased to 80 Ω , C_{gs} increased from 1.0 to 1.14 pF/mm, C_{gd} increased from 0.03 to 0.06 pF/mm, source resistance r_s increased from 0.58 to 0.72 Ω , and source inductance decreased from 0.14 to 0.10 nH; these values fall within normal process variations. Interference between the forward and reverse waves on the drain line results in strong frequency dependence of the drain voltages (Figs. 9 and 10); this can be predicted by simple analysis.

V. DRAIN VOLTAGE DISTRIBUTION

After Ayasli [8], if the wavelength is much greater than the spacing between the FET's, the synthetic lines can be approximated as continuous structures coupled by a uniformly distributed transconductance. The lines then have characteristic impedances and phase velocities given by the sum of distributed and lumped capacitances and inductances per unit length [8]; the line impedances (Z_{og} , Z_{od}) and velocities (v_{pg} , v_{pd}) are generally made equal. The lines then have propagation constants given by

$$\gamma_g = \alpha_g + j\beta_g = \frac{r_g \omega^2 C_{gs}^2 Z_{og}}{2l} + j\omega C_{gs} v_{pg} \quad (1)$$

$$\gamma_d = \alpha_d + j\beta_d = \frac{Z_{od} G_{ds}}{2l} + j\omega C_{gd} v_{pd} \quad (2)$$

where l is the FET spacing, C_{gs} is the gate-source capaci-

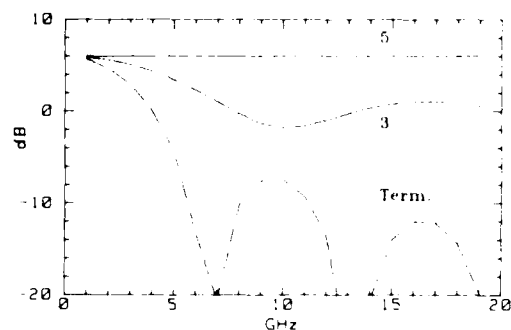


Fig. 11 Voltage versus frequency, referenced to input voltage, at drain 5, drain 3, and drain reverse termination as calculated by (4)

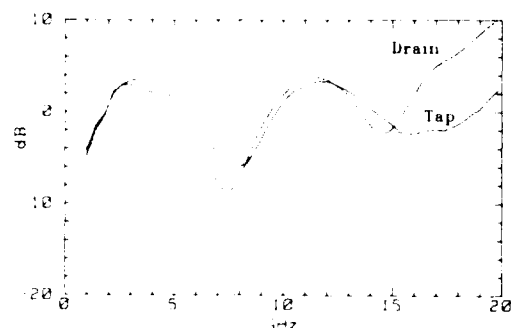


Fig. 12 Voltage versus frequency at drain 2 and at drain 2 tap point, microstrip amplifier

tance, r_g is the gate resistance, G_{ds} is the drain-source conductance, and a forward propagating wave is of the form $e^{-\gamma z}$. The voltage along the drain line is

$$V_d(z) = \frac{-g_m Z_{0d} V_{in}}{2l} \cdot e^{-\gamma_d z} \left[\frac{1 - e^{(\gamma_d - \gamma_g)z}}{\gamma_d - \gamma_g} + \frac{1 - e^{(\gamma_d + \gamma_g)(z - nl)}}{\gamma_d + \gamma_g} \right] \quad (3)$$

where n is the number of FET's, g_m is the FET transconductance, V_{in} is the input voltage, and z is the distance along the drain line, with the origin located at the drain-line reverse termination. Ignoring line attenuation, and assuming equal gate and drain phase velocities, (3) becomes

$$\|V_d(z)\| = \frac{g_m Z_{0d} V_{in}}{2l} \cdot \sqrt{z^2 + z \frac{\sin(2\beta(nl - z))}{\beta} + \frac{\sin^2(\beta(nl - z))}{\beta^2}} \quad (4)$$

which is plotted in Fig. 11. The above analysis neglects the matching effect of the series drain stubs (Fig. 4). Because these series stubs provide partial high-frequency impedance matching between the FET's and the drain transmission line, at high frequencies the drain voltages are larger than the voltages at the tap points where the drain series stubs connect to the drain line (Fig. 12). Drain-line voltage variation also arises from reflections from the drain-line reverse termination, which, owing to process variations, was 80 Ω in the device tested. We see from Fig. 11 that at

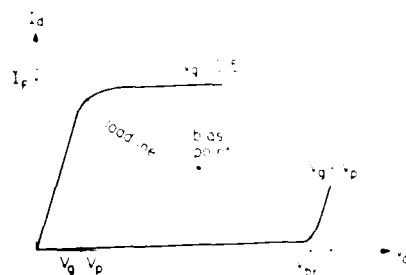


Fig. 13 FET load-line for maximum output power

high frequencies the power absorbed by the drain-line reverse termination is about 20 dB below the amplifier output power. Furthermore, at high frequencies the input power is absorbed primarily in the FET input resistances and not in the gate-line termination. Thus, at high frequencies the TWA is a directional coupler with gain. The terminations reduce the low-frequency power gain but do not waste substantial available gain near the cutoff frequency. The predicted frequency-dependent drain voltage distributions also complicate the large-signal operation of the amplifier.

VI. SATURATION MECHANISMS

The nonlinearities and power limitations in FET amplifiers include gate forward conduction, pinchoff, drain saturation, and drain breakdown. Gate forward conduction, limiting the gate voltage for linear operation to a maximum of approximately +0.5 V, thus also limits the drain current to a maximum of I_F ; the drain current at $V_{gate} = 0.5$ V. For linear operation, the gate voltage must also be more positive than the pinchoff voltage V_p and the drain voltage must be below the drain breakdown voltage V_{BR} . Finally, nonlinear operation results if the drain voltage is less than $(V_{gate} - V_p)$, the voltage necessary to pinch off the drain end of the FET channel; we refer to this as drain saturation.

In a single FET amplifier, the load-line can be chosen as in Fig. 13 so that all these limits are reached simultaneously, maximizing the output power before saturation. From this load-line, the gate and drain voltages must track in phase. Ayasli [9] and Ladbroke [10] extend this result to traveling-wave amplifiers by assuming that under appropriate design conditions (tapered gate and drain lines) the gate voltages and drain voltages of all FET's can be made equal, thus causing all devices to saturate simultaneously. In the case where gate and drain losses can be neglected, we can show that if the drain and gate synthetic lines have characteristic impedances Z_{0d} and Z_{0g} and phase velocities v_{pd} and v_{pg} of the form

$$\begin{aligned} Z_{0d}(z) &= K_1 z \\ Z_{0g}(z) &= Z_0 \\ v_{pd}(z) &= v_{pg}(z) = v_p \end{aligned} \quad (5)$$

and if the drain-line reverse termination is omitted and the output load resistance Z_{load} set at

$$Z_{load} = K_1 nl \quad (6)$$

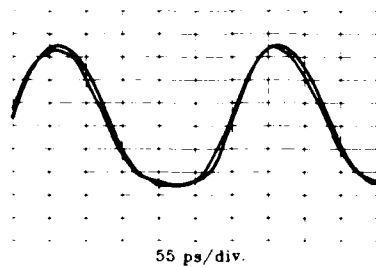


Fig. 14 Saturation at drains 4 and 5 of microstrip TWA, 3-GHz, 7-dBm input power

then the voltage along the drain line will be uniform as follows:

$$V_d(z) = -ng_m Z_{\text{load}} I_{\text{in}} e^{-j\omega z/v_d} \quad (7)$$

The drain-line voltage is uniform and in phase with the gate-line voltage, allowing simultaneous saturation of all FET's and thus maximizing the output power at saturation.

In the uniform drain-line case, as is shown by (3) and by Figs. 9 and 10, the reverse wave on the drain line complicates the problem; the drain voltages are equal only at low frequencies, and, by (3), the reverse wave introduces a phase shift between the gate and drain voltages of each FET. Thus, in the uniform drain line case, neither the conditions for simultaneous saturation of all FET's nor the conditions for simultaneously reaching all saturation mechanisms in a given FET can be met.

The 2-18 GHz microstrip amplifier has 1-dB gain compression at 7-dBm input power, and is not optimized for maximum power output; the lines are not tapered in the form of (5) and the bias is not set for maximum uncompressed output power. Ignoring for a moment the frequency dependence and position dependence of the gate and drain voltages, we can estimate the gain compression point and identify the predominant saturation mechanism. With a gate bias voltage V_{G0} of -0.3 V, a drain bias voltage V_{D0} of 3.5 V, a pinchoff voltage of approximately -2 V, and an amplifier voltage gain of $A_i = -2$ (6 dB), the gate signal is $\delta V_{\text{gate}} = \delta V_{\text{drain}}/A_i$, and the maximum negative drain voltage excursion is limited by drain saturation to $\delta V_{\text{drain}} = (V_{D0} - V_{G0} - \delta V_{\text{gate}} + V_p) = -1.2$ V, corresponding to 11.5-dBm output power. With 6-dB amplifier gain, drain saturation will thus occur at input power levels of approximately 5.5 dBm, while the maximum input voltage before gate forward conduction occurs is $\delta V_{\text{gate}} = (0.5 - V_{G0}) = 0.8$ V, corresponding to 8-dBm input power. As pinchoff and drain breakdown occur only at still higher input powers, the maximum power output of the amplifier is thus limited by drain saturation. Probing the drain and gate large-signal voltage waveforms with the amplifier driven at its 1-dB gain compression power, we observe no clipping of the gate voltage waveforms (which would arise from gate forward conduction), but observe clipping of the negative excursions of the drain voltage waveforms; the clipping resulting from drain saturation. Adjustment of the gate bias V_{G0} to 0 V results in significant gate forward

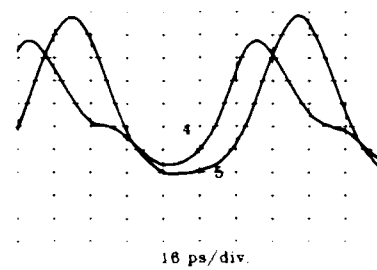


Fig. 15 Saturation at drains 4 and 5 of microstrip TWA, 10-GHz, 7-dBm input power

conduction at 7-dBm input power, and clipping of the positive excursions of the gate voltage waveforms was observed; subsequent tests were performed with the amplifier biased normally ($V_{G0} = -0.3$ V), where gain compression is dominated by drain saturation.

At 3 GHz, the small-signal voltages at the drains of the last two devices are approximately equal, and are larger than the small-signal voltages at drains 1, 2, and 3 (see Figs. 9 and 10). Thus, clipping occurs simultaneously at drains 4 and 5 (Fig. 14). Because of the smaller voltage swings at drains 1, 2, and 3, these devices show strong drain saturation only at input power levels several decibels larger than the input power necessary to cause drain saturation in the fourth and fifth FET's.

At 10 GHz, the distortion at the 1-dB compression point is complicated by phase shifts between the 10-GHz fundamental and the 20-GHz generated harmonic currents (Fig. 15). The 10-GHz small-signal voltage at drain 5 is 1.5 dB larger than that at drain 4; thus, FET 5 saturates more strongly. As with the 3-GHz saturation characteristics, the 10-GHz small-signal voltages at drains 1, 2, and 3 are comparatively small, and thus the first three transistors do not show significant saturation at 1-dB gain compression. The 20-GHz harmonic current generated at FET 5 produces equal forward and reverse drain voltage waves at 20 GHz. With 10-ps line delay between drains 4 and 5, the 20-GHz reverse wave from FET 5 undergoes 20-ps relative phase delay (which is 72° of a 10-GHz cycle) before combining with the 10-GHz forward wave at drain 4. The resulting voltage waveform at drain 4 would then approximate a sawtooth function; drain saturation at FET 4 then clips the peak negative excursion. Depending upon the line delay between successive drains, the reverse-propagating harmonic currents can either increase or decrease the peak voltages at other drains, increasing or decreasing the saturation at prior devices.

At 18 GHz, the small-signal drain voltage at drain 4 is larger than that at drain 5. Thus, at the 1-dB gain compression point, FET 4 will saturate strongly while FET 5 will show only weak drain saturation. At this frequency, FET's 2 and 3 have small-signal drain voltages that are 0.5-1 dB smaller than at drain 4, and thus also show significant drain saturation. The 36-GHz harmonic currents generated at drain 4 are beyond the cutoff frequency of the synthetic drain line; the generated 36-GHz forward wave thus experiences significant dispersion and attenuation relative to

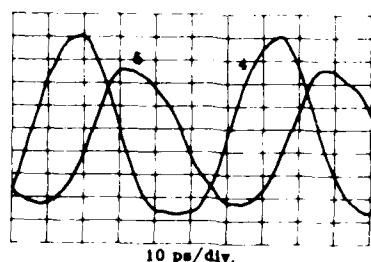


Fig. 16 Saturation at drains 4 and 5 of microstrip TWA, 18 GHz, -7-dBm input power

the 18-GHz forward wave as the two waves propagate towards drain 5 and the output. The voltage waveform at drain 5 is thus visibly distorted, but the phase relationship between the fundamental and the distortion components has been shifted, and the waveform no longer clearly reflects the drain saturation waveform observed at drain 4 (Fig. 16).

VII. CONCLUSIONS

We have studied the propagation of signals internal to microwave distributed amplifiers with electrooptic sampling. Gate-line attenuation and cutoff is observed, as is interference of the forward and reverse wave on the drain lines, both as predicted by theory. Using a microwave simulation program, the circuit models can be adjusted to obtain a fit between simulated and measured internal node voltages, allowing detailed circuit diagnostics. Large-signal saturation characteristics of the amplifier are set by both the order of occurrence of each saturation mechanism in each FET, and by the propagation of the generated harmonic currents through the circuit.

ACKNOWLEDGMENT

The authors wish to thank G. Zdasiuk and C. Yuen of Varian Associates for their assistance. They also thank A. Macfarlane for typesetting the manuscript.

REFERENCES

- [1] B. H. Kolner and D. M. Bloom, "Electro-optic sampling in GaAs integrated circuits," *IEEE J. Quantum Electron.*, vol. QE-22, pp. 79-93, Jan. 1986.
- [2] K. J. Weingarten, M. J. W. Rodwell, H. K. Heinrich, B. H. Kolner, and D. M. Bloom, "Direct electro-optic sampling of GaAs integrated circuits," *Electron. Lett.*, vol. 21, pp. 765-766, 1985.
- [3] J. L. Freeman, S. K. Diamond, H. Fong, and D. M. Bloom, "Electro-optic sampling of planar digital integrated circuits," *Appl. Phys. Lett.*, vol. 47, pp. 1083-1084, 1985.
- [4] M. J. W. Rodwell, K. J. Weingarten, J. L. Freeman, and D. M. Bloom, "Gate propagation delay and logic timing of GaAs integrated circuits measured by electro-optic sampling," *Electron. Lett.*, vol. 9, pp. 501-502, 1986.
- [5] J. A. Valdmanis, G. A. Mourou, and C. W. Gabel, "Subpicosecond electrical sampling," *IEEE J. Quantum Electron.*, vol. QE-19, pp. 664-667, Apr. 1983.
- [6] J. B. Bever, S. N. Prasad, R. C. Becker, J. F. Nordman, and G. K. Hohenwarter, "MES-FET distributed amplifier design guidelines," *IEEE Trans. Microwave Theory Tech.*, vol. MTT-32, pp. 268-275, Mar. 1984.
- [7] M. Riazat, I. Zubeck, S. Bandy, and G. Zdasiuk, "Coplanar waveguides used in 2-18 GHz distributed amplifier," in *Tech. Dig.*, 1986 *IEEE MTT-S Int. Microwave Symp.*, pp. 337-338, 1986.
- [8] Y. Avash, R. I. Mozzi, J. L. Vorhaus, I. D. Reynolds, and R. A. Pucel, "A Monolithic GaAs 1-13 GHz traveling-wave amplifier," *IEEE Trans. Microwave Theory Tech.*, vol. MTT-30, pp. 976-981, July 1982.
- [9] Y. Avash, I. D. Reynolds, R. I. Mozzi, and R. K. Hanes, "2-20 GHz GaAs traveling-wave power amplifier," *IEEE Trans. Microwave Theory Tech.*, vol. MTT-32, pp. 290-295, Mar. 1984.
- [10] P. H. Tadbroke, "Large-signal criteria for the design of GaAs FET distributed power amplifiers," *IEEE Trans. Electron Devices*, vol. ED-32, pp. 1745-1748, Sept. 1985.



transmission systems



high speed electronic testing and ultrafast optical pulse generation

M. J. W. Rodwell was born on January 18, 1960, in Altrincham, England. He received the B.S. degree in electrical engineering from the University of Tennessee, Knoxville, in 1980, and the M.S.E.E. degree from Stanford University, Stanford, CA, in 1982. Currently, he is a Ph.D. student in electrical engineering at Stanford, pursuing research in picosecond optics and electronics.

From 1982 through 1984, he worked at AT&T Bell Laboratories, designing fiber-optic digital

Majid Riazat (M'84) received the B.S. degree in engineering physics from the University of Oklahoma, Norman, Oklahoma, in 1978 and the M.S. and the Ph.D. degrees in applied physics from Stanford University, Stanford, California, in 1980 and 1983, respectively.

In 1984, he joined Varian Research Center in Palo Alto, CA, where he is currently a Senior Engineer involved in MMIC design and microwave measurements research.

K. J. Weingarten (S'86) was born January 30, 1961 in St. Petersburg, FL. He received the B.S. degree in electrical engineering from the Georgia Institute of Technology, Atlanta, GA, in 1983 and the M.S. degree in electrical engineering from Stanford University, Stanford, CA, in 1985. He is currently a Ph.D. candidate in electrical engineering at Stanford.

He works as a research assistant in the Edward T. Ginzton Laboratory. His research interests are electrooptic sampling of GaAs ICs, high speed electronic testing, and ultrafast optical pulse generation.



B. A. Auld (S'49, A'53, M'58-F'73) was born on November 4, 1922, in Wei-Hwei-Fu, China. He received the B.S. degree in electrical engineering from the University of British Columbia in 1946 and the Ph.D. degree in electrical engineering from Stanford University, Stanford, CA, in 1952.

In 1958, he joined the Edward L. Ginzton Laboratory, W. W. Hansen Laboratories of Physics, Stanford University, where he is currently a Professor of Applied Physics (research). His research activities have been concerned with

electromagnetic and acoustic waves. Upon joining the staff at Edward L. Ginzton Laboratories, he worked on the application of nonlinear analysis to microwave ferrite problems, primarily with regard to parametric instabilities, harmonic generation, nonlinear resonance, and shock-wave propagation. In more recent years, he has been involved with microwave acoustics and acoustic imaging.

Dr. Auld was awarded the 1959 IRE Microwave Prize for a paper on symmetrical ferrite circulators. In 1983, he was awarded the IEEE Ultrasonic Achievement award for scientific excellence and distinction through contributions to ultrasonics.



D. M. Bloom (S'68, M'76, M'80) was born on October 10, 1948, in Brooklyn, NY. He received the B.S. degree in electrical engineering from the University of California Santa Barbara in 1970 and the M.S. and the



Ph.D. degrees in electrical engineering from Stanford University in 1972 and 1975, respectively.

From 1975 to 1977, he was employed by Stanford University as a Research Associate. During this period, he was awarded the IBM Postdoctoral Fellowship. From 1977 to 1979, he was employed by Bell Telephone Laboratories, Holmdel, NJ, where he conducted research on optical phase conjugation, ultrafast optical pulse propagation in fibers, and tunable color-center lasers. From 1979 to 1983, he served on the staff and later as a Project Manager at Hewlett Packard Laboratories, Palo Alto, CA. While at Hewlett Packard, he conducted and managed research on fiber-optical devices, high-speed photodetectors, and picosecond electronic measurement techniques. In late 1983, he joined the Edward L. Ginzton Laboratory, W. W. Hansen Laboratories of Physics, Stanford University, where he is currently an Associate Professor of Electrical Engineering. His current research interests are ultrafast optics and electronics.

He was awarded the 1980 Adolph Lomb Medal of the Optical Society of America for his pioneering work on the use of nonlinear optical processes to achieve real time conjugate wavefront generation. In 1981, he was elected a Fellow of the Optical Society of America in recognition of his distinguished service in the advancement of optics. He is the 1985 IEEE LEOS traveling lecturer.

Electrooptic Sampling of Gallium Arsenide Integrated Circuits

K.J. Weingarten, M.J.W. Rodwell, J.L. Freeman, S.K. Diamond, and D.M. Bloom

Stanford University, Edward L. Ginzton Laboratory
Stanford, California, 94305

1. Introduction

As GaAs integrated circuits (IC's) grow in speed and complexity, new methods to accurately measure the internal node response of these circuits are required. Sampling oscilloscopes have a 25 ps risetime and network analyzers can measure linear response to 100 GHz. However, both instruments load the test point with $50\ \Omega$ limiting their use to input or output ports. Electrooptic sampling was pioneered [1],[2],[3] to measure optoelectronic devices (photoconductors and photodetectors) with response times shorter than a sampling oscilloscope's resolution. To address the need to test internal nodes we have developed an electrooptic sampling system for probing signals directly within a GaAs IC [4].

2. Electrooptic Sampling System

Gallium arsenide is electrooptic; the electric fields from conductor voltages induce optical birefringence, causing a change in polarization to a suitably polarized probe beam passing through these fields. The polarization change can be detected by passing the probe beam through a polarizer and onto a photodetector. For the longitudinal probing geometry the change in intensity of the received beam is linearly proportional to the voltage [4] across the substrate at the test point. Probing geometries for measuring the voltage on various conductor types are shown in Fig. 1 [5],[6].

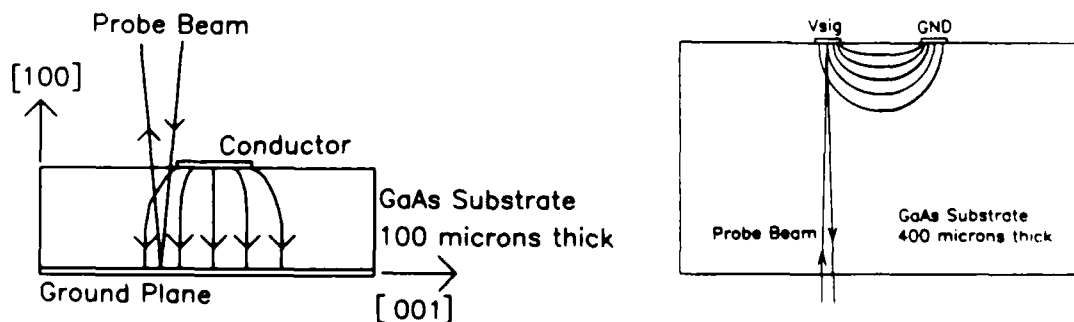


Figure 1: Cross sections of sampling geometries. Frontside (left) for probing microstrip transmission lines and backside (right) for planar transmission lines and wire interconnects

Figure 2 shows the sampling system schematic. A mode-locked Nd:YAG laser is driven at 82 MHz, producing optical pulses of $1.06\text{ }\mu\text{m}$ wavelength and 100 ps pulsewidth. A fiber-grating pulse compressor reduces the pulse duration to 2 ps [7] and a phase-lock-loop timing stabilizer reduces the laser timing jitter to 1 ps [8]. The probe beam passes through a polarizing beamsplitter and a $\lambda/4$ waveplate producing elliptically polarized light with its major axis 22.5° to the beamsplitter axes. A $\lambda/2$ waveplate rotates the axes of ellipse to 45° from the electrooptic crystal axes of the substrate. A microscope objective focuses the beam through the substrate adjacent to or on the conductor of interest for frontside or backside probing, respectively. The reflected light passes back through the waveplates and beamsplitter, producing linearly polarized light at 45° to the beamsplitter axes. The polarization component reflected from the beamsplitter is directed onto a photodiode connected to a receiver. The beam intensity at the photodiode varies linearly with the voltage on the conductor [4].

The system can be configured to emulate either a sampling oscilloscope or a network analyzer. To emulate a sampling oscilloscope, the microwave synthesizer is set to an exact multiple of the laser pulse repetition rate plus some small frequency offset, typically 10-100 Hz. The received intensity then varies in proportion to the signal voltage at this offset frequency. To improve the signal to noise ratio, the microwave signal is also pulse modulated at 10 MHz for synchronous detection. To use the sampler

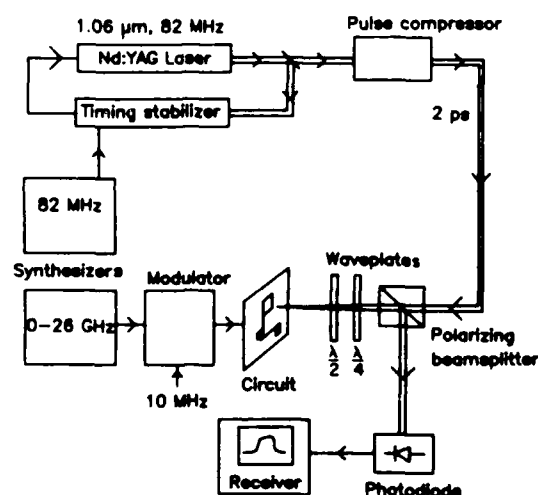


Figure 2: Schematic of the electrooptic sampler

as a network analyzer, we remove the pulse modulation, offset the microwave frequency by 10 MHz and use a narrowband 10 MHz vector voltmeter.

The measurement bandwidth is set by the optical pulsewidth and the pulse-to-pulse timing jitter. The pulsewidth is measured with an optical autocorrelator; however, this does not uniquely determine the pulseshape. A more useful measure of the pulse's frequency content is the Fourier transform of its autocorrelation, the power spectral density (PSD) [9]. The compressed pulse autocorrelation, with a FWHM of 2 ps, has a -3 dB point of 100 GHz, slightly less than that of an ideal 2 ps FWHM gaussian pulse.

The timing jitter degrades the system performance in two ways, increasing the noise floor and decreasing the measurement bandwidth [8]. However, using a phase-lock-loop to stabilize the laser timing with respect to a stable microwave synthesizer, the r.m.s. jitter has been reduced to less than 1 ps with long term drift of about 0.5 ps/minute.

3. Circuit Applications

Since the sampling system can emulate either a sampling oscilloscope or a network analyzer, it is ideally suited for circuit measurements on GaAs IC's. Signal timing, risetimes, and propagation delays on a number of digital circuits have been measured [6],[10]. On an 8-bit multiplexer clocked at 2.6 GHz [11], signals on interconnects as narrow as $2\text{ }\mu\text{m}$ and the bottom of air bridge posts were measured, including the serial output word of the MUX and the timing of the 8-phase clock. To measure propagation delays, a test structure consisting a string of 20 inverters for average gate delay measurements with conventional electronics [12] was probed. By switching the first inverter with a microwave synthesizer at gigahertz rates, a repeating square wave rippled through the inverter chain. The probe beam was then positioned at nodes in the circuit to measure the delays between inverters and between the FET's internal to individual inverters (see Fig. 3).

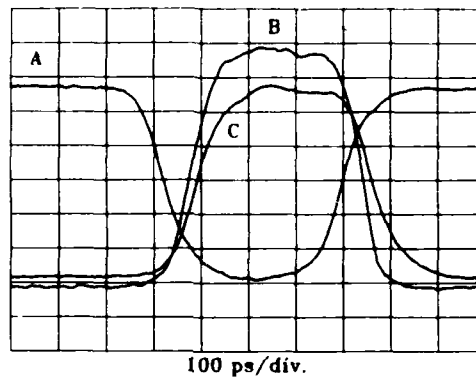


Figure 3: Propagation delays through one inverter of the 20-inverter test structure. A: Drive signal from previous inverter B: Delay through inverting FET, 60 ps C: Delay through buffer FET and diode-level shifters, 15 ps

More recently the system has been applied to the extensive characterization of microwave amplifiers [13]. Using the sampler in the network analyzer mode, the small-signal response at internal nodes was measured (see Fig. 4). Comparing the measured data to the simulated data, the process-dependent circuit parameters were modified to obtain a best-fit. Modeled gate termination resistance increased from $50\text{ }\Omega$ to $80\text{ }\Omega$, and the devices' f_r decreased by 14%, for example. The large-signal, saturation behaviour of the amplifiers was studied using the system as a sampling oscilloscope. Harmonic distortion at fundamental frequencies as high as 21 GHz was observed.

In the network analyzer mode the sampler measures the vector voltage on the IC. A network analyzer, however, measures the forward and reverse traveling waves. By measuring the voltage along a conductor, the forward and reverse traveling waves can be calculated. Figure 5 shows an example of such a measurement on a transmission line with two different load terminations. For a line terminated in its characteristic impedance, the magnitude is constant and the phase varies linearly with slope β , the wavenumber, while for a perfect short or open, the magnitude varies sinusoidally. From this data the reflection coefficient, loss, and dispersion can be calculated. Scanning perpendicular to the conductor allows for measurement of the potential distribution (Fig. 6). Note that the potential drops off in roughly the distance of substrate thickness, $350\text{ }\mu\text{m}$, as expected. The phase shift near the edge of the substrate is evidence of coupling of the guided wave to higher-order leaky modes.

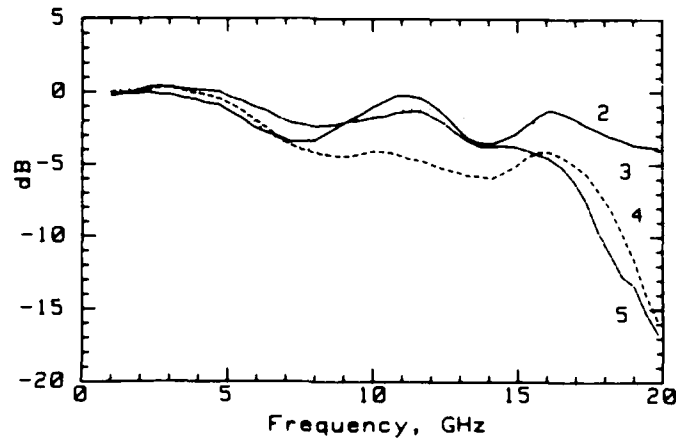


Figure 4: Small-signal voltage frequency response at the gates of a 5-FET distributed amplifier (gate 1 omitted for clarity)

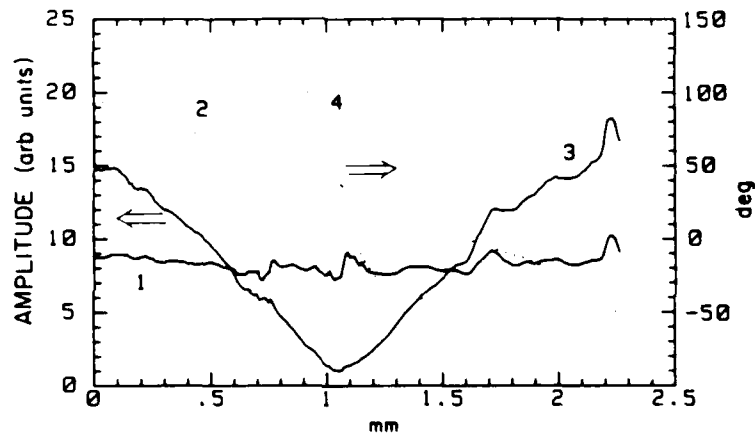


Figure 5: Length scan of microstrip transmission line for two load terminations at 16 GHz drive frequency: 1) magnitude and 2) phase with $50\ \Omega$ termination, 3) magnitude and 4) phase with short termination

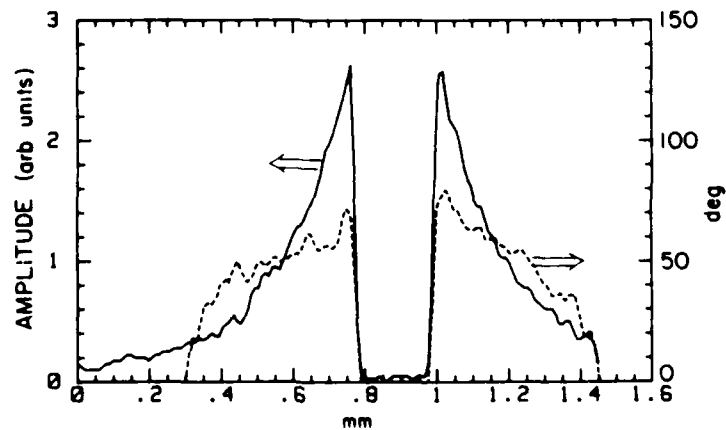


Figure 6: Width scan of microstrip transmission line at 31 GHz drive frequency. The conductor width is $220\ \mu\text{m}$ and the substrate thickness $350\ \mu\text{m}$. The phase delay near the edge of the substrate is evidence of coupling to radiative modes

4. Conclusion

We have described an electrooptic sampling system designed for making ultrafast measurements on GaAs IC's. The system has a measurement bandwidth of 80 GHz, a timing drift of less than 1 ps, a noise floor of 300 μ V (1 Hz), and a spatial resolution of 2 μ m. Using the system as either a sampling oscilloscope or a network analyzer, we have measured signal timing, risetimes, and propagation delays in digital circuits with picosecond resolution, frequency response and harmonic distortion in microwave amplifiers to 20 GHz, and standing waves, propagation constants, and potential distributions of transmission lines to 40 GHz. The technique has a potential bandwidth extending past the millimeter-wave range (300 GHz), and future use of this system will concentrate on the study of new ultrafast GaAs circuits and devices.

5. Acknowledgements

The authors wish to thank Majid Riazat of Varian Associates, Steve Swierskowski of Lawrence Livermore National Laboratory, and K. Reed Gleason of TriQuint Semiconductor for their invaluable assistance with their GaAs IC's. This work was supported by the Air Force Office of Scientific Research under contract number F49620-85K-0016. M. Rodwell, J. Freeman, and S. Diamond wish to acknowledge IBM fellowships.

6. References

1. J.A. Valdmanis, G. A. Mourou, and C.W. Gabel, IEEE J. Quant. Elec., **19**, 664 (1983)
2. B.K. Kolner, D.M. Bloom, and P.S. Cross, Elect. Lett., **19**, 574 (1983)
3. J.A. Valdmanis and G. Mourou, IEEE J. Quant. Elec., **22**, 69, (1986)
4. B.H. Kolner and D.M. Bloom, IEEE J. Quant. Elec., **22**, 79 (1986)
5. K.J. Weingarten, M.J.W. Rodwell, H.K. Heinrich, B.H. Kolner, and D.M. Bloom, Electron. Lett., **21**, 765 (1985)
6. J.L. Freeman, S.K. Diamond, H. Fong, and D.M. Bloom, Appl. Phys. Lett., **47**, 1083 (1985)
7. J.D. Kafka, B.H. Kolner, T.M. Baer, and D.M. Bloom, Optics Lett., **9**, 505 (1984)
8. M.J.W. Rodwell, K.J. Weingarten, D.M. Bloom, T. Baer, and B.H. Kolner, *submitted to Optics Letters*.
9. R.N. Bracewell, *The Fourier Transform and its Applications*, McGraw-Hill, New York 1978
10. M.J.W. Rodwell, K.J. Weingarten, J.L. Freeman, and D.M. Bloom, Electron. Lett., **22**, 499 (1986)
11. G.D. McCormack, A.G. Rode, and E.W. Strid, Proc. 1982 GaAs IC Symp., pp. 25-28
12. S. Swierkowski, K. Mayeda, and C. McGonaghy, Technical Digest, 1985 International Electron Devices Meeting, pp. 272-275
13. M.J.W. Rodwell, M. Riazat, K.J. Weingarten, B.A. Auld, and D.M. Bloom, Technical Digest, 1986 IEEE MTT-S International Microwave Symp., pp. 333-336

Picosecond Sampling of GaAs Integrated Circuits

K. J. Weingarten, M. J. W. Rodwell, and D. M. Bloom

Edward. L. Ginzton Laboratory
Stanford University
Stanford, CA 94305

1. Introduction

Gallium Arsenide (GaAs) microwave integrated circuits (IC's) are now being developed for operation in the millimeter-wave range, while GaAs digital IC's have demonstrated ring-oscillator propagation delays of 5-10 ps, with gate delays of 50-100 ps for larger scale circuits. Digital IC's are currently tested only by indirect techniques (multi-stage propagation delay or cycle times), while microwave circuits are tested by external scattering parameter measurement; if the circuit does not perform to expectations, the cause is not easily identified. Electrooptic sampling was initially developed to measure the response of photoconductors and photodetectors faster than the time resolution of sampling oscilloscopes and used an external electrooptic modulator connected to the device under test [1,2]. The system developed at Stanford uses the GaAs IC substrate as the electrooptic material, permitting detailed internal-node circuit evaluation with picosecond time resolution.

2. The Sampling System

GaAs is electrooptic; the electric fields associated with conductor voltages induce optical birefringence, causing a polarization change to a probe beam passing through these fields. Figure 1 shows the standard probing arrangements. For standard [100] cut GaAs substrates the probe beam is effected by the longitudinal field components. Passing the reflected light through a polarizer results in a change in intensity proportional to the voltage across the substrate at the probe point [3]. For frontside probing, the fields extend from the conductor roughly the distance of the substrate thickness and the probe spot size is set to approximately one-tenth of the substrate thickness to accurately measure the conductor potential. For backside probing, the characteristic extent of the fields into the substrate is the distance between the signal conductor and the ground; the substrate thickness must be much greater than the signal-ground spacing and the probe spot size should be less than or equal to the conductor width.

The sampling system is shown schematically in Fig. 2. A Nd:YAG laser produces 1.06 μm , 90 ps pulses at an 82 MHz rate. The laser has free-running pulse-to-pulse timing fluctuations of 4 ps rms, reduced to less than 0.5 ps rms by a feedback system [4]. A fiber-grating pulse compressor shortens the pulses to 1.5 ps FWHM. The beam passes through a polarizing beamsplitter and two waveplates, then is focused through the IC substrate with a microscope objective to a 3 μm spot on the probed conductor (backside probing) or a 10 μm spot on the ground plane adjacent to the probed conductor (frontside probing). The reflected light is analyzed by the polarizing beamsplitter; the change in intensity is proportional to the voltage across the GaAs substrate [2] and is detected by a photodiode connected to a vector receiver.

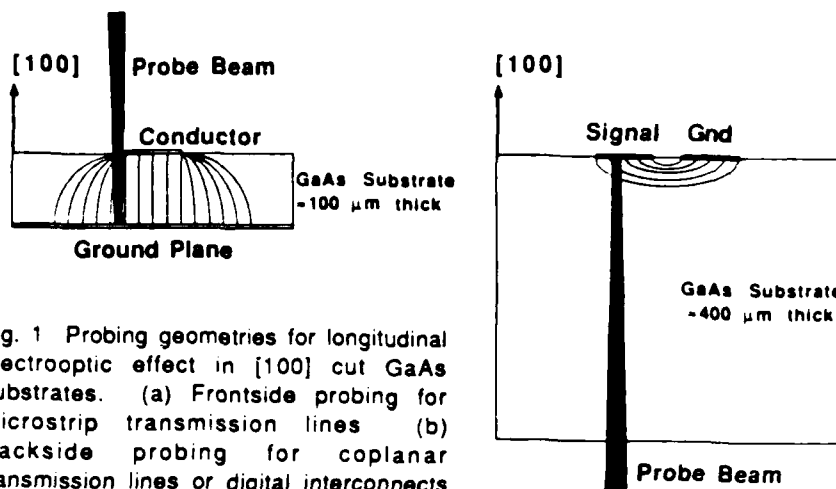


Fig. 1 Probing geometries for longitudinal electrooptic effect in [100] cut GaAs substrates. (a) Frontside probing for microstrip transmission lines (b) Backside probing for coplanar transmission lines or digital interconnects

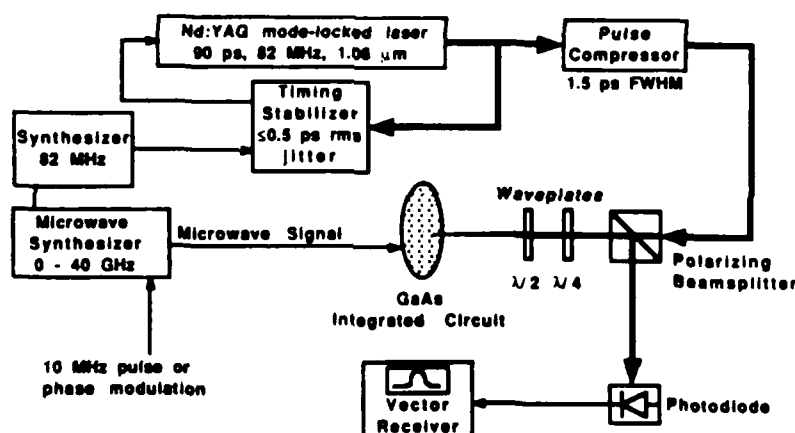


Fig. 2 Schematic of the electrooptic sampler

To drive the IC a microwave synthesizer generates either sinusoidal excitation for microwave circuits or the clock or data signals for digital circuits. For wafer-level testing of IC's a microwave probe station (Cascade Microtech Model 42) was modified to allow for backside electrooptic probing. The transmission line probes used with this test station allow for repeatable, low reflection connections in a 50 Ω environment to 26 GHz. The synthesizer is set to an exact multiple of the laser repetition rate (82 MHz), plus a small frequency offset Δf ; the resulting intensity modulation at the photodiode receiver varies at this offset rate Δf . To enhance the system sensitivity, the synthesizer is also modulated at 10 MHz to allow synchronous detection in a spectral region where low-frequency laser amplitude noise is below the shot noise limit.

3. Bandwidth and Noise Considerations

The system's bandwidth is determined by the optical transit time of the pulse through the GaAs substrate where fields are present, the optical pulsewidth, and pulse-to-pulse timing jitter of the laser with respect to the microwave synthesizer driving the circuit. In general the optical transit time of the pulse in the GaAs substrate can be neglected. Because the optical and microwave dielectric constant in GaAs are nearly equal, microwave transmission lines have a cutoff frequency for higher-order modes roughly equal the inverse of the optical transit time. Well-designed microwave circuits operate at frequencies well below the multimode cutoff frequency. Only when measuring interconnects near or above the cutoff frequency (where dispersive characteristics are of interest) must the optical transit time be considered.

To accurately measure the shape of circuit waveforms, the impulse response of the system should be of short duration and free of "wings" (long-duration substructure). Using a 1 km fiber in the pulse compressor introduces significant group velocity dispersion, producing a more linear frequency chirp [5], reducing the wings on the compressed pulse. To accurately determine the extent of wings on the compressed pulse, the autocorrelation is numerically Fourier transformed to obtain the power spectral density of the pulse.

Timing jitter influences both bandwidth and sensitivity; the impulse response of the sampling system is the convolution of the optical pulse with the probability distribution of its arrival time (neglecting optical transit time), while those Fourier components of the jitter lying within the detection bandwidth of the receiver introduce noise proportional to the time derivative of the measured waveform as shown in Fig. 3. Stabilization of the laser timing is thus imperative for low-noise measurements of microwave or picosecond signals. To address this issue a timing stabilization feedback system was implemented to reduce the jitter to a level less than the optical pulsewidth. Figure 4 shows the reduction of the timing jitter of our laser, measured as phase noise with an RF spectrum analyzer. With the addition of a low-phase noise synthesizer (HP8662) and an improved modelocker the laser exhibits jitter of ≤ 300 fs rms.

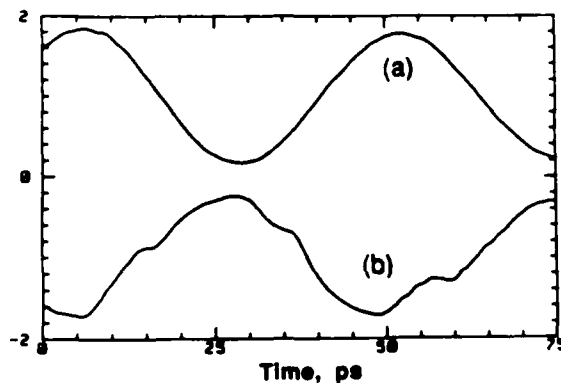


Fig. 3 A 20 GHz signal, measured with the electrooptic sampler. (a) Timing stabilizer on. (b) Timing stabilizer off. Excess timing jitter introduces excess amplitude noise, timing error, and reduces measurement bandwidth.

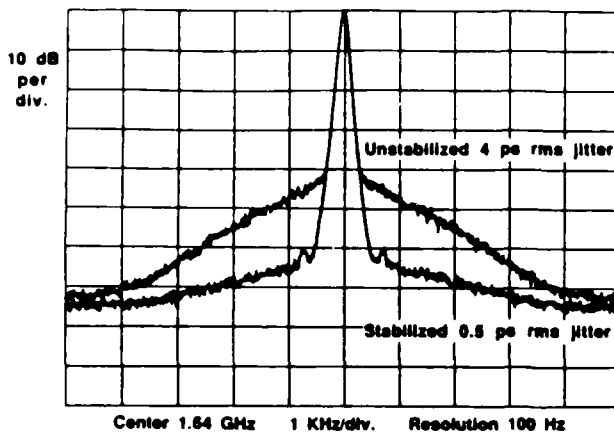


Fig. 4 Timing jitter measured as phase noise measuring the laser output with a photodiode connected to an RF spectrum analyzer. Integrating the phase noise over frequency gives timing jitter.

To achieve accuracy, repeatability, and fast acquisition of circuit measurements requires shot-noise-limited sensitivity in the detection system [2]. Low-frequency noise on the laser contributes excess amplitude noise above the shot noise limit to a frequencies of several hundred kilohertz. To translate the signal detection to a frequency where this $1/f$ laser noise is below the shot noise limit, the microwave signal to the IC is modulated at 10 MHz. With a narrowband 10 MHz vector receiver, the resulting shot-noise-limited sensitivity is sufficient to acquire measurements at scan rate of 10-100 Hz. For microwave circuits or simple digital circuits, the input signal is pulse modulated at 10 MHz. For sequential digital circuits which do not operate correctly with chopped excitation, a small-deviation 10 MHz phase modulation is used. In this case the received signal, proportional to the derivative of the sampled waveform, is integrated in software [6].

The pulse compressor is also a source of several types of excess amplitude noise. Stimulated Raman scattering (SRS) with gain proportional to the pump intensity and interaction length, sets an upper limit to the intensity in the fiber and thus an upper limit to its compression. However, as the pump intensity approaches the SRS threshold, we observe a substantial increase in amplitude noise above the shot noise limit on the compressor output (Fig. 5). The period of the repetitive noise spectrum in this figure corresponds to the free spectral range of the 1 km fiber; the high gain of the SRS and 4% Fresnel reflection at each end facet form a parasitic synchronously-pumped fiber-Raman laser [7]. Self-phase modulation (SPM) occurs over the entire length of the fiber while the interaction length for SRS is set by dispersion-induced walkoff between the input and Stokes-shifted wavelengths, approximately 60 meters. This dispersion also causes the 1.06 μm pump and the 1.12 μm Raman pulse to separate by 1.8 ns over the length of the 1 km fiber. The weakly reflected Raman pulse is further amplified if after its first round trip through the fiber it is synchronized to within 1.8 ns of a pump pulse. With this condition the Raman threshold with the 1 km fiber is 400 mW average power from the fiber output. Trimming the fiber length a few inches defeats this synchronism and increases the Raman threshold to 700 mW. We routinely obtain 50X compression ratios at power levels (350 mW average power from the fiber output) well below the Raman threshold.

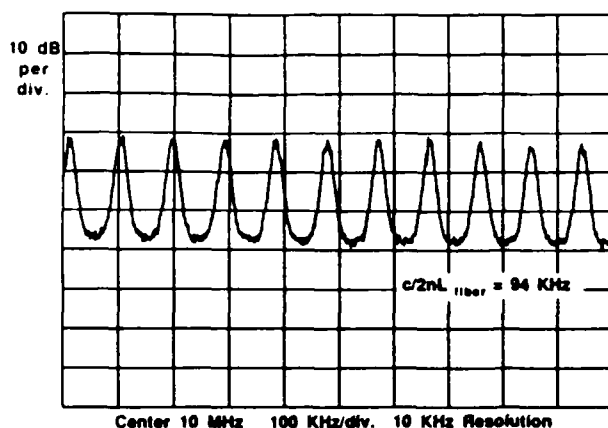


Fig. 5 Noise spectrum of pulse compressor output near the SRS threshold. The free spectral range of the 1 km fiber is 94 kHz, indicating the fiber forms a parasitic fiber-Raman laser.

In addition to SRS the fiber generates broadband polarization noise, possibly arising from guided acoustic wave Brillouin scattering [8]. The polarization noise is converted to amplitude noise after passing through the grating pair in the compressor. Adjusting the polarization from the fiber to maximize transmission through the grating path results in second-order intensity variations due to polarization fluctuations reducing this excess noise to a level below the shot noise limit. To suppress polarization drift, the non-polarization-preserving fiber is placed in a temperature-stabilized environment.

4. Circuit Measurements

Propagation delays of switching devices in simple test circuits, measured by either electrooptic sampling or by conventional methods, are used to project the maximum clock frequency of these devices used in digital systems; unless the test circuit provides representative switching voltages, interface impedances, and fan-in/fan-outs, the measured delays will not correlate well with the maximum clock frequency of circuits such as shift registers, binary multipliers, and memory. In particular, the risetime of a single device driven by a low-impedance photoconductor and loaded by a low-impedance transmission line will be much shorter than the propagation delay of a logic gate driven by the moderate output impedance of a driving gate and loaded by the input capacitance of a cascaded gate. The simplest representative test structures, ring oscillators and inverter strings, load the gates with unity fan-out and hence give optimistically small delay measurements. Ring oscillators often operate small-signal (without full logic-level swings), however, while inverters strings allow large-signal operation to be verified. Using such a string of 1 μm gate buffered-FET-logic (BFL) inverters, we have measured large-signal gate propagation delays of 75 ps [6].

Master-slave flip-flops, connected as binary frequency dividers, operate with realistic signal levels and loading conditions, and serve as better performance indicators. We have tested 23 GHz dynamic and 18 GHz static frequency dividers implemented in BFL and capacitively enhanced (CEL) MESFET logic from Hughes Research Laboratories [9] using the modified Cascade probe station for electrooptic sampling. These circuits used 0.2 μm e-beam written gates, molecular-beam epitaxy grown channels, air-bridge interconnects, and optimized feedback to achieve such clock rates. Correct divide-by-two operation was verified by direct waveform measurement (Fig. 6), gate propagation delays of 30-40 ps were measured and correlated to maximum clock frequencies (Fig. 7), and the internal delays through the inverting and source-follower stages of individual BFL gates were identified.

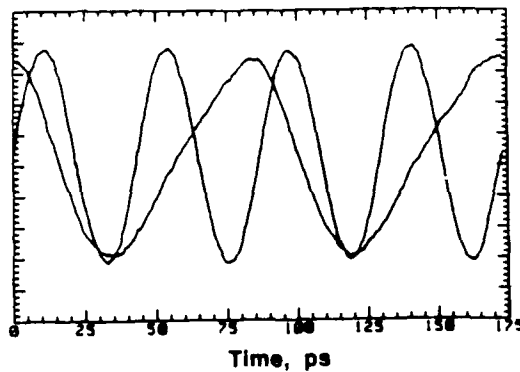


Fig. 6 BFL dynamic frequency divider, clock and output waveforms, clocked at 23 GHz.

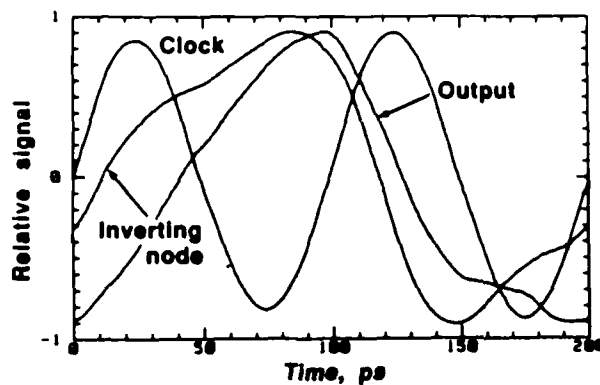


Fig. 7 BFL static frequency divider clocked at 10 GHz. Twice the delay from the clock to the output sets the circuits maximum clock frequency.

Configured as a vector voltmeter, the sampler has been used to measure voltage transfer functions of microwave structures and circuits, including slotted-line measurements of standing wave ratio (Fig. 8), phase velocity, and lateral potential distribution [10] of microstrip and coplanar waveguide transmission lines. On GaAs microwave amplifiers, propagation of microwave signals internal to microstrip and coplanar-waveguide MESFET distributed amplifiers [11,12] have been measured (Fig. 9), and the gain saturation behavior of these circuits investigated (Fig. 10).

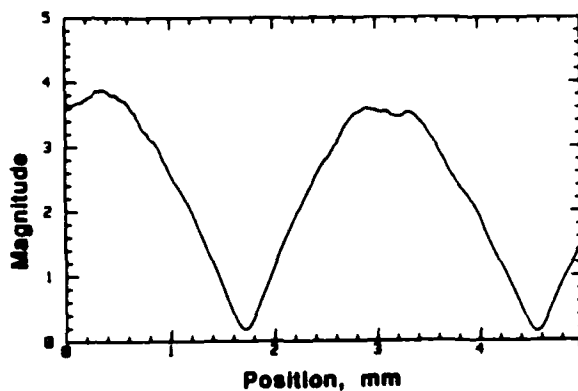


Fig. 8 Standing wave on a CPW transmission line at 20 GHz with an open termination at one end.

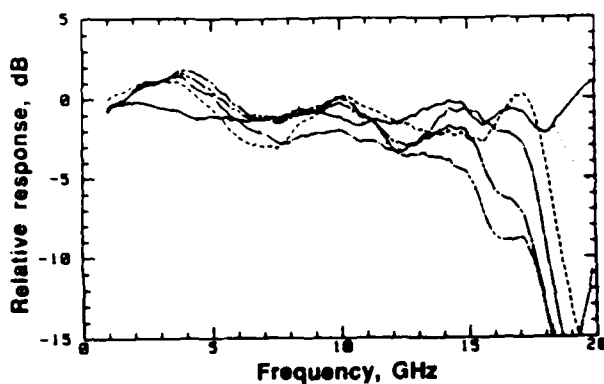


Fig. 9 Small-signal gate voltages vs. frequency of a 5-stage 2-18 GHz CPW distributed amplifier.

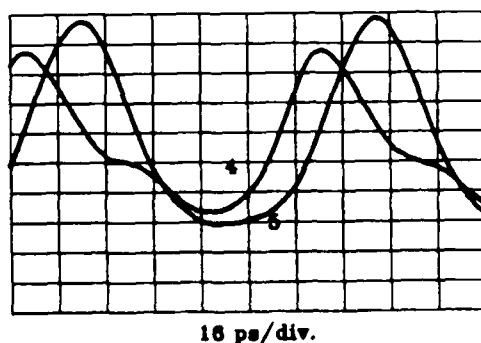


Fig. 10 Saturation waveform at drains 4 and 5 of a 2-18 GHz distributed amplifier at 10 GHz and 1 dB gain compression

5. Conclusion

With a pulsewidth of 1.5 ps FWHM and a demonstrated timing jitter ≤ 300 fs, the electrooptic sampler has a measurement bandwidth exceeding 100 GHz. A microwave probe station has been modified to allow for electrooptic probing of GaAs IC's at the wafer level. With a spatial resolution of 3 μm and a noise floor of 300 μV (1 Hz), the system is suitable for characterization of ultrafast digital and analog GaAs IC's, such as inverter chains, multiplexers, frequency dividers, and microwave amplifiers.

6. Acknowledgments

We thank M. Riazat of Varian Associates and J. Jensen of Hughes Research Laboratories for their invaluable assistance with their GaAs IC's and the generous equipment donations of Cascade Microtech, Inc., Tektronix, Inc. and the Hewlett-Packard Co. M. Rodwell acknowledges an IBM Pre-doctoral Fellowship and K. Weingarten acknowledges a Newport Research Award. This work was supported in part by the Air Force Office of Scientific Research contract F49620-85K-0016 and by Wright-Patterson Air Force Base Avionics Laboratory contract F33615-86-C-1126.

7. References

1. J.A. Valdmanis, G.A. Mourou., and C.W. Gabel: IEEE J. Quant. Elec., 19, 664 (1983)
2. B.H. Kolner and D.M. Bloom: IEEE J. Quant. Elec., 22, 69, (1986), J.A. Valdmanis and G.A. Mourou: ibid., 22,79 (1986)
3. J.L. Freeman, S.K. Diamond, H. Fong, and D.M. Bloom: Appl. Phys. Lett., 47, 1083 (1985)
4. M.J.W. Rodwell, K.J. Weingarten, D.M.Bloom, T. Baer, and B.H. Kolner: Optics Letters. 11, 638, (1986)
5. D. Grischowski and C.A. Balant: Appl. Phys. Lett., 41, 1, (1982)
6. M.J.W. Rodwell, K.J. Weingarten, J.L. Freeman, and D.M.Bloom: Electron. Lett., 22, 499 (1986)
7. M.N. Islam, L.F. Mollenauer, and R.H. Stolen: Ultrafast Phenomena V, ed. by G.R. Fleming and A.E. Siegman, Springer Ser. Chem. Phys., Vol. 46 (Springer-Verlag, New York 1986) p. 46
8. M. Levenson, R.M. Shelby, and P.W. Bayer: Phys. Rev. B, 31, 5244 (1985)
9. J.F. Jensen, L.G. Salmon, D.S. Deakin, and M.J. Delaney: Technical Digest of the 1986 International Electron Device Meeting, p. 476
10. K.J. Weingarten, M.J.W. Rodwell, J.L. Freeman, S.K. Diamond, and D.M. Bloom: Ultrafast Phenomena V, ed. by G.R. Fleming and A.E. Siegman, Springer Ser. Chem. Phys., Vol. 46 (Springer-Verlag, New York 1986) p. 98
11. M.J.W. Rodwell, M. Riazat, K.J. Weingarten, B.A. Auld, and D.M. Bloom: IEEE Trans. Microwave Theory Tech., MTT-34, 1356, (1986)
12. G. Zdaslук, M. Riazat, R. LaRue, C. Yuen, and S. Bandy: To appear in Picosecond Electronics and Optoelectronics, (Springer-Verlag, 1987)

NONLINEAR TRANSMISSION LINE FOR PICOSECOND PULSE COMPRESSION AND BROADBAND PHASE MODULATION

Indexing terms: Integrated circuits, Transmission lines, Phase modulation

Simulations and scale-model experiments indicate that shock-wave formation on a GaAs integrated circuit nonlinear transmission line will generate electrical pulses with rise times less than 5 ps, and that velocity modulation on the line will permit broadband phase modulation from DC to 40 GHz.

Devices for generation of fast-rise-time electrical transitions are crucial for high-speed digital and analogue applications and for wide-bandwidth electronic instrumentation. In particular, the bandwidth of diode sampling bridges used in sampling oscilloscopes, network analysers and microwave frequency counters is limited by the rise time of the pulse gating the diodes. Step-recovery diodes can generate transitions of 50 ps rise time and ~10 V amplitude, while tunnel diodes can generate steps of 25 ps rise time but with amplitude (~0.2 V) insufficient for most applications.

The nonlinear charge-voltage relationship of a reverse-biased semiconductor junction (variable capacitance diode or varactor) is used for harmonic generation at frequencies as high as 350 GHz.¹ If varactors are instead incorporated into a transmission line as periodic nonlinear shunt capacitances, a nonlinear transmission line is formed. Parametric gain and shock-wave formation on fully distributed varactor lines was studied by Landauer² and Khokhlov.³ Jager and Tegude⁴ have studied harmonic generation, slow-wave propagation and parametric amplification on periodic nonlinear lines. We show, by calculations, simulations and results with a 20:1 scale model, that shock-wave formation on a monolithic periodic nonlinear line can be used for compression of 25 ps electrical transitions to rise times less than 5 ps, and that velocity modulation on the line can be used for phase modulation⁴ of carriers from DC to millimetre-wave frequencies.

The device is shown in Fig. 1. A relatively high-impedance transmission line of characteristic impedance Z_1 is period-

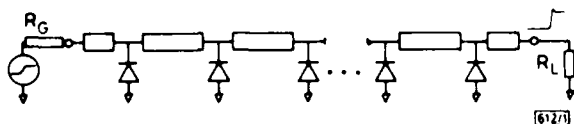


Fig. 1 Nonlinear transmission line

ically loaded, at electrical spacings of τ (in units of time), by Schottky diodes serving as voltage-dependent shunt capacitances, producing a synthetic transmission line whose propagation velocity is voltage-dependent. For input signals $v_{in}(t)$ such that at all points on the line the propagating wave is of sufficiently long rise time, the output of the line is³

$$v_{out}(t) = v_{in}[t - T(v)] \quad (1)$$

$$T(v) = n\tau [LC_T(v)]$$

where n is the number of diodes in the line, $L = Z_1\tau$ is the transmission-line inductance per section of line, $C_T(v) = [C_J(v) + \tau Z_1]$ is the total capacitance per section and the capacitance of a step-junction diode with junction potential ϕ is $C_J(v) = C_{J0} \sqrt{1 + v/\phi}$.

As an input signal $v_{in}(t)$, a step with initial voltage v_i , final voltage v_k and rise time $T_{r,in}$, propagates along the line, the rise time will at first decrease linearly with distance. As the pulse rise time decreases, dispersion arising from the structure's cutoff frequency ω_c competes with the compression arising from the voltage-dependent propagation velocity, and a final limited rise time $T_{r,min}$, of the order of but longer than $2.2/\omega_c$, is reached at which the rise time compression per section due to line nonlinearity is equal to the rise time broadening per section due to line dispersion. The output rise

time is given by

$$T_{r,out} \approx \max \left\{ \begin{array}{l} T_{r,in} - [T(v_i) - T(v_k)] \\ T_{r,min} \end{array} \right\} \quad (2)$$

Line periodicity introduces the dominant cutoff frequency ω_{per} , given by the implicit relationship

$$Z_1 C_{is} \omega_{per} \sin(\omega_{per} \tau) / 2 = \cos(\omega_{per} \tau) + 1 \quad (3)$$

$$\omega_{per} \approx 2 \sqrt{LC_{is}}$$

where $C_{is} = [Q(v_k) - Q(v_i)] / (v_k - v_i)$ is the varactor's large-signal capacitance, and where the approximation holds for $C_{is} \gg \tau/Z_1$. Increasing ω_{per} by decreasing the diode spacing τ will decrease both the small-signal characteristic impedance $Z_0(v) = \sqrt{L/C_T(v)}$ and the large-signal characteristic impedance $Z_{ls} = \sqrt{LC_{is} + \tau Z_1}$; if we constrain $Z_{ls} = 50 \Omega$, then C_{is} must scale with $Z_1\tau$ and ω_{per} is then limited by lithographic constraints on the minimum varactor size. The varactor series resistance r_s introduces a varactor cutoff frequency of $\omega_{rc} \approx 1/r_s C_{is}$, limiting the compressed rise time to $\sim 2.2 r_s C_{is}$.³ Finally, both analysis^{5,6} and experimental results^{5,7} indicate that pulse broadening due to transmission line dispersion and skin impedance is small relative to that due to line periodicity.

Schottky diodes with terahertz $r_s C$ cutoff frequencies are readily integrated with microstrip or coplanar waveguide transmission lines on GaAs substrates. A nonlinear transmission line incorporating 60 diodes with $C_{J0} = 50$ fF (active area $5 \times 5 \mu\text{m}$ on material with $3 \times 10^{16} \text{ cm}^{-3}$ doping) at $160 \mu\text{m}$ spacings ($\tau = 1.4$ ps) along a 90Ω coplanar waveguide has a large-signal characteristic impedance Z_{ls} of 50Ω for a 0–2 V step. The periodic-line cutoff frequency of 140 GHz, an order of magnitude smaller than typical varactor cutoff frequencies, should result in a minimum compressed rise time of the order of $\sim 0.35/140 \text{ GHz} = 2.5$ ps; more accurate nonlinear circuit simulations using SPICE indicate that a 2 V step-function input with 25 ps rise time will produce an output rise time of 4 ps.

We have constructed a 20:1 scale model of the proposed monolithic device, using 45 silicon abrupt-junction diodes with $C_{J0} = 1$ pF and $\phi = 0.8$ V at 28 ps spacings along a 90Ω microstrip transmission line. Because the diode polarity on the scale model is reversed from that of Fig. 1, the scale model compresses negative transitions. The measured group delay $T(v)$ varies from 2.2 ns to 1.7 ns and $Z_0(v)$ varies from 45Ω to 58Ω as the bias is varied from 0 V to -3 V. In simulations the scale model compresses 0 V to -2 V transitions of 360 ps fall time to 80 ps output fall time. To compress the slower 525 ps transitions available from our pulse generator, the input pulse initial voltage is increased to 0.5 V, increasing the line's compression $[T(v_k) - T(v_i)]$. The bias change increases C_{is} and hence decreases ω_{per} ; the resulting compressed output fall time is 100 ps (Fig. 2). A step-function input is not necessary for fast edge generation; driving the line with a 15 dBm 300 MHz sine wave with -1.25 V bias generates a sawtooth output waveform with 100 ps fall time.

The nonlinear line is also a broadband voltage-controlled

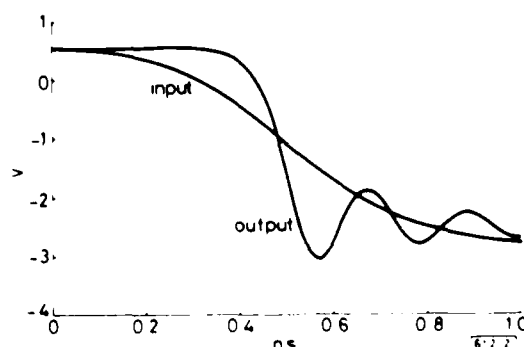


Fig. 2 Measured compression of 525 ps input fall time to 100 ps output fall time on 20:1 scale model

linear phase-shifter; at frequencies from DC to $\sim \omega_{per}/4$ the line provides constant voltage-controlled group delay and small insertion loss, while Z_0 shows only a small variation with voltage. Superimposing on the line a DC bias plus carrier and modulation frequencies results in phase modulation. The carrier ω_0 , modulation ω_m and generated sidebands $\omega_0 \pm n\omega_m$ are phase-matched provided that all these frequencies are much less than ω_{per} ; thus the phase modulation is broadband in both the carrier and modulation frequencies. By eqn. 1, spurious harmonics of ω_0 and ω_m are generated; second- and third-order intercepts for the scale model are +12 and +10 dBm at 1 GHz and -1 V bias. On the 20:1 scale model, carriers from 100 MHz to 2.5 GHz were phase-modulated at frequencies from 10 MHz to 1 GHz (Fig. 3); a monolithic nonlinear line should provide broadband phase modulation from DC to ~ 40 GHz.

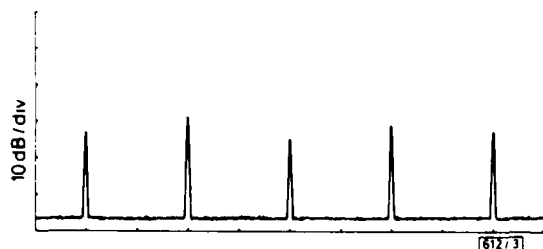


Fig. 3 2.5 GHz carrier phase-modulated at 200 MHz by scale-model nonlinear line

Centre = 2.5 GHz, span = 1 GHz

Diode sampling bridges are currently driven by 25–50 ps steps from step-recovery diodes; if a nonlinear line compressed these steps to 4 ps rise time, the bandwidth of sampling oscilloscopes, network analysers and frequency counters would be extended to 100 GHz. As a phase modulator or voltage-controlled phase shifter monolithically integrated on

GaAs with Schottky diode mixers and FET amplifiers, the nonlinear line should find broad application in microwave and millimetre-wave systems.

Acknowledgments: This work was supported by the US Office of Naval Research under grant N00014-85-K-0381. M. Rodwell acknowledges an IBM fellowship.

M. J. W. RODWELL
D. M. BLOOM
B. A. AULD

4th November 1986

Edward L. Ginzton Laboratory
Stanford University
Stanford, CA 94305, USA

References

- 1 ARCHER, J. W., and FABER, M. T.: 'High output single- and dual-diode millimeter-wave frequency doublers', *IEEE Trans.*, 1985, **MTT-33**, pp. 533–538
- 2 LANDAUER, R.: 'Parametric amplification along nonlinear transmission lines', *J. Appl. Phys.*, 1960, **31**, pp. 479–484
- 3 KHOKHLOV, R. V.: 'On the theory of shock radio waves in nonlinear lines', *Radiotekhnika i elektronika*, 1961, **6**, pp. 917–925
- 4 JAGER, D., and TEGUDE, F.-J.: 'Nonlinear wave propagation along periodic-loaded transmission line', *Appl. Phys.*, 1978, **15**, pp. 393–397
- 5 HASNAIN, G., DIENES, A., and WHINNERY, J. R.: 'Dispersion of picosecond pulses in coplanar transmission lines', *IEEE Trans.*, 1986, **MTT-34**, pp. 738–741
- 6 WIGINGTON, R. L., and NAHAM, N. S.: 'Transient analysis of coaxial cables considering skin effect', *Proc. IRE*, 1956, pp. 166–174
- 7 KETCHEN, M. B., GRISCHKOWSKI, D., CHEN, T. C., CHI, C.-C., DULING, I. N., HALAS, N. J., HALBOUT, J.-M., KASH, J. A., and LI, G. P.: 'Generation of subpicosecond electrical pulses on coplanar transmission lines', *Appl. Phys. Lett.*, 1986, **48**, pp. 751–753

MICROWAVE MEASUREMENTS OF GaAs INTEGRATED CIRCUITS USING ELECTROOPTIC SAMPLING

K. J. Weingarten, R. Majidi-Ahy, M. J. W. Rodwell, B.A. Auld, and D. M. Bloom

Edward L. Ginzton Laboratory
Stanford University
Stanford, CA 94305

Abstract

We describe the electrooptic sampling system at Stanford with emphasis on the requirements for microwave measurements. Results presented include internal-node measurements of 20 GHz distributed amplifiers, propagation delays in GaAs frequency dividers clocked to 18 GHz, and VSWR on IC transmission lines to 40 GHz.

Introduction

Gallium Arsenide (GaAs) microwave integrated circuits (IC's) now operate at millimeter-wave frequencies, while GaAs digital IC's operate with clock rates at microwave frequencies up to 18 GHz. Digital IC's are currently tested only by indirect techniques (multi-stage propagation delay or cycle times), while microwave circuits are tested by external scattering parameters; if the circuit does not perform correctly, the cause can only be inferred from its external response. Electrooptic sampling was initially developed to measure the response of photoconductors and photodetectors faster than the time resolution of sampling oscilloscopes and used an external electrooptic modulator connected to the device under test in a hybrid fashion [1,2]. The system developed at Stanford uses the GaAs IC substrate as the electrooptic material, permitting detailed internal-node circuit evaluation with picosecond time resolution.

The Sampling System

GaAs is electrooptic; the electric fields associated with conductor voltages induce optical birefringence, causing a polarization change to a probe beam passing through these fields. Figures 1 and 2 show the cross-section of typical probing geometries. For standard [100] cut GaAs substrates the probe beam polarization is affected only by the longitudinal field components. The beam is focused through the IC substrate where its polarization is modulated by the voltage across the substrate at the test point. The reflected light is passed through a polarizer and its intensity detected by a photodiode. The probe beam polarization is adjusted to the linear region of the intensity transmission of the polarizer, resulting in a change in intensity at the photodiode proportional to the voltage across the substrate at the probe point [3].

For frontside probing, suitable for microstrip transmission lines, the fields extend from the conductor roughly the distance of the substrate thickness; the probe spot size is set to approximately one-tenth of the substrate thickness to accurately measure the conductor potential. For backside probing, suitable for planar transmission lines and wire interconnects, the characteristic extent of the fields into the substrate is the distance between the signal conductor and ground; the substrate thickness must be

much greater than the signal-ground spacing (a requirement met by good high-frequency IC design) and the probe beam spot diameter should be less than or equal to the conductor width. An additional requirement on the IC is that the backside of the wafer be sufficiently polished to allow for passage of the probe beam with negligible scattering.

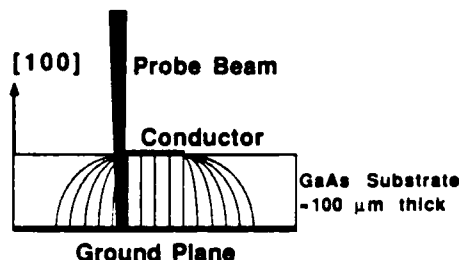


Fig. 1 Frontside probing for microstrip transmission lines. Typical conductor widths are 40-70 μms.

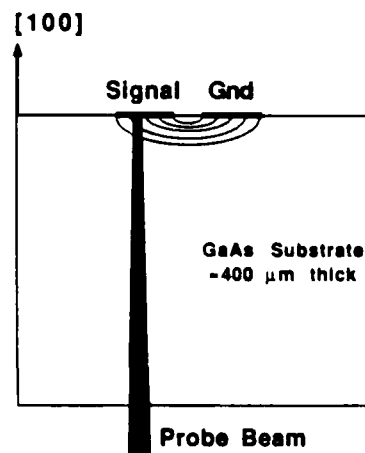


Fig. 2 Backside probing for planar transmission lines and wire interconnects. Conductor widths may be as small as 2 μms.

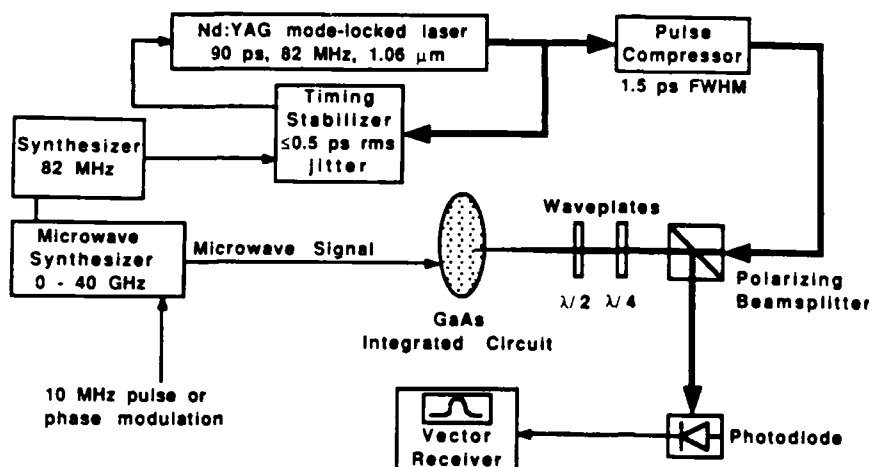


Fig. 3 Electrooptic sampler system

The sampling system is shown schematically in Fig. 3. A commercially available, mode-locked Nd:YAG laser produces 1.06 μm , 90 ps pulses at an 82 MHz rate. The laser has free-running pulse-to-pulse timing fluctuations of 4 ps rms, reduced to less than 300 fs rms by a phase-lock-loop feedback system [4]. A fiber-grating pulse compressor shortens the pulses to 1.5 ps FWHM (full width at half maximum) [5,6]. The beam passes through a polarizing beamsplitter and two waveplates to adjust its polarization, then is focused through the IC substrate with a microscope objective to a 3 μm spot on the probed conductor (backside probing) or a 10 μm spot on the ground plane adjacent to the probed conductor (frontside probing). The reflected light is analyzed by the polarizing beamsplitter; the change in intensity, proportional to the voltage across the GaAs substrate, is detected by a photodiode connected to a vector receiver.

To drive the IC a microwave synthesizer generates either sinusoidal excitation for microwave circuits or the clock or data signals for digital circuits. For wafer-level testing of IC's a microwave probe station (Cascade Microtech Model 42) was modified to allow for backside electrooptic probing. The transmission line probes used with this test station allow for launching a signal on the IC with repeatable, low reflection connections in a 50 Ω environment to 26 GHz. The synthesizer is set to an exact multiple of the laser repetition rate (82 MHz), plus a small frequency offset Δf (1-100 Hz); the resulting intensity modulation at the photodiode receiver varies at this slow offset rate Δf . To enhance the system sensitivity, the synthesizer is also modulated at 10 MHz to allow synchronous detection in a spectral region where laser amplitude noise approaches the shot noise limit.

Measurement bandwidth/time resolution

The system's bandwidth is determined by the optical transit time of the pulse through the GaAs substrate where fields are present, the optical pulsewidth, and pulse-to-pulse timing jitter of the laser with respect to the microwave synthesizer driving the circuit. In general the optical transit time of the pulse in the GaAs substrate can be neglected for microwave IC's. Because the optical and microwave dielectric constant in GaAs are nearly equal, microwave transmission lines have a cutoff frequency for higher-order modes roughly equal the inverse of the optical transit time. Well-designed microwave circuits operate at frequencies well below the multimode cutoff frequency. Only when measuring interconnects near or above the cutoff frequency (where dispersive characteristics are of interest) must the optical transit time be considered. For example, the optical transit

time for a 125 μm thick substrate is 3 ps, corresponding to a 3 dB response rolloff of >100 GHz.

The compressed pulsewidth, 1.5 ps FWHM, is measured with an optical autocorrelator and calculated assuming a gaussian pulseshape. However, a more quantitative estimate of the spectral content of the pulse is determined by numerically Fourier transforming the autocorrelation. This calculation gives the power spectral density of the pulse with no assumption about the pulseshape.

Timing jitter influences both bandwidth and sensitivity; the impulse response of the sampling system is the convolution of the optical pulse with the probability distribution of its arrival time (neglecting optical transit time), while those Fourier components of the jitter lying within the detection bandwidth of the receiver introduce noise proportional to the time derivative of the measured waveform [4]. Stabilization of the laser timing is thus imperative for low-noise measurements of microwave or picosecond signals. To address this issue a timing stabilization feedback system was implemented to reduce the jitter to a level less than the optical pulsewidth. Figure 4 shows the measured phase noise of one harmonic of the laser with an HP 8662 low-phase noise synthesizer as the reference for the feedback system. Integrating the phase noise allows calculation of the jitter in time, less than 300 fs rms.

Measurement sensitivity

To achieve accuracy, repeatability, and fast acquisition of circuit measurements requires shot-noise-limited sensitivity in the detection system [2]. Low-frequency noise on the laser contributes excess amplitude noise above the shot noise limit to a frequencies of several hundred kilohertz. To translate the signal detection to a frequency where this 1/f laser noise is below the shot noise limit, the microwave signal to the IC is modulated at 10 MHz. With a narrowband 10 MHz vector receiver, the resulting shot-noise-limited sensitivity is sufficient to acquire measurements at scan rate of 10-100 Hz with a typical voltage sensitivity of 100-300 $\mu\text{V}/\text{MHz}$. For microwave circuits or simple digital circuits, the input signal is pulse modulated at 10 MHz. For sequential digital circuits which do not operate correctly with chopped excitation, a small-deviation 10 MHz phase modulation is used. In this case the received signal, proportional to the derivative of the sampled waveform, is integrated in software [7].

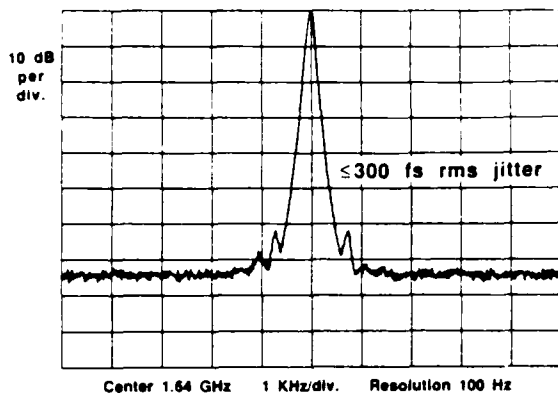


Fig. 4 Laser intensity phase noise at the 20th harmonic of the pulse repetition rate, measured with a photodiode and RF spectrum analyzer. The noise floor of this measurement is instrumentation limited, giving an upper limit for the timing jitter of 300 fs rms.

The pulse compressor is also a source of several types of excess amplitude noise, due to stimulated Raman scattering (SRS) and temperature-induced polarization drift in the non-polarization-preserving fiber [8]. These noise sources are avoided by keeping the optical power in the fiber well below the Raman threshold and by temperature stabilizing the fiber to suppress polarization drift.

Circuit Measurements

Configured as a vector voltmeter, the sampler can measure voltage transfer functions of microwave structures and circuits, including measurements of standing wave ratio, phase velocity, and lateral voltage distribution of microstrip [9] and coplanar waveguide transmission (CPW) lines. On GaAs microwave amplifiers, propagation of microwave signals internal to microstrip and coplanar-waveguide MESFET distributed amplifiers (Fig. 5)[10,11] have been measured.

The sampler measures the standing-wave voltage on a conductor due to the sum of the forward and reverse traveling waves

$$V(z) = V^+e^{-j\beta z} + V^-e^{+j\beta z}$$

where V^+ and V^- are the forward and reverse traveling coefficients, β is the wavenumber, and z the position. For a one-port transmission line the ratio of the traveling wave coefficients V^+ and V^- is the reflection coefficient Γ , or S_{11} , the insertion loss. To determine this ratio we have measured the voltage as a function of position along the conductor and then numerically fit the data to obtain a minimum mean-square-error estimate of the traveling wave coefficients (Figs. 6 & 7.)

The sampler can also be used as a time-domain instrument to measure internal-node waveforms in the IC. We have measured propagation delays on digital circuits clocked at microwave frequencies such as an 18 GHz static frequency divider (from Hughes Research Labs[12],[13]), gain saturation of distributed amplifiers (from Varian Research[11]), and frequencies to 40 GHz on transmission lines (Fig. 8). This type of time-domain information can be obtained with neither a sampling oscilloscope (due to limited bandwidth) nor a network analyzer (small-signal response only.)

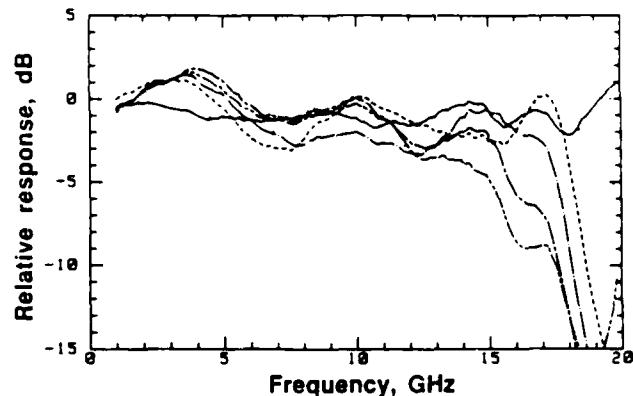


Fig. 5 Frequency response of internal gate nodes and termination in a 5-stage distributed amplifier. The ripple is due to standing waves on the conductor, the rolloff at 18 GHz is due to the cutoff of the periodically loaded gate line, and the droop in the magnitude is loss due to FET input conductance.

Conclusion

With a pulsewidth of 1.5 ps FWHM and a timing jitter ≤ 300 fs, the electrooptic sampler has a measurement bandwidth exceeding 100 GHz. A microwave probe station, modified to allow for electrooptic probing of GaAs IC's at the wafer level, has been used to characterize ultrafast digital GaAs IC's clocked at microwave frequencies and microwave IC's such as distributed amplifiers. Directivity for network analyzer type measurements is obtained by scanning the probe along transmission line conductors to calculate the forward and reverse traveling wave coefficients from the voltage standing wave. We have experimentally verified this technique for a one port, terminated transmission line to millimeter-wave frequencies. Extension of this technique to two-port measurements of devices and circuits will allow for full S-parameter measurements with the reference plane on the IC, avoiding complex de-embedding of IC test fixtures.

Acknowledgments

We acknowledge the generous equipment donations of Cascade Microtech, Inc., Tektronix, Inc., and the Hewlett-Packard Co. with specific thanks to Dale Albin from HP for use of the Ka-band frequency doubler. K. Weingarten acknowledges a Newport Research Award and M. Rodwell acknowledges an IBM Pre-doctoral Fellowship. This work was supported in part by the Air Force Office of Scientific Research contract F49620-85K-0016 and by Wright-Patterson Air Force Base Avionics Laboratory contract F33615-86-C-1126.

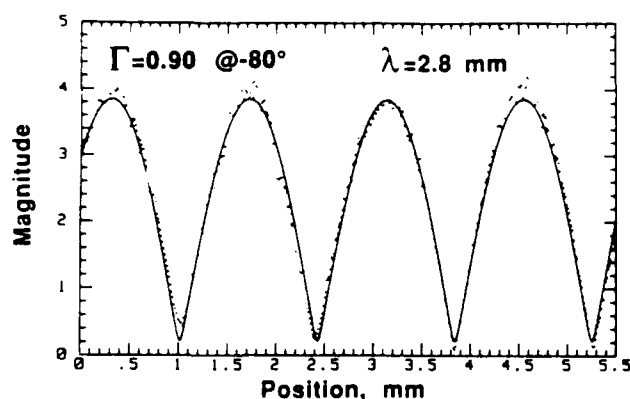


Fig. 6 Magnitude of the voltage standing wave on an open terminated CPW transmission line on GaAs at 40 GHz. The points are the data and the solid line is the fitted curve.

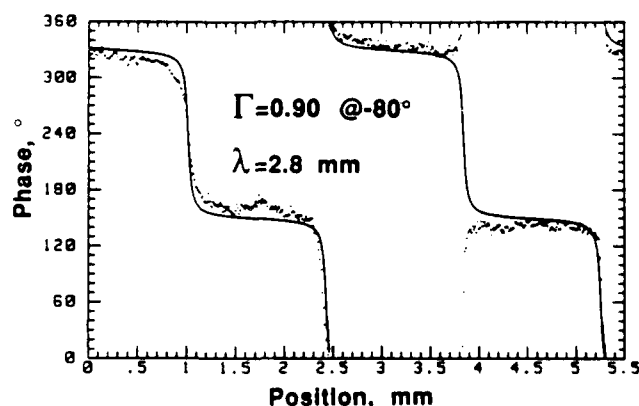


Fig. 7 Phase of the voltage standing wave on an open terminated CPW transmission line on GaAs at 40 GHz. The points are data and the solid line is the fitted curve. Each division of 10° in phase corresponds to 0.7 ps in time.

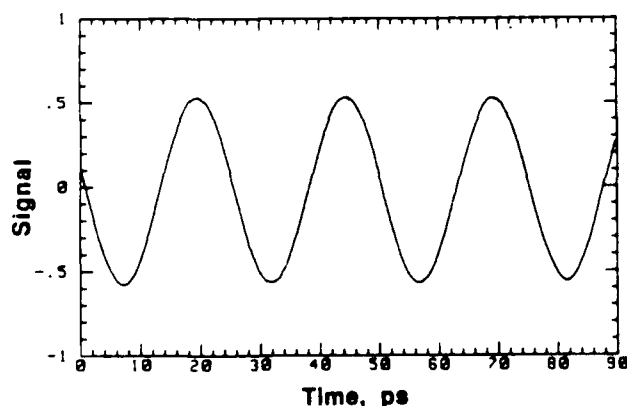


Fig. 8 Time waveform on the CPW line at 40 GHz drive frequency.

References

1. J.A. Valdmanis, G.A. Mourou, and C.W. Gabel: IEEE J. Quant. Elec., **19**, 664 (1983); J.A. Valdmanis and G.A. Mourou: *ibid.*, **22**, 69 (1986)
2. B.H. Kolner and D.M. Bloom: IEEE J. Quant. Elec., **22**, 79, (1986)
3. J.L. Freeman, S.K. Diamond, H. Fong, and D.M. Bloom: Appl. Phys. Lett., **47**, 1083 (1985)
4. M.J.W. Rodwell, K.J. Weingarten, D.M. Bloom, T. Baer, and B.H. Kolner: Optics Letters, **11**, 638, (1986)
5. J.D. Kafka, B.H. Kolner, T. Baer, and D.M. Bloom: Opt. Lett., **9**, 505, (1984)
6. D. Grischkowsky and A.C. Balant: Appl. Phys. Lett., **41**, 1, (1982)
7. M.J.W. Rodwell, K.J. Weingarten, J.L. Freeman, and D.M. Bloom: Electron. Lett., **22**, 499 (1986)
8. K.J. Weingarten, M.J.W. Rodwell, and D.M. Bloom: To appear in Picosecond Electronics and Optoelectronics, (Springer-Verlag, 1987)
9. K.J. Weingarten, M.J.W. Rodwell, J.L. Freeman, S.K. Diamond, and D.M. Bloom: Ultrafast Phenomena V, ed. by G.R. Fleming and A.E. Siegman, Springer Ser. Chem. Phys., Vol. 46 (Springer-Verlag, New York 1986) p. 98
10. M.J.W. Rodwell, M. Riazat, K.J. Weingarten, B.A. Auld, and D.M. Bloom: IEEE Trans. Microwave Theory Tech., **MTT-34**, 1356, (1986)
11. G. Zdasiuk, M. Riazat, R. LaRue, C. Yuen, and S. Bandy: To appear in Picosecond Electronics and Optoelectronics, (Springer-Verlag, 1987)
12. J.F. Jensen, L.G. Salmon, D.S. Deakin, and M.J. Delaney: Technical Digest of the 1986 International Electron Device Meeting, p. 476
13. J.F. Jensen, K.J. Weingarten, D.M. Bloom: To appear in Picosecond Electronics and Optoelectronics, (Springer-Verlag, 1987)

Optical Detection of Charge Modulation in Silicon Integrated Circuits Using a Multimode Laser-Diode Probe

B. R. HEMENWAY, H. K. HEINRICH, J. H. GOLL, Z. XU, AND DAVID M. BLOOM, FELLOW, IEEE

Abstract—This paper reports on the detection of sheet charge densities in silicon devices using an improved noninvasive optical probe based on the detection of free-carrier optical dispersion using a multilongitudinal-mode 1.3- μm semiconductor laser. The improved system incorporates a differential detection technique and a Wollaston prism that allows the use of the multimode laser. These changes increase stability, sensitivity, and bandwidth, allow near shot-noise limited operation, reduce required optical power, and simplify the apparatus. The technique can be applied to probe electronic signals or, conversely, to modulate light using controlled electronic signals. Simple demonstrations of each application are presented.

WHILE the operation of standard semiconductor devices is well understood on the basis of highly developed models, corroborative experimental techniques that directly access the internal parts of the devices have not been available. Such techniques are especially appealing in the development of complex high-performance devices such as resonant tunneling diodes and quantum-well devices, where our understanding of the device physics is less mature. Also, noninvasive access to internal nodes within integrated circuits can help determine logic states, signal levels, and investigate latch-up, heating, and other problems. Recently [1], [2], we reported an optical probe which, working on the principle of free-carrier optical dispersion in semiconductors, provides information not available at the device terminals and thus makes new kinds of tests possible. This letter describes improvements made to the optical probe and demonstrates the detection of single-shot 25-Mbit/s modulation of sheet charge densities in a bipolar transistor. We now use a multimode 1.3- μm semiconductor laser, and have increased sensitivity, stability, and noise performance. A second application—using electronic signals applied to the silicon to modulate light—has been identified. This is illustrated by an optical modulator based on a planar silicon n-p-n transistor. We observed a peak-to-peak amplitude modulation index of 9.8 percent at 25 Mbit/s with signal-to-noise ratio exceeding 6:1.

The improved optical probe is depicted in Fig. 1. New elements include a multilongitudinal-mode 1.3- μm InGaAsP laser, a quartz Wollaston prism, coated high numerical aperture lenses, and two photodiodes for differential detection

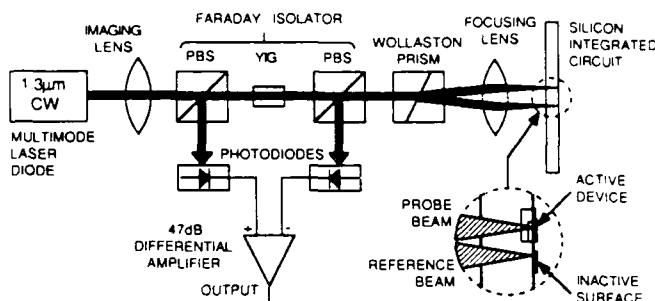


Fig. 1. Schematic diagram of improved charge-sensing optical system, with multimode laser, Wollaston prism, and differential detection.

of the polarized optical beams. The Wollaston prism separates the incoming beam into two orthogonally polarized beams, with a divergence angle of 3.8 mrad. The relative phase shift between the two beams is adjusted by translation of the prism to a point of maximum sensitivity. Optimum sensitivity is achieved when, in the absence of a signal applied to the silicon device, the light returning to the Faraday isolator in Fig. 1 is circularly polarized. For a given laser mode, this is achieved when the relative phase shift induced by a round trip through the Wollaston prism and test wafer is an odd multiple of $\pi/2$. With multimode lasers, it is not possible to meet this condition simultaneously for all modes. However, when the relative phase shift for one mode is $\pi/2$ or a small odd multiple of $\pi/2$ the optimum bias condition can be met to good approximation for all modes. This can also be understood by noting that the path difference for the two beams should be short compared to the laser coherence length.

The "probe" beam is focused to a 3- μm spot in a device area where the time-varying charge density modulates the phase of the beam by free-carrier dispersion. The "reference" beam is focused 30 μm away, onto an inactive area where there is no modulation of the beam. Both beams reflect from the front surface and return through the substrate. The reflective surface of the wafer need not be metalized, but the back surface must be polished. The beams are recombined in the Wollaston prism. The relative phase shift induced by the charge in the silicon device results in elliptical polarization in the recombined beams. (That is, there is a deviation from the circular polarization with no signal on the silicon device.) This polarization modulation is converted to amplitude modulation by the polarizing beam splitters in the Faraday isolator. The detected signals at the two photodiodes are 180° out of phase.

Manuscript received March 24, 1987; revised May 21, 1987. This work was supported by the Joint Services Electronics Program under Contract N00014-84-k-0327.

The authors are with the Ginzton Laboratory, Stanford University, Stanford, CA 94305.

IEEE Log Number 8715905.

The net relative phase shift of the two beams is found by integrating the local refractive index along their paths. The change in refractive index due to free-carrier dispersion is given by

$$\Delta n = -\frac{n_0 q^2 \lambda_0^2}{8 \pi^2 c^2 \epsilon_0} \left[\frac{N_e}{m_{e,e}^*} + \frac{N_h}{m_{h,h}^*} \right]$$

where q is the electronic charge, λ_0 is the vacuum wavelength, n_0 is the refractive index, ϵ_0 is the material permittivity, N_e and N_h are the local time-dependent free electron and hole concentrations, and $m_{e,e}^*$ and $m_{h,h}^*$ are the carrier effective masses. The change Δn causes a modulation of the nominally circular polarization in the return beam and generates in the photodetectors two signals that are 180° out of phase. The signals pass through separate 46-dB gain 1–200-MHz low-noise amplifiers and are combined in a differential amplifier with 1-dB gain. Common-mode noise is virtually eliminated by this differential detection scheme.

Improvements in the probe performance are substantial. The Wollaston prism allows the use of a multimode laser diode. With a single wedge [2], static birefringence leads to a differential path delay between the two beams and mode partition noise from the laser renders the system useless. The Wollaston prism equalizes the path lengths and allows the use of a multimode laser. (The previous system used a Nd:YAG or a single-longitudinal-mode semiconductor laser.) The new system is much less sensitive to mode fluctuations giving a received signal that is more stable and depends to first order only on laser intensity. Differential detection has virtually doubled the signal voltage with only a 1.3-dB increase in the noise. Sensitivity to intensity noise in the laser is also greatly reduced. Finally, the coated lenses increase optical efficiency. The system noise floor can now be adjusted to within 2 dB of the Johnson noise limit, which in our system is about 7 dB above the shot-noise limit. The system exhibits some additional laser-induced noise caused by variations in temperature and optical feedback. A better isolator and temperature control should minimize this problem.

Modulation efficiency in this system is high enough to suggest that data communication could be accomplished using an on-chip silicon modulator. This was demonstrated using a planar silicon n-p-n transistor. We injected a 25-Mbit/s digital RZ data stream into the base of a common-emitter transistor circuit. The emitter area was $11 \times 11 \mu\text{m}^2$ and peak current was 130 mA. The applied base voltage is the lower trace in Fig. 2. The upper trace is the received optical signal after amplification without equalization when the probe beam was positioned in the base. The modulation index is 9.8 percent peak to peak relative to the static light level with a signal-to-noise ratio exceeding 6:1.

The baseline wander seen in Fig. 2 could cause timing or data errors in the receiver. This is caused by the 1-MHz low-end cutoff in the amplifier and also by heating; modulation of current changes the temperature profile near the beams and therefore the index of refraction. The dynamic response of this thermal modulation causes a frequency-dependent difference in the phase of the two beams. This appears in the received signal. The effect can be minimized by bringing the beams

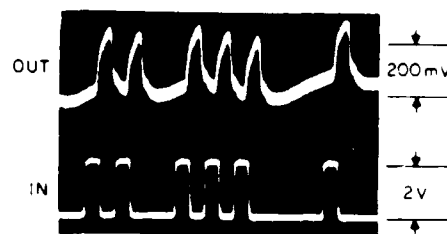


Fig. 2 Lower trace: Real-time voltage signal input to base of transistor. Upper trace: Response of system at output of differential amplifier. Horizontal scale is 50 ns/div.

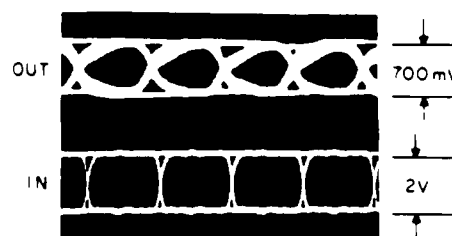


Fig. 3 Lower trace: Eye diagram of pseudorandom Manchester-coded bit stream input to base of transistor. Upper trace: Eye diagram of received optical signal. Horizontal scale is 20 ns/div.

closer together, placing them in approximately the same thermal environment. A computer model of the effect shows that, for our configuration, the thermal contribution to the observed signal is large at dc but has a corner frequency at approximately 1 MHz and then rolls off at 30 dB/decade. The thermal effect is therefore expected to be negligible at higher frequencies. This behavior is verified by experiment. However, in a different context, one may wish to use this dc sensitivity to examine remotely the temperature profile in an active integrated circuit.

Despite the thermal effect, one can use silicon as an efficient broad-band optoelectronic modulator by appropriately coding the input data stream. Manchester coding at clock rates above 5 MHz effectively eliminates the thermal effect because of the negligible spectral content of the data stream at frequencies where heating is important. The penalty is a maximum data rate reduced by half. Fig. 3 is the eye diagram of a pseudorandom optical Manchester-encoded bit stream injected into the base at 25 Mbit/s using the same configuration as for Fig. 2. The lower trace is the input eye diagram, and the upper trace is the received eye diagram. The received eye is open, with a signal-to-noise ratio of greater than 6:1, indicating an expected bit error rate of less than 10^{-9} . The associated modulation index in this planar structure is 9.8 percent. (Modulation depth for 0.8-V ECL signals in the base is typically 3–4 percent.)

This experiment suggests that optical data communication could be implemented using on-chip modulators based on the plasma optical effect. Practical systems would likely require higher data rates and monolithic optical implementation. We are currently developing new monolithic device structures that do not require external optics to achieve intensity modulation and that can operate at higher data rates. In addition, all semiconductors exhibit free-carrier optical dispersion to some degree. For example, in GaAs the small values of the effective masses and relatively large bandgap suggest that the effect will

be easily seen, if care is taken to account for the electrooptic effect.

In summary, refinements to the charge-sensing optical probe system now allow the use of a multimode 1.3- μm semiconductor laser. Differential detection increases the signal-to-noise ratio. We show that a planar silicon bipolar transistor can be used as an optical modulator using free-carrier dispersion and demonstrate a communications channel at 25 Mbit/s with a signal-to-noise ratio of 6:1 and a modulation index of 9.8 percent. We believe these improvements will lead to new methods in the testing of VLSI circuits and in the use of free-carrier dispersion for silicon optical modulators.

ACKNOWLEDGMENT

The authors wish to acknowledge M. Rodwell and R. Marsland for technical assistance.

REFERENCES

- [1] H. K. Heinrich, B. R. Hemenway, K. A. McGroddy, and D. M. Bloom, "Measurement of real-time digital signals in a silicon bipolar junction transistor using a noninvasive optical probe," *Electron Lett.*, vol. 22, no. 12, pp. 650-652, 1986.
- [2] H. K. Heinrich, D. M. Bloom, and B. R. Hemenway, "Noninvasive sheet charge density probe for integrated silicon devices," *Appl. Phys. Lett.*, vol. 48, no. 16, pp. 1066-1068, Apr. 21, 1986, also, "Erratum," vol. 48, no. 26, p. 1811, June 30, 1986.

**Generation of 7.8 ps Electrical Transients
on a
Monolithic Nonlinear Transmission Line**

M.J.W. Rodwell, C.J. Madden, B.T. Khuri-Yakub, and D.M. Bloom
Edward L. Ginzton Laboratory,
Stanford University, Stanford, CA 94305

Y.C. Pao, N.S. Gabriel
Varian III-V Device Center
Santa Clara, CA 95054

S.P. Swierkowski
Lawrence Livermore National Labs
Livermore, CA, 94550

Abstract

Picosecond electrical transients were generated by shock-wave formation on a GaAs monolithic nonlinear transmission line. An output falltime of 7.8 ps was generated by a single line driven at 15 GHz (20 ps input falltime), while 3.7:1 compression to 10.1 ps was attained for two cascaded lines.

Submitted to Electronics Letters
July 20, 1987

Picosecond pulse generators are central components for wide-bandwidth time-domain electronic measurements, including waveform sampling and picosecond metrology, and in high-speed analogue applications. Step-recovery diodes, generating $\sim 10\text{V}$ transitions of 35 ps risetime, are used for gating diode sampling bridges while tunnel diodes, with $\sim 0.2\text{V}$ transitions of 25 ps risetime, frequently generate the test pulse in time-domain reflectometers. Fast electrical transients can also be generated by nonlinear wave propagation [1-3]. Previously, we had proposed a GaAs monolithic nonlinear transmission line for compression of a 25 ps input to 4 ps output falltime, and had demonstrated compression from 500 ps to 100 ps on a 20:1 scale model [4]. We now report generation of electrical waveforms with 7.8 ps falltime on a monolithic structure.

The circuit diagram is shown in figure 1a. A transmission line with characteristic impedance $Z_1 > 50\Omega$ is periodically loaded, at electrical spacings of τ (in units of time), by Schottky varactor diodes, producing a synthetic transmission line whose characteristic impedance $Z_0(v) = \sqrt{L/C_T(v)}$ and group delay $T(v) = n\sqrt{LC_T(v)}$ are voltage-dependent. $L = Z_1\tau$ and $C_l = \tau/Z_1$ are the transmission-line inductance and capacitance per section of line, and n is the number of diodes in the line. The total capacitance per section $C_T(v) = (C_j(v) + C_l)$ where the capacitance of a step-junction diode with junction potential ϕ is $C_j(v) = C_{j0}/\sqrt{1 - v/\phi}$.

The voltage-dependence of the group velocity results in compression of the falltime of electrical wavefronts as they propagate on the line. For an input waveform having a negative-going transition with initial voltage v_h , final voltage v_l , and falltime $T_{f,in}$, the falltime at the output of the line will be [4]

$$T_{f,out} \cong \max \begin{cases} T_{f,in} - (T(v_l) - T(v_h)) \\ T_{f,min} \end{cases}$$

The minimum compressed falltime $T_{f,min} \sim \max(1/\omega_{per}, 1/\omega_{rc})$ is set predominantly by the periodic-line cutoff frequency $\omega_{per} \cong 2/\sqrt{LC_T} = 2/Z_0C_T$ and the varactor rc cutoff frequency $\omega_{rc} \cong 1/r_sC_j(v)$, where r_s is the varactor series resistance. With monolithic fabrication on GaAs, ω_{rc} and ω_{per} on the order of 0.1-1 THz are feasible [5], permitting compressed falltimes on the order of 1-10 ps.

The monolithic device (figure 1b) incorporates 42 diodes with $\phi \cong 0.8\text{V}$ and $C_{j0} = 50$

fF at 160 μm spacings ($\tau = 1.4\text{ps}$) along a 90Ω coplanar waveguide transmission line, resulting in a 140 GHz periodic-line cutoff frequency. By calculation, the characteristic impedance $Z_0(v)$ varies from 44 to 55Ω and the group delay $T(v)$ changes 25 ps as the line voltage varies from 0 to -2 volts. Circuit simulations using SPICE indicate that, given negligible diode series resistance, a 2 V step-function input with 20 ps falltime will produce an output falltime of 4 ps.

A cross-section through a diode is shown in figure 1d. Schottky diodes are formed on MBE material with a $0.6\mu\text{m}$ N- active layer ($3 \times 10^{16}/\text{cm}^3$ doping). A buried $0.8\mu\text{m}$ N+ layer ($3 \times 10^{18}/\text{cm}^3$ doping) provides both the diode cathode connection and a resistive connection between the two coplanar waveguide ground planes, suppressing the slotline mode. Fabrication requires three mask levels with $10\mu\text{m}$ design rules. Ohmic contacts having $0.03\Omega\text{-mm}$ resistivity are formed by a $0.75\mu\text{m}$ recess etch, a self-aligned (88% Au-12% Ge)/Ni/Au liftoff, and a 450°C alloy. Proton implantation [6] using both 190 keV, $6 \times 10^{14}/\text{cm}^2$ and 160 keV, $1.5 \times 10^{14}/\text{cm}^2$, provides $> 40\text{M}\Omega$ per square isolation. During implantation, a $1.6\mu\text{m}$ Au/ $1.4\mu\text{m}$ polyimide mask [6] protects the ohmic contacts and the diode active region. The interconnections are formed with a $0.1\mu\text{m}$ Ti/ $0.1\mu\text{m}$ Pt/ $1.4\mu\text{m}$ Au liftoff. Schottky diodes are formed in $10\mu\text{m} \times 10\mu\text{m}$ regions where the interconnect metal overlaps unimplanted N- material (figure 1c).

Circuit element values for the completed devices were established through I-V, C-V, and small-signal scattering parameter measurements. The diode series resistance, r_s , is 10Ω while C-V characteristics conform to those of a $C_{j0} = 50\text{fF}$, $\phi = 0.8\text{ V}$ step-junction diode shunted by a 14 fF layout capacitance. In addition, $Z_1 = 80\Omega$ and $\tau = 1.5\text{ ps}$. Series resistance of the $6.7\text{mm} \times 10\mu\text{m}$ transmission-line center conductor is 12Ω . Due to these parameter variations, $Z_0(v)$ varies from 40 to 49Ω and the group delay $T(v)$ changes 23 ps as the line voltage varies from 0 to -3 volts. The large r_s results in significant attenuation (5 dB at 15 GHz) for these prototype devices.

Because a 35 ps step-recovery diode was not available, the lines were tested with sinusoidal excitation applied through microwave wafer probes, providing a continuously adjustable input 10%-90% falltime of 0.3 cycles. The formation of shock-waves is similar to that occurring with step-function excitation. Voltage waveforms at points internal to the

structure were observed by direct electrooptic sampling [7], a noninvasive optical technique with 2 ps time resolution. A single 42- diode line reshaped a $7.5 V_{p-p}$, 15 GHz input (20 ps input falltime) to a sawtooth waveform with a compressed output falltime of 7.8 ps (figure 2). With a $8.5 V_{p-p}$, 8 GHz input (37.5 ps input falltime), two cascaded lines produced 3.7:1 compression to 10.1 ps output falltime (figure 3). In these measurements the line DC bias was set so that the diodes were on the threshold of forward conduction at the peak positive excursion of the input waveform. The 7.8 ps minimum compressed falltime is due to the 10Ω diode series resistance resulting from the $10\mu\text{m}$ spacing between ohmic and Schottky contacts. In SPICE simulations using the measured circuit parameters, a 7.6 ps falltime is predicted for $r_s = 10\Omega$, 6.0 ps for 5Ω , and 4.3 ps for 0Ω . With layout redesign, we expect to reduce r_s and to increase ω_{per} , attaining compressed falltimes approaching 1 ps.

The bandwidth of diode sampling bridges is primarily limited by the risetime of the gating pulse; with integration of a Schottky diode sampling bridge gated by a nonlinear transmission line, the bandwidth of sampling gates used in sampling oscilloscopes, network analysers, and frequency counters could be extended to 100 GHz.

Acknowledgements: This work was supported by the US Office of Naval Research under grant N00014-85-K-0381. Thanks to K.J.Weingarten for his assistance with the electrooptic measurements, and to R. Anholt (Stanford), D.C. D'Avanzo and T. Taylor (Hewlett-Packard Co.) for guidance with the proton implantation. M. Rodwell acknowledges an IBM fellowship.

References

- [1] Landauer, R. : "Parametric Amplification along Nonlinear Transmission Lines", J. Appl. Phys., 1960, Vol. 31, No. 3, pp. 479-484.
- [2] Khokhlov, R.V. : "On the Theory of Shock Radio Waves in Non-Linear Lines", *Radiotekhnika i elektronika*, 1961, 6, No.6, pp. 917-925.
- [3] Jager, D. and Tegude, F.-J. : "Nonlinear Wave Propagation along Periodic-Loaded Transmission Line", Appl. Phys., 1978, 15, pp. 393-397.
- [4] Rodwell, M.J.W., Bloom, D.M., and Auld, B.A.: "Nonlinear Transmission Line for Picosecond Pulse Compression and Broadband Phase Modulation" , Elect. Lett., 1987, Vol. 23, No. 3.
- [5] Lundien, K., Mattauch, R.J., Archer, J., and Malik, R. : "Hyperabrupt Junction Varactor Diodes for Millimeter-Wavelength Harmonic Generators", IEEE Trans. MTT-31, 1983, pp. 235-238.
- [6] D'Avanzo, D.C.: "Proton Isolation for GaAs Integrated Circuits", IEEE Trans. ED-29, 1982, pp. 1051-1058.
- [7] Kolner , B.H., and Bloom, D.M. "Electro-Optic Sampling of GaAs Integrated Circuits", IEEE J. Quantum Electron., QE-22, 1986, pp. 79-93.

Figure Captions:

Figure 1: Nonlinear transmission line circuit diagram (a), layout (b), diode top view (c), and diode cross-section (d).

Figure 2: Compression of 15 GHz input to 7.8 ps output falltime.

Figure 3: Compression of 8 GHz input to 10.1 ps output falltime with 2 cascaded lines.

53163

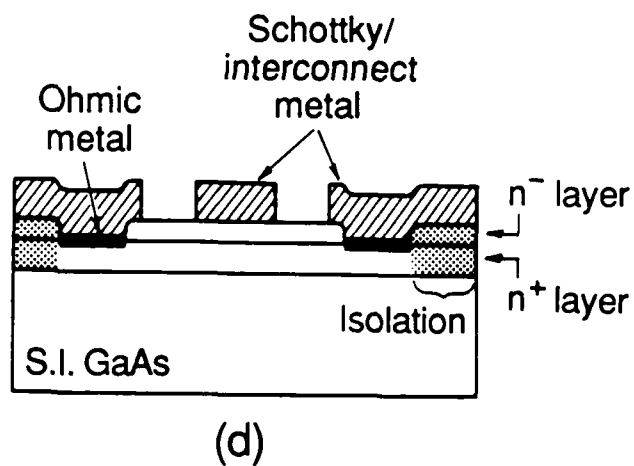
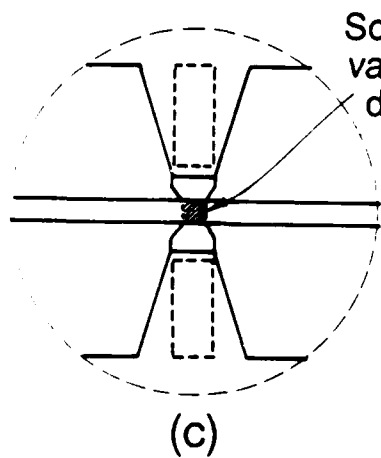
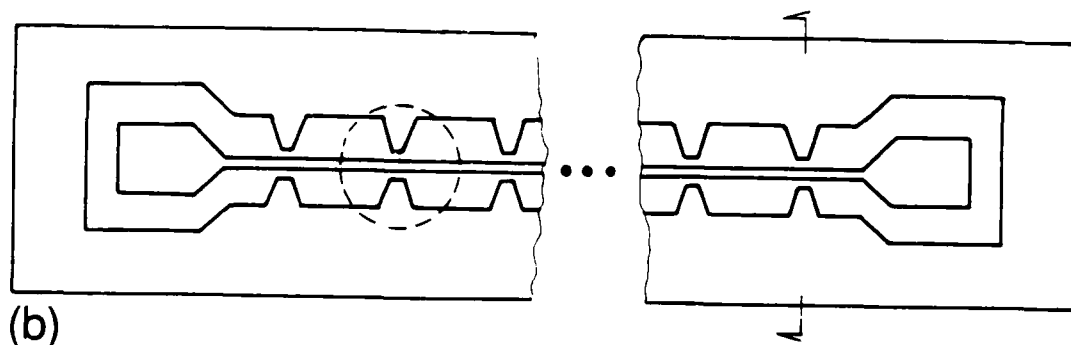
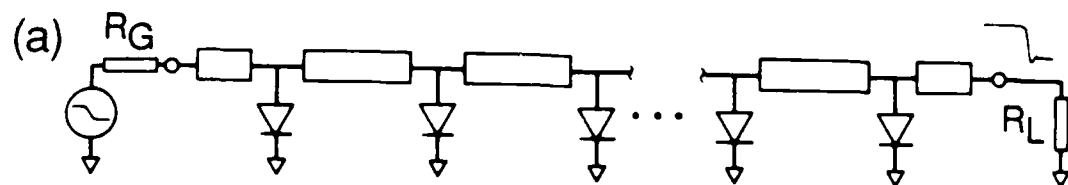


Figure 2, Radwell et al.

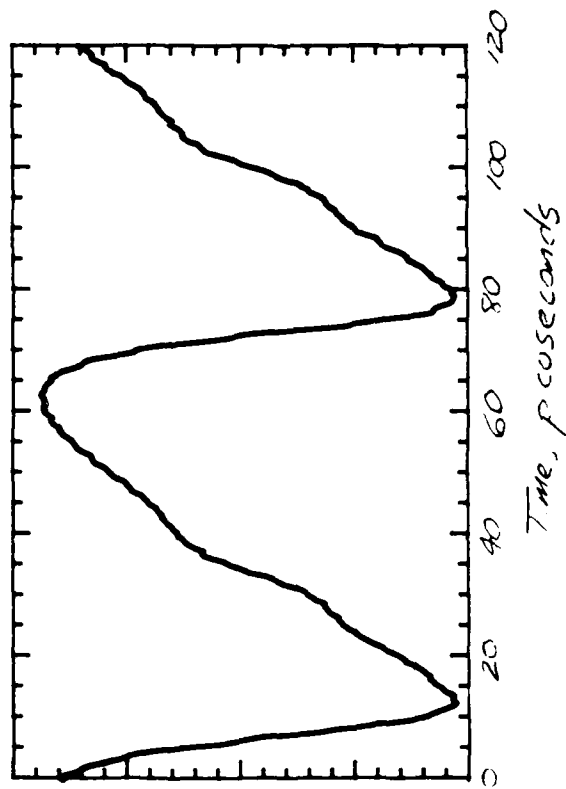
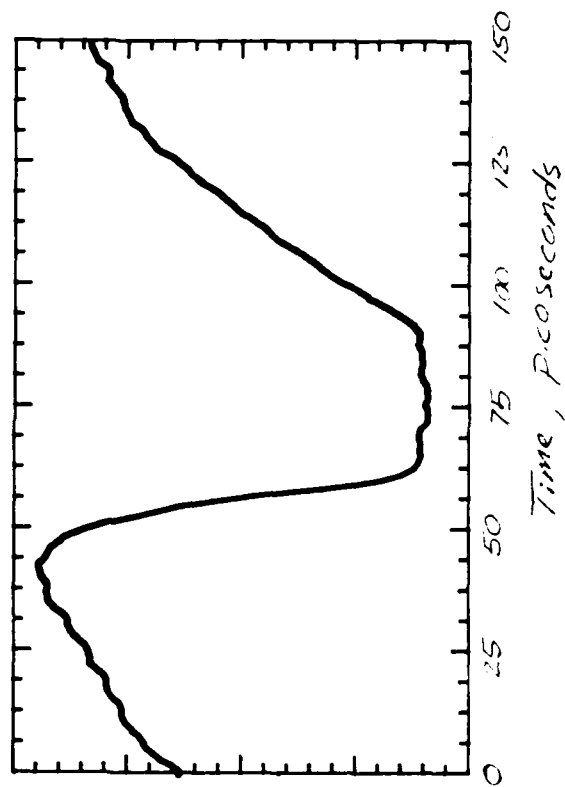


Figure 3, Rodwell et al.



Picosecond Optical Sampling of GaAs Integrated Circuits

K. J. Weingarten, M. J. W. Rodwell, and D. M. Bloom

Edward L. Ginzton Laboratory

Stanford University

Stanford, California 94305

(415) 723-0464

Invited paper to the special issue of

IEEE Journal of Quantum Electronics
on Ultrafast Optics and Electronics

Anthony M. Johnson, editor
To be published February 1988

1. Introduction

The development of advanced GaAs devices and integrated circuits has been spurred by a number of applications, including microwave and millimeter-wave radar and communication systems, fiber optic digital data transmission at gigahertz rates, high-speed data acquisition, and the constant push for faster digital logic in high-speed computers and signal processors; the IC's developed for these applications are creating new demands upon high-speed electronic instrumentation.

One demand is for increased instrument bandwidth. GaAs MESFET's have demonstrated a maximum frequency of oscillation, f_{\max} , in excess of 110 GHz [1], while pseudomorphic InGaAs/AlGaAs modulation-doped field-effect transistors [2] have shown power-gain bandwidth products which extrapolate to give $f_{\max} \approx 200$ GHz, resonant tunnelling diodes have oscillated at 56 GHz [3], and heterojunction bipolar transistors and permeable base transistors currently under development should show similar performance. Because the maximum frequency of oscillation of these devices is often greater than the 100 GHz bandwidth of commercial millimeter-wave network analyzers, f_{\max} is estimated by extrapolation from measurements at lower frequencies. Used as switching elements, propagation delays and transition times of 1-10 ps should be expected for these devices, well below the resolution of commercial sampling oscilloscopes. In either case the device bandwidth exceeds that of the measurement instrument.

A second demand is for noninvasive access to the internal signals within high-speed integrated circuits. GaAs digital integrated circuits of MSI (medium-scale integration) complexity and 1-5 GHz clock rates are now available commercially, as are GaAs monolithic microwave integrated circuits (MMIC's) of SSI (small-scale integration) complexity and 1-26 GHz bandwidths. More complex LSI (large-scale integration) digital circuits are under development, and experimental SSI digital circuits operating with 18 GHz clock rates [4] have been demonstrated. In contrast to silicon LSI integrated circuits operating at clock rates in the tens and hundreds of megahertz, the development of GaAs high-speed circuits is hampered both by poorly refined device models and by layout-dependent circuit parasitics associated with the high frequencies of operation. A test instrument providing noninvasive measurements within the integrated circuit would permit full characterization of such complex high-speed IC's.

These issues have motivated a number of researchers to investigate alternative test techniques, both to increase measurement bandwidth and to allow internal testing of IC's. This paper begins with a review of conventional test methods and instruments, summarizes several new test techniques for IC's, and then describes in detail the principles, capabilities, and IC measurement results of direct electrooptic sampling, a measurement technique that allows for internal-node voltage measurements in GaAs IC's with picosecond time resolution, corresponding to bandwidths in excess of 100 GHz.

1.1. Electrical test methods

We begin by considering the limitations of conventional test instruments. Their capabilities and characteristics are determined by two features - the IC probe that connects the test instrument to the circuit and the test instrument itself. The IC probe has its own intrinsic bandwidth that may limit the test method. In addition, the probe also determines an instrument's ability to probe *internal* to the IC due to its size (limiting its spatial resolution) and influence on circuit performance (loading of the circuit from its characteristic and parasitic impedances.) The test instrument sets the available bandwidth given perfect IC probes or packaged circuits, and defines the type of electrical test, such as measuring time or frequency response.

Connection of a test instrument to an IC begins with the external connectors, typically 50 Ω coaxial cable with a microwave connector, such as SMA and APC-3.5, standard microwave connectors, or K-connector and APC-2.4, newer connectors for 46 GHz (K) or 50 GHz (APC 2.4) operation. The IC probes are the *transitions* from the coaxial cable to some type of contact point with a size comparable to an IC bond pad. Low-frequency signals are often connected with needle probes. At frequencies greater than several hundred megahertz these probes have serious *parasitic* impedances, due to shunt capacitance from fringing fields and series inductance from the long, thin needle. The parasitic impedances and the relatively large probe size compared to IC interconnects limit their effective use to low-frequency external input or output circuit responses at the bond pads. For signals greater than several hundred megahertz, the recently developed Cascade Microtech probe [5,6] has demonstrated IC connections to millimeter-wave frequencies of 50 GHz. The probe consists of a coaxial connector with a transition to 50 Ω coplanar waveguide (CPW) transmission line that then tapers to bond pad size contacts. They offer good microwave performance, but their size limits test points to IC bond pads and their 50 Ω characteristic impedance limits their use to input or output sections of the IC.

Thus, electrical probes suffer from a measurement dilemma. Good high-frequency probes use transmission lines to control the line impedance from the coaxial transition to the IC bond pad and to reduce parasitic impedances. The low characteristic impedance of such lines (typically 50 Ω) limits their use to input/output connections. High-impedance probes suitable for probing intermediate circuit nodes have significant parasitic impedances at microwave frequencies, severely perturbing the circuit operation and affecting the measurement accuracy. In both cases, the probe size is large compared to IC interconnect size, limiting their use to test points the size of bond pads.

Conventional test instruments for measuring high-speed electrical signals consist of sampling oscilloscopes, spectrum analyzers, and network analyzers. Sampling oscilloscopes measure the time response of repetitive signals with a resolution as short as 25 ps or a bandwidth of 14 GHz. Combined with transmission line probes this instrument gives either time domain reflectometry measurements or signal waveforms of an IC's external response, but has neither the time resolution required for state-of-the-art GaAs IC's nor the ability to measure the internal node response of MSI or LSI IC's. A promising note is the recent introduction of a new sampling oscilloscope based on Josephson Junction superconducting technology [7] with a time resolution of about 8 ps. As with slower sampling oscilloscopes, however, the 50 Ω connectors limit its use to external characterization of IC's.

Spectrum and network analyzers measure the response of circuits in the frequency domain, with a range of 26.5 GHz typically and limited extension through the millimeter-wave frequencies to 300 GHz. A spectrum analyzer measures the power spectrum of a signal, while network analyzers measure the vector transfer function of a network (magnitude and phase) as a function of frequency. The small-signal, linear characteristics of microwave devices and circuits measured with a network analyzer are usually expressed in terms of the scattering parameters. These provide a measure (often extrapolated) of f_{max} , a device's maximum frequency of oscillation, and f_T , the unity current gain frequency, figures of merit of a device's operation speed. The frequency range of these instruments can be extended to millimeter-wave frequencies (300 GHz for the spectrum analyzer, 100 GHz for the network analyzer) using external source multipliers, mixers and waveguide connectors, but the frequency coverage is limited to 1.5:1 waveguide bandwidths and the waveguide connectors require a hybrid mount of the IC in a waveguide package, preventing wafer testing of the IC. Network analyzers can provide time-domain measurements of a network's small-signal step or impulse response by Fourier transforming the small-signal frequency-domain two-port device parameters. For large-signal measurements, where the network is no longer linear, the principle of superposition cannot be applied, preventing calculation of the large-signal time-domain response from measurements of frequency-domain transfer functions. For example, the network analyzer cannot measure the time waveform response of the IC's due to amplifier saturation. Although spec-

trum analyzers can measure the harmonic spectrum magnitude of saturated or large-signal circuit responses, the phases of the harmonics are not measured, and the large-signal time waveforms again cannot be inferred. Both instruments also rely on 50 Ω connectors and IC probes, limiting their ability to probe an IC to its external response. For network analysis, a further issue is de-embedding the device parameters from the connector and circuit fixture response, a task which grows progressively more difficult at increasing frequencies, particularly for millimeter-wave testing.

1.2. Non-Electrical, Novel test techniques

With the objective of either increased bandwidth or internal IC testing with high spatial resolution (or both) a number of new test techniques have been introduced and demonstrated. One method of measuring a voltage on IC conductors is to energy analyze secondary electron emission. To test logic level signals in VLSI silicon IC's researchers in the late 1960's developed the voltage contrast scanning electron microscope (SEM) or E-beam probing [8,9]. This technique uses an electron beam from an SEM to stimulate secondary electron emission from surface metallization. For a metal conductor at ground or negative potential, the electrons have sufficient energy to be collected by a detector shielded by an energy analyzer grid. Metal lines at a positive potential retard the emitted electrons, lowering their energy and reducing the number of electrons detected. The detected signal is small for IC voltage levels; to improve time resolution the signal is sampled with electron beam pulses and averaged to improve signal-to-noise ratio.

Commercial SEM's have sensitivities of 1-10 mV, bandwidths up to 2 GHz or time resolutions of ≈ 1 ns, and a spatial resolution as small as 20 nm. Compared to typical operating speeds of commercial silicon VLSI (clock rates of 10 to 100 MHz) this technique has good time resolution, acceptable sensitivity, and excellent spatial resolution. The system's time resolution is set by gating the E-beam from the thermionic cathodes of standard SEM's. For decreasing electron beam duration required for increased time resolution, the average beam current decreases, degrading measurement sensitivity and limiting practical systems to a time resolution of several hundred picoseconds. To overcome this limitation, a technique which implements a photocathode triggered by an intense picosecond optical pulse to generate short, high-current electron pulses [10] has been demonstrated. This approach shows promise for achieving time resolution approaching 10 ps with the SEM probe. The major drawbacks of SEM testing are its complexity and its relatively high cost.

Photoemissive sampling, based on analyzing secondary electron emission from IC conductors similar to E-beam testing, uses intense, energetic light from a pulsed laser focused on an IC conductor to generate photoelectrons. An extraction/retarding grid combination placed in close proximity to the conductor energy analyzes the electrons, with a resulting secondary electron emission varying with the conductor potential. The feasibility of this new approach is made possible by picosecond pulsewidth, high peak power lasers, and offers a potential improvement in time resolution and sensitivity over the SEM probe. The technique is not available commercially, but a number of researchers have demonstrated systems with time resolution as short as 7 ps with good spatial resolution and millivolt sensitivity [11,12,13]. With both electron-beam and photoemissive sampling, electron beams and electron extraction fields can produce charge concentrations within the semiconductor substrate through charging of deep levels, or at its surface, through field-induced surface inversion.

A technique which optically senses free-carrier charge density was recently developed for measurements within silicon IC devices [14,15]. Because of its centrosymmetric crystal structure, silicon exhibits no bulk second-order optical nonlinearities, such as the electrooptic effect, to use as a basis for an optical measurement system. Third-order effects, such as voltage-dependent second-harmonic generation or the optical Kerr effect, are in general very weak and result in

impractical systems in terms of measurement sensitivity and implementation. Most semiconductor devices function by modulating charge density within a control region, which contributes to material index of refraction as described by the plasma-optical relation

$$n = n_0 \left(1 - \frac{\omega_p^2}{\omega^2} \right)^{\frac{1}{2}} \quad (1)$$

$$\omega_p^2 = \frac{q^2 N}{\epsilon_s m_e^*} + \frac{q^2 P}{\epsilon_s m_h^*} \quad (2)$$

where n_0 is the bulk index of refraction, ω is the optical probe frequency, ω_p is the plasma resonance frequency, N is the electron concentration in the conduction band, P is the hole concentration in the valence band, ϵ_s is the permittivity of the substrate material, and m_e^* and m_h^* are the electron/hole conductivity effective masses. The change in charge density is detected with a compact optical interferometer using a 1.3 μm wavelength (the absorption minimum in silicon) semiconductor laser as the probe, shown schematically in Fig. 1. In contrast to electrooptic techniques, where typical probe beam intensity modulation is on the order of 0.1%, for the charge density typical of integrated silicon bipolar transistors the probe beam modulation in the charge-sensing system is on the order of 1%. This sensitivity has allowed the demonstration of single-shot (i.e. no repetitive sampling) detection of a silicon bipolar junction transistor's switching signal in a 200 MHz bandwidth (Fig. 2). Since the plasma-optical effect occurs in all semiconductor materials, this technique is applicable to GaAs IC's and shows promise for studying device characteristics and charge dynamics.

Another optical probe scheme is electrooptic sampling, which uses an electrooptic light modulator to intensity modulate a probe beam in proportion to a circuit voltage. The technique was initially developed to measure the response of photoconductors and photodetectors faster than the time resolution of sampling oscilloscopes [16,17,18,19] and used an external electrooptic modulator (typically lithium tantalate, LiTaO₃) connected to the device under test. A polarized optical probe beam passes through an electrooptic crystal, whose index of refraction changes due to the presence of an electrical signal (Fig. 3.) The polarization of the light after passing through the electrooptic crystal depends on the signal driving the modulator, and passing the probe beam through a polarizer results in a signal-dependent intensity modulation. The approach exhibits excellent time resolution (<0.5 ps) due to the advanced level of ultrashort pulse generation with the colliding-pulse mode-locked (CPM) laser and the very high intrinsic speed of the electrooptic effect. Combined with a cryogenic system, optical measurements of electrical signals have been made at liquid helium temperatures[20]. However, the hybrid lithium tantalate electrooptic modulator requires connecting the test point on the IC to the transmission line of the modulator, restricting its use to external test points. Unless carefully designed, the system's time resolution is degraded by the hybrid connection between the modulator and the device under test, due to the loading of the test point from the relatively low characteristic impedance of the transmission line, and due to the parasitic impedances of bond wires.

Using an electrooptic needle probe (Figs. 4&5) [21], the technique has been extended to internal node probing of IC's. The needle, a fused silica rod with a 40 x 40 micron tip of LiTaO₃ coated for high reflection of the probe beam, is brought close to a conductor, introducing fields within the probe tip. As with the hybrid electrooptic scheme, the electric fields change the polarization of the probing beam, and the reflected beam is analyzed by a polarizer. The LiTaO₃ electrooptic material, transparent to visible wavelength light, allows the use of ultrashort sampling pulses

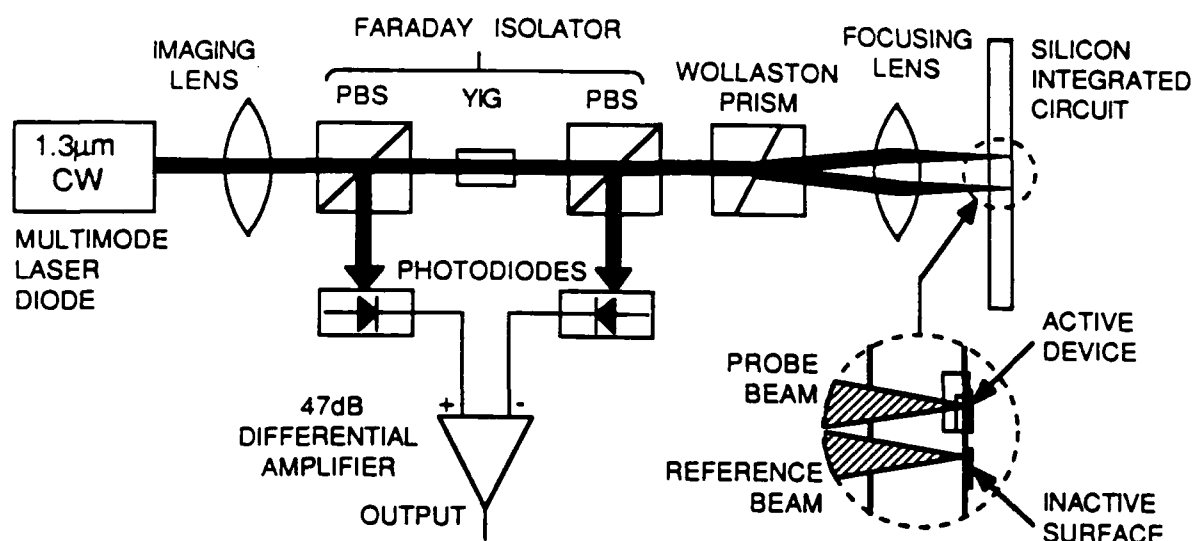


Figure 1: Charge-sensing system schematic [14,15]. The Wollaston prism separates the input beam into a probe beam and a reference beam. The presence of charge in the probe beam path results in a change in output intensity at the photodiodes proportional to the charge concentration, as described in the text. PBS denotes a polarizing beamsplitter cube.

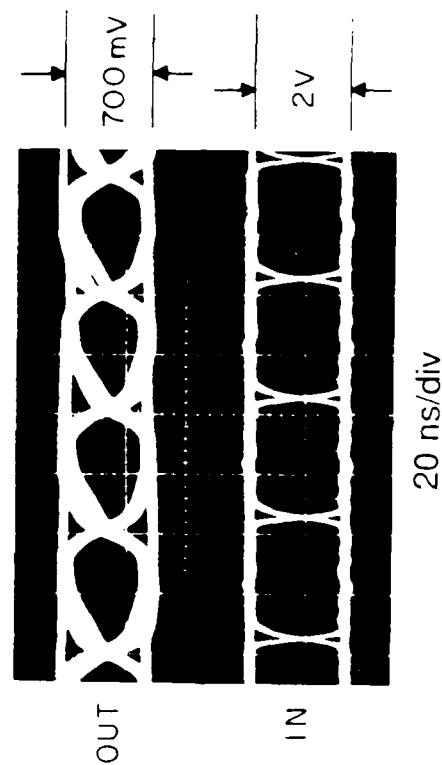


Figure 2: Eye diagram of the stored base charge in a silicon bipolar junction transistor, as monitored by the optical charge sensing system, upper trace. The corresponding base voltage is shown in the lower trace. The input signal is 25 Megahertz pseudo-random Manchester-coded data. Time scale is 20 ns per division.

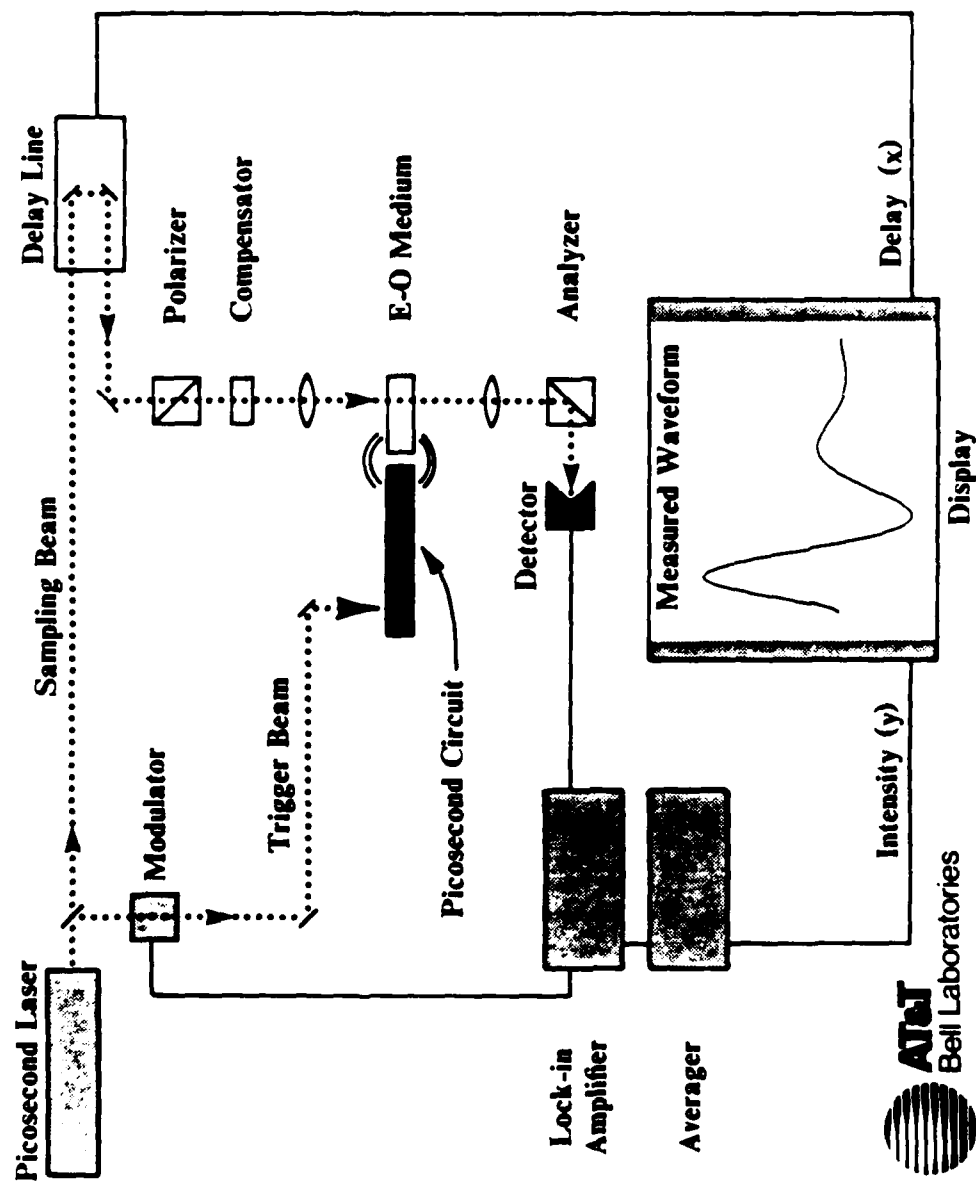


Figure 3: Electrooptic sampling system [18]. Courtesy of J.A. Valdmanis, AT&T Bell Laboratories.

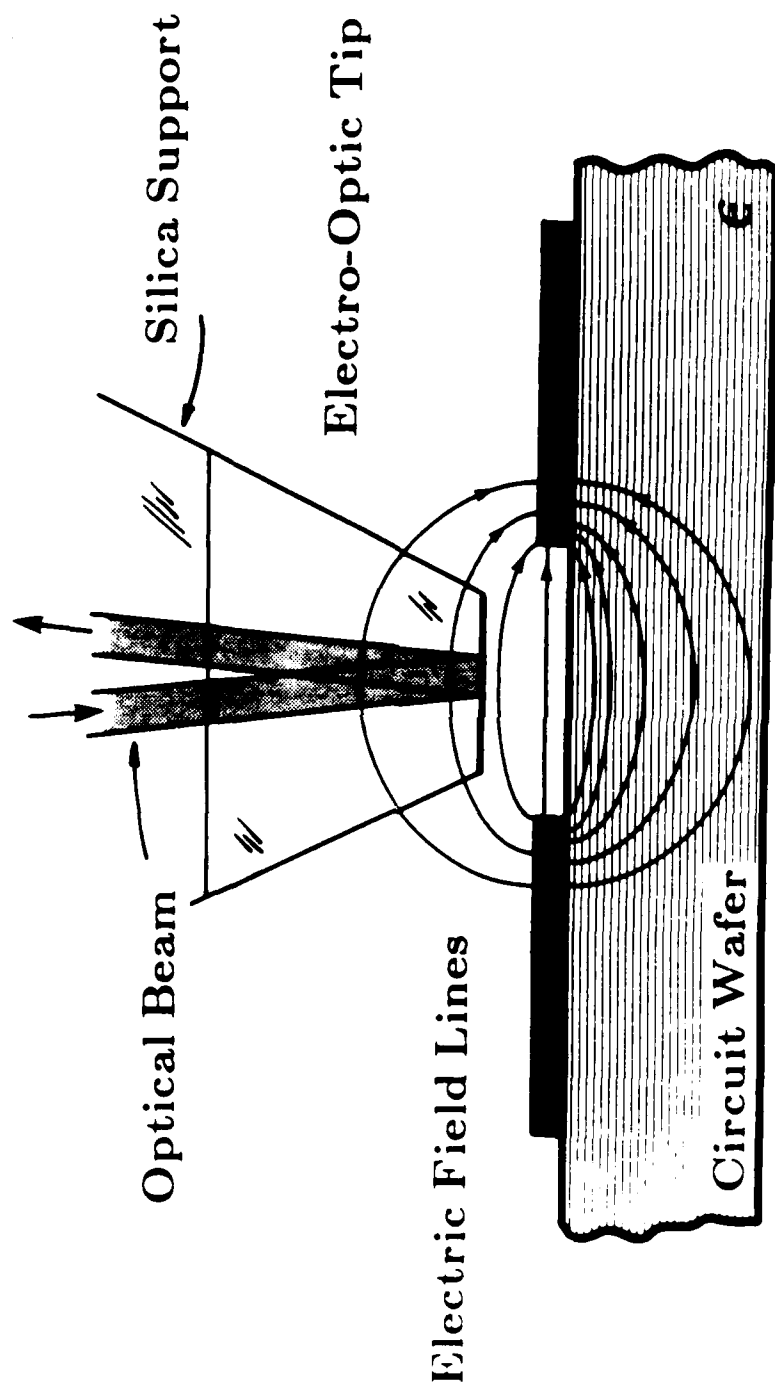


Figure 4: Electrooptic needle probe for on-wafer measurements [21,22]. Courtesy of J.A. Valdmanis, AT&T Bell Laboratories.

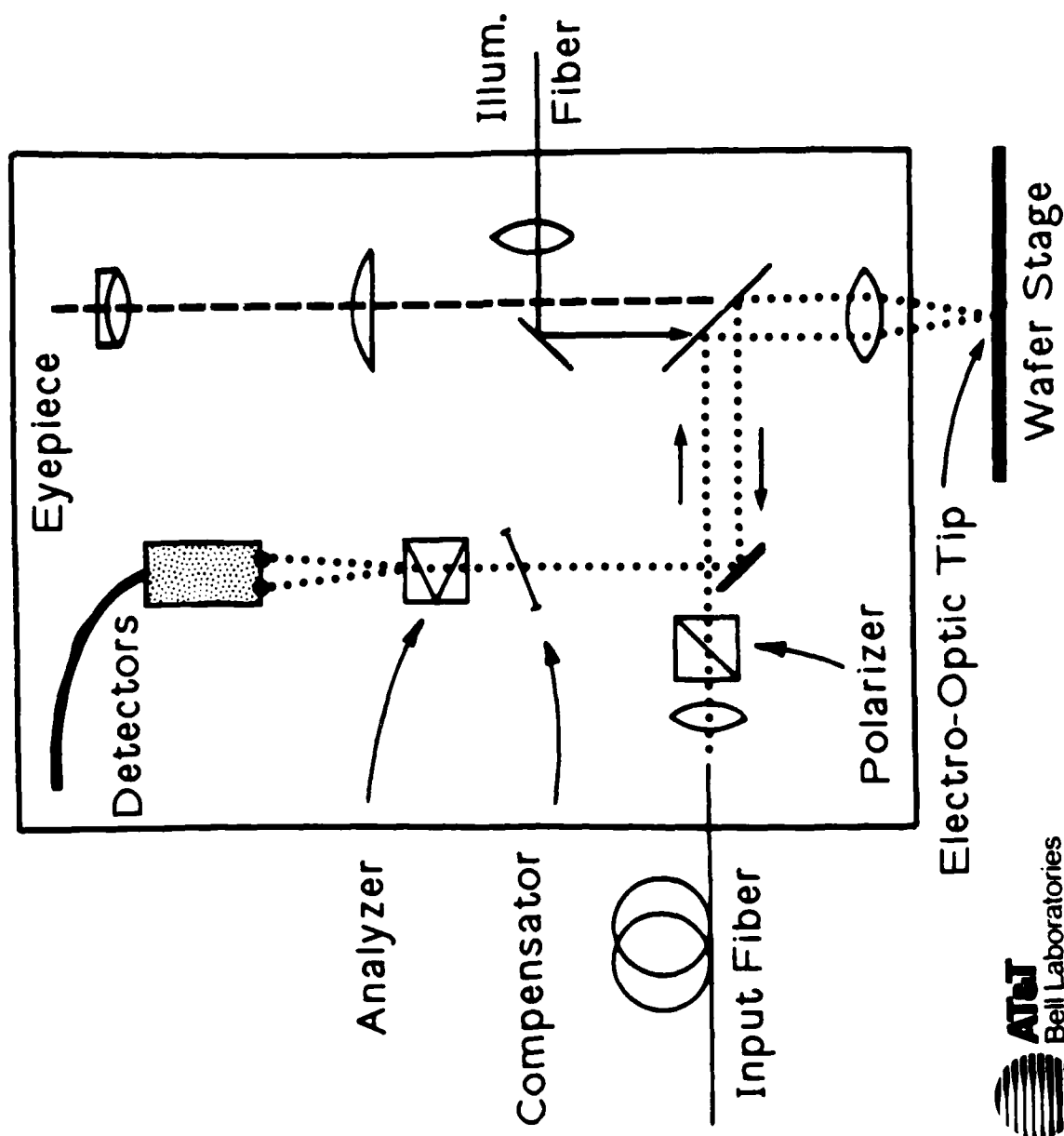


Figure 5: Sampling system for on-wafer measurements with the electrooptic needle probe. Courtesy of J.A. Valdmann, AT&T Bell Laboratories.

from a CPM laser; a step response risetime of less than 300 fs has been demonstrated[22,23]. Because the probe relies on no optical or electrical properties of the circuit under test, circuits of any substrate material can be tested without sample preparation. The probe exhibits some small circuit invasiveness through capacitive loading on the order of 10 femtofarads due to the proximity of the LiTaO₃ probe tip of dielectric constant $\epsilon_r = 40$. The polarization shift in lithium tantalate, proportional to the lateral electric field, may make the probe sensitive to signals from nearby conductors in addition to the potential of the probed conductor.

The external electrooptic sampling techniques described above can provide signal measurements with subpicosecond time resolution (equivalent to bandwidths of approaching 1 THz.) Direct electrooptic sampling, a related technique where the substrate of the GaAs circuit under test serves as the electrooptic modulator, eliminates the electrical parasitics associated with external electrooptic elements and provides voltage measurements of points internal to the IC with picosecond time resolution and micron spatial resolution. This method's principles, capabilities, and circuit measurement results are described in the following sections.

2. Principles of Direct Electrooptic Sampling in GaAs IC's

The electrooptic effect, an anisotropic variation in a material's dielectric constant due to an applied electric field, is present in a variety of non-centrosymmetric crystals. Among these are GaAs, InP and AlAs, used for high-speed semiconductor devices, and lithium niobate (LiNbO₃), lithium tantalate (LiTaO₃) and potassium dihydrogen phosphate (KH₂PO₄), used for nonlinear optical devices. Centrosymmetric crystals do not exhibit the electrooptic effect; notable among these materials are silicon and germanium. The change in refractive index of electrooptic materials with electric field can be used for optical phase-modulation, and, from this, polarization-modulation or intensity-modulation [24,25]. Direct electrooptic sampling uses the electrooptic effect in GaAs to obtain voltage-dependent intensity modulation of a probe beam [26,27]. As with other experimental probing methods, a pulsed optical probe beam permits a time resolution on the order of one picosecond or instrument bandwidths greater than 100 GHz.

Without external electrooptic elements, the invasive properties of those elements are eliminated, permitting probing with no electrical contact, no loading of the test point with low-impedance transmission lines, and no parasitic probe impedance. Because the probing beam can be focused to a spot of diameter of several microns, the probe's spatial resolution allows access to finely-spaced conductors in LSI GaAs circuits. Direct electrooptic sampling thus provides the bandwidth, the spatial resolution, and the internal-node access necessary for characterization of high-speed GaAs integrated circuits.

2.1. Electrooptic Voltage Probing in a GaAs Crystal

GaAs is one of simplest electrooptic crystals, a zincblende with crystal symmetry $\bar{4}3m$. Its cubic structure results in no natural (field-free) birefringence and a symmetric electrooptic tensor with equal-valued elements. The electrooptic tensor in GaAs is [28]

$$r_{jk} = \begin{pmatrix} 0 & 0 & 0 \\ 0 & 0 & 0 \\ 0 & 0 & 0 \\ r_{41} & 0 & 0 \\ 0 & r_{41} & 0 \\ 0 & 0 & r_{41} \end{pmatrix} \quad (3)$$

An applied electric field induces a birefringence described by the index ellipsoid

$$\frac{x^2}{n_0^2} + \frac{y^2}{n_0^2} + \frac{z^2}{n_0^2} + 2r_{41}yzE_x + 2r_{41}xzE_y + 2r_{41}xyE_z = 1 \quad (4)$$

where n_0 is the zero-field refractive index, r_{41} is the electro-optic coefficient for GaAs, and E is the applied electric field in the direction indicated by its subscript. The intersection of the index ellipsoid and a plane normal to the optical propagation direction defines an ellipse whose major and minor axes give the allowed (eigenvector) polarization directions and their refractive indices.

To relate this to an IC substrate, Fig. 6 shows the principal crystal axes of a GaAs IC fabricated on standard (100)-cut material. The X, Y, and Z axes are aligned with the $\langle 100 \rangle$ directions of the GaAs cubic Bravais lattice, while the Y' and Z' axes are aligned with the $[01\bar{1}]$ and $[011]$ directions parallel to the cleave planes of the a GaAs wafer (along which individual IC's are scribed) and 45° to the $[010]$ and $[001]$ directions. For an optical plane wave traveling in the X direction, the intersection of the index ellipsoid and the $x=0$ plane normal to its direction of propagation defines an ellipse in the (Y', Z') plane

$$y'^2 \left(\frac{1}{n_0^2} + r_{41} E_x \right) + z'^2 \left(\frac{1}{n_0^2} + r_{41} E_x \right) = 1 \quad (5)$$

The Y' and Z' axes are the eigenvectors of the electrooptic effect and form the natural coordinate system for describing electrooptic sampling in GaAs IC's. The refractive indices $n_{y'}$ and $n_{z'}$ in the Y' and Z' directions are

$$n_{y'} = n_0 - \frac{n_0^3 r_{41} E_x}{2} \quad (6a)$$

$$n_{z'} = n_0 + \frac{n_0^3 r_{41} E_x}{2} \quad (6b)$$

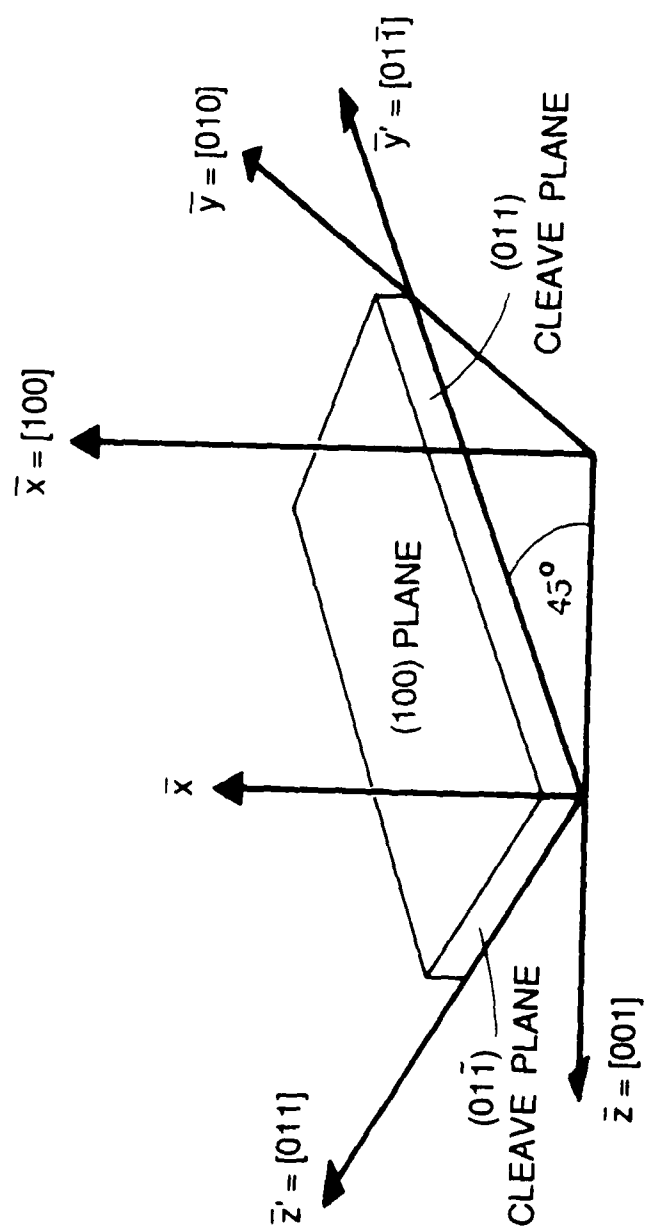


Figure 6: Principal axes and cleave planes in (100)-cut Gallium Arsenide.

and these field-dependent refractive indices result in differential phase shift for beam polarizations in the Y' and Z' directions.

Consider the transmission electrooptic amplitude modulator shown in Fig. 7. A circularly-polarized plane wave propagating through the substrate receives a change in phase between the Y' and Z' polarizations due to the electrooptic effect in proportion to the electric field given by

$$\Delta\phi = \frac{2\pi n_0^3 r_{41}}{\lambda_0} E_x W = \frac{2\pi n_0^3 r_{41}}{\lambda_0} V \quad (7)$$

such that the beam emerging from the substrate has changed from circular to slightly elliptical polarization. Note that the product $E_x W$ of the substrate thickness and the x-component of the electric field is the potential difference V between the front and back surfaces of the GaAs wafer where the probing beam traverses the wafer. This result holds for a general field distribution; a plane-wave optical beam propagating along a $\langle 100 \rangle$ direction experiences a change in phase shift proportional to product of the longitudinal electric field and the substrate thickness, i.e. it is *only* affected by the potential difference V across the wafer at the probe point.

To measure this voltage-induced polarization change, the beam emerging from the GaAs is passed through a polarizer oriented at 45° to the Y' and Z' axes. The intensity of the output beam is then

$$\begin{aligned} P_{\text{out}}(V) &= P_0 \left[1 + \sin \left(\frac{2\pi}{\lambda_0} n_0^3 r_{41} V \right) \right] \\ &= P_0 \left[1 + \sin \left(\frac{\pi V}{V_\pi} \right) \right] \end{aligned} \quad (8)$$

where P_0 is the output intensity with zero field in the substrate. V_π , called the half-wave-voltage, and given by

$$V_\pi = \frac{\lambda_0}{2 n_0^3 r_{41}} \quad (9)$$

is the voltage required for 180° phase shift between the Y' and Z' polarizations. For GaAs, $V_\pi \approx 10$ kV at a wavelength of $1.064 \mu\text{m}$ for $n_0 = 3.6$, and $r_{41} \approx 1.4 \times 10^{-12}$ [29]; the argument of the sine expression is thus small for typical voltages V on integrated circuits, and Eqn. 8 can be approximated by

$$P_{\text{out}} \approx P_0 \left[1 + \frac{\pi V}{V_\pi} \right] \quad (10)$$

Thus for substrate voltages to several hundred volts, the output beam intensity is nearly linear and in direct proportion to the voltage across the substrate. The intensity of the output beam, detected by a photodiode, is thus a measure of the voltage across the substrate of the IC.

2.2. Probing geometries in GaAs IC's

The transmission modulator of Fig. 7 requires separate lenses for focusing and collecting the probe beam, precisely aligned on opposite sides of the wafer for IC measurements. Also, high-density interconnections on the circuit side of digital IC's and backside metallization on many microwave IC's would obstruct the beam passage through the wafer. Reflection-type probing geometries as shown in Fig. 8 provide better access to IC's, using a single lens for focusing and using the IC metallization for reflection. The frontside geometry is suitable for probing microstrip transmission lines of MMIC's. The backside geometry permits very tight focusing of the probing beam to a diameter limited by the numerical aperture of the focusing lens, and provides a probe beam modulation sensitive to the probed conductor's voltage but independent of nearby signal conductors [30], a necessity for testing high-density IC's.

For microstrip transmission lines typically used in MMIC's, the fields extend laterally from the conductor roughly a distance equal the substrate thickness; the probe beam is focused from the top of the substrate through the fringing fields of the conductor to a beam spot size diameter approximately one-tenth of the substrate thickness so that it overlaps well with the fringing fields. Other MMIC's use planar transmission lines such as coplanar waveguide (CPW) for microwave interconnects. MSI/LSI circuits typically use thin metal lines (3 to 10 μm); the electric field distribution around the conductors is a strong function of their layout. For these types of interconnects and for planar transmission lines, the extent of the fields into the substrate is on the order of the distance between signal conductors and grounds. Typical IC substrate thickness (400 to 500 μm) is much greater than conductor spacings; the electric fields lie near the substrate surface, and the back of the substrate is nearly at an equipotential with respect to individual conductors on the IC surface. The optical probe, focused through the back of the substrate to a spot diameter less than or equal to the conductor width, is modulated by the voltage on the conductor nearly independent of signals from nearby conductors.

In both cases the optical probe is reflected from metallization on the IC. The signal is proportional to the amount of light reflected, and if the reflectivity of the metallization varies, the signal strength also varies. The signal can be normalized to the amount of reflected light, but metallization such as ohmic contacts, which may be very rough, will cause poor signal sensitivity if a large fraction of the probe beam is scattered. Because integrated circuits are patterned by optical lithography, the wafer top surface has good optical quality. For backside probing the back of the wafer must be polished to allow passage of the probe beam with negligible scattering. For frontside probing the ground plane should be sufficiently reflective to provide a good return beam - most MMIC's we have encountered have shown adequate ground-plane reflectivity.

In reflection-mode probing, the incident and reflected beams, centered on the microscope lens for optimum focusing, can be separated by manipulation of their polarizations (Fig. 9.) The advantages of this arrangement for IC probing are ease-of-alignment, on-axis focusing for diffraction-limited spot size, and efficient use of the optical signal (in contrast to using a beamsplitter to separate the incident and return beams, which attenuates half the optical power on each pass.) The polarization states of this arrangement may be analyzed by Jones calculus, and are qualitatively described as follows. A linearly polarized probe beam from the polarizing beamsplitter passes through a quarter-waveplate, oriented at 22.5° to the axis of the beamsplitter, producing an elliptical polarization. A half-waveplate oriented at 33.75° then rotates the elliptical polarization an additional 22.5° to align its major axis at 45° to the [011] direction of the GaAs substrate (i.e. oriented at 45° to the substrate cleave planes.) The on-axis probe beam is focused by a microscope objective next to a conductor (frontside probing) or on the conductor (backside probing.) The reflected beam passes back through the lens and the waveplates, producing a linear polarization at 45° to the axes of the polarizing beamsplitter, and the polarization component at 90° orientation is directed by the beamsplitter onto a photodiode. The probed

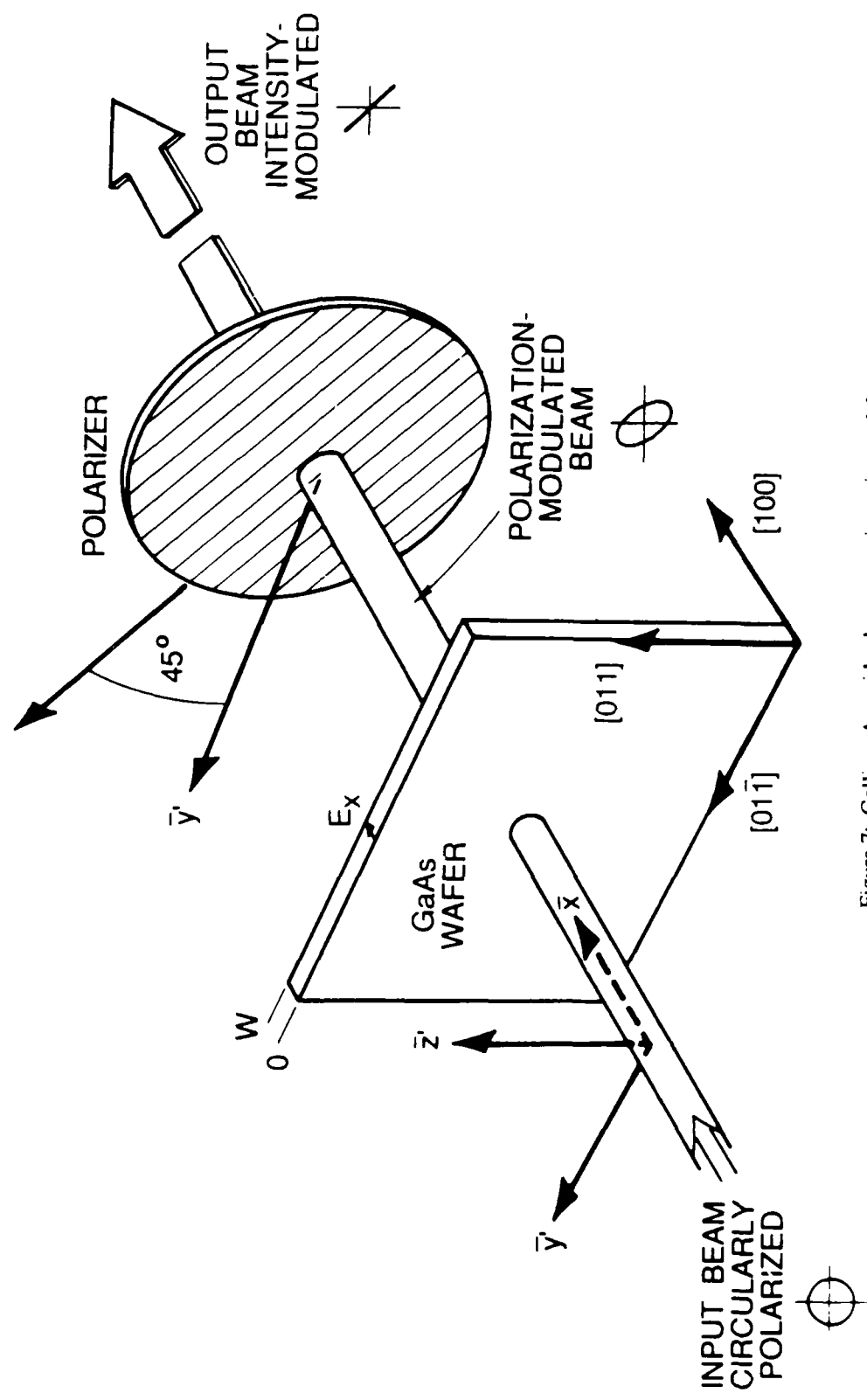
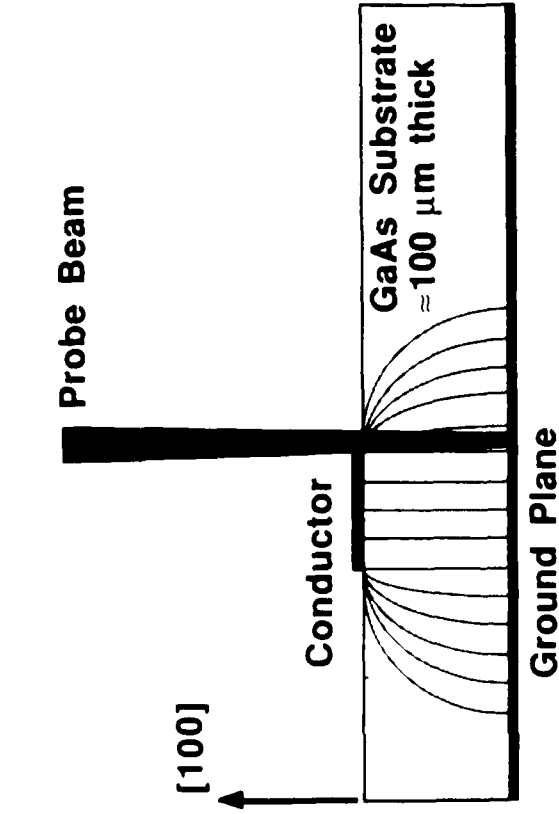


Figure 7: Gallium Arsenide electrooptic intensity modulator.

Frontside Probing



Backside Probing

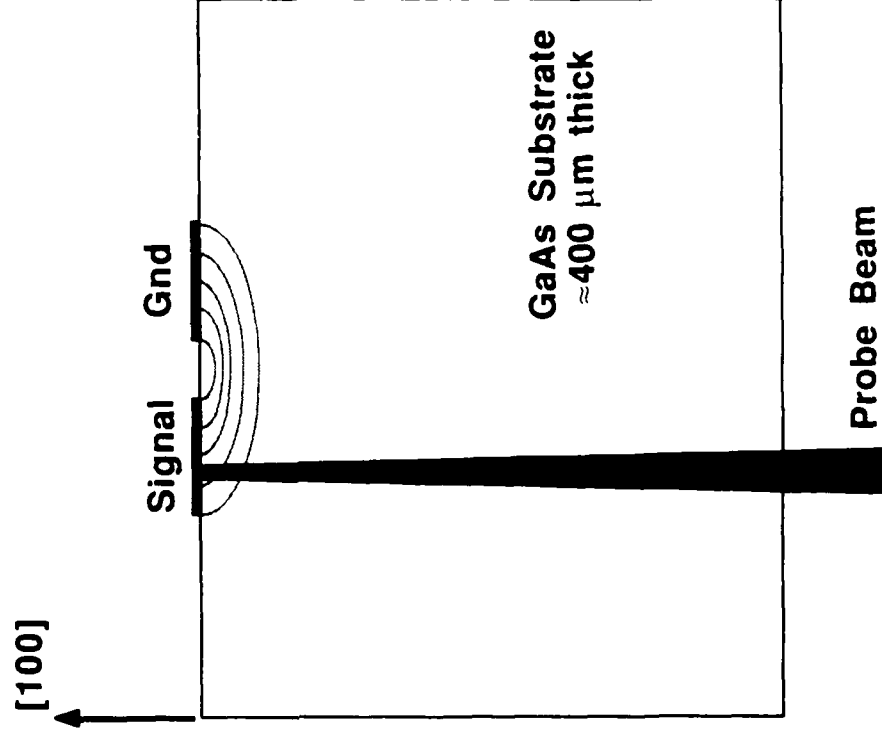


Figure 8: Reflection-mode probing geometries for electrooptic sampling of GaAs integrated circuits. The frontside geometry is used for probing microstrip transmission lines on MMIC's, while the backside geometry is used for probing planar transmission lines on MMIC's and interconnects lines on digital IC's.

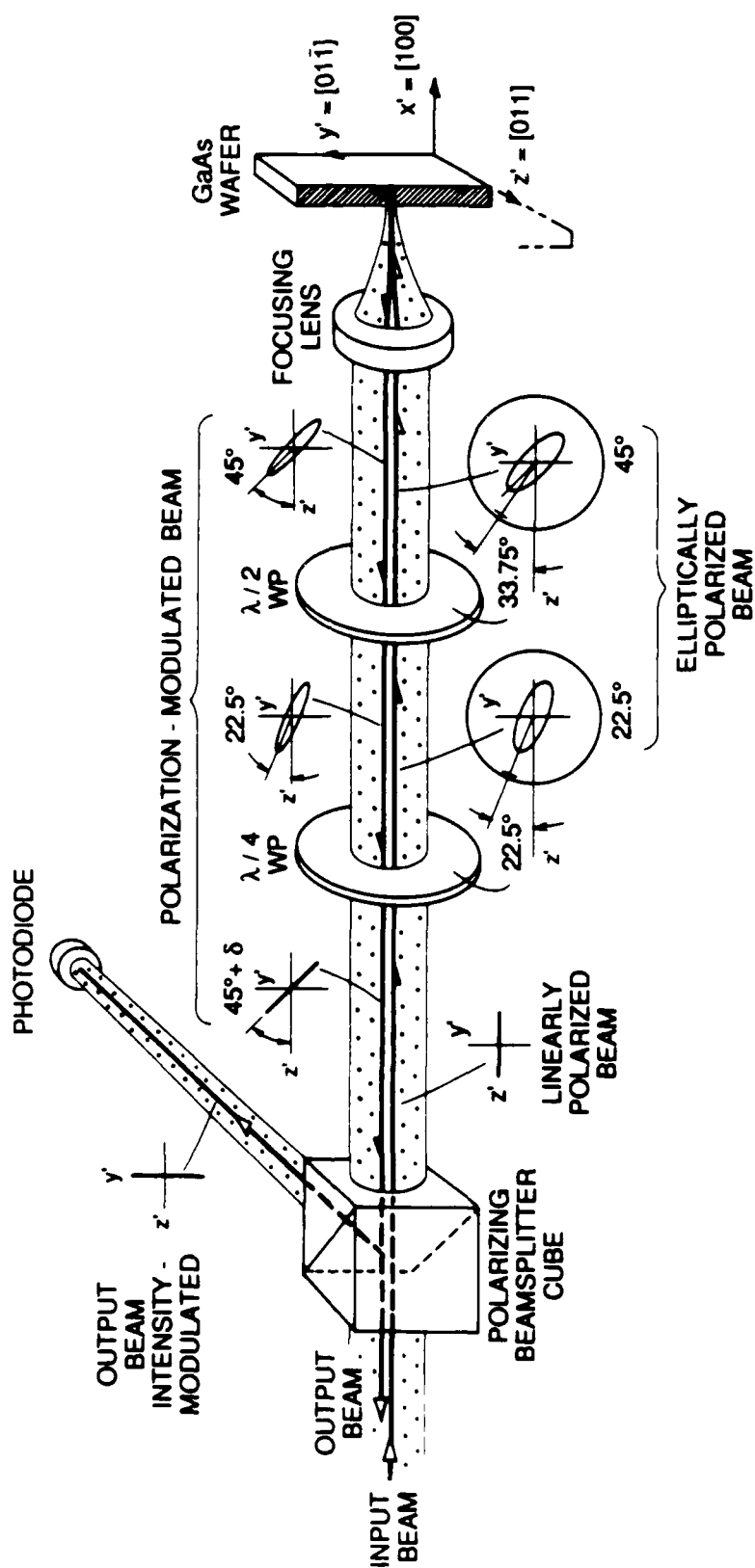


Figure 9: Coaxial arrangement for separation of incident and reflected beams in reflection-mode probing.

conductor voltage changes the polarization of the return beam through the electrooptic effect by changing the *angle* of the linearly polarized light prior to the polarizer, and thus the intensity incident upon the photodiode. The resulting intensity varies as in Eqn. 10 where V_π is now

$$V_\pi = \frac{\lambda_0}{4n_0^3 r_{41}} \cong 5 \text{ kV} \quad (11)$$

giving twice the sensitivity for the reflection-mode cases. The on-axis return beam may be separated from the incident beam with a Faraday isolator. The signal from this beam is out-of-phase with the first beam allowing for differential detection to further improve signal sensitivity.

2.3. Electrooptic Sampling

The longitudinal reflection-mode geometries provide intensity modulation proportional to voltage for IC probing. With a continuous optical probe beam, the output intensity incident upon the photodiode will be a large steady-state intensity P_0 plus a small intensity change following the voltage of the probed conductor; microwave-frequency or picosecond-risetime signals on the probed conductor will result in microwave-frequency or picosecond-risetime modulation of the probe beam. Detection of this modulation would require a photodiode/receiver system with bandwidth comparable to that of the detected signal. With commercial sampling oscilloscopes limited to ~ 14 GHz and infrared photodiodes limited to ~ 20 GHz, the probing system's bandwidth would be insufficient for many high-speed and microwave GaAs circuits. In addition, the small modulation provided by the electrooptic effect would result in extremely poor signal-to-noise ratio using direct detection at microwave bandwidths, and thus very poor instrument sensitivity.

Mode-locked laser systems in conjunction with optical pulse compressors can generate extremely short optical pulses. At visible wavelengths, pulses as short as 6 fs [31,32] have been generated, while at the infrared wavelengths where GaAs is transparent, pulses as short as 33 fs have been generated [33,34]. Sampling techniques using a pulsed optical probe can achieve a time resolution set by the optical pulse duration and the circuit-probe interaction time, permitting instrument bandwidths exceeding 100 GHz. We describe repetitive sampling in the time domain as *synchronous sampling*, where equivalent-time measurements of the voltage waveforms are made in a manner similar to the operation of a sampling oscilloscope, and in the frequency domain as *harmonic mixing*, where the electrooptic sampler measures the amplitude and phase of sinusoidal voltages on probed conductors, similar to a microwave network analyzer.

In synchronous or equivalent-time sampling, an optical probe pulse with a repetition rate f_0 (set by the laser) samples a repetitive voltage waveform. If the waveform repeats at *exactly* $N \cdot f_0$, an integer multiple of the probe repetition rate, an optical pulse interacts with the waveform every N^{th} period at a fixed point within its cycle. Over many repetitions, the pulses sample the voltage waveform at the *same* time within the cycle, undergoing an equal modulation of each pulse's intensity. The resulting change in the average intensity of the probe beam, proportional to the signal, is detected by a photodiode receiver whose bandwidth is much less than the optical pulse repetition frequency. To detect the entire time waveform, the waveform frequency is increased by a small amount Δf (Fig. 10.) The probe pulses are then slowly delayed with respect to the waveform, sampling successively delayed points, so that the average intensity at the photodiode changes in proportion to the waveform, but *repeating* at a rate Δf . The receiver then averages (low-pass filters) the photocurrent over a period much longer than $1/f_0$, eliminating the individual pulses. The averaged photocurrent i_{out} is then continuous and varies with $V(t)$, but at the slow repetition rate Δf .

$$i_{\text{out}}(t) = I_0 \left[1 + \frac{\pi}{V_{\pi}} V \left(\frac{t \Delta f}{N f_0 + \Delta f} \right) \right] \quad (12)$$

where I_0 is the average photodiode current. Typically f_0 is ≈ 82 MHz, N varies from 1 to 500 for circuit drive frequencies to 40 GHz, and Δf is 10 to 100 Hertz. In contrast to pump/probe sampling, which has one probe pulse for every pump signal, the signal repeats N times between probe pulses in equivalent-time sampling. Because the pulse repetition rate is harmonically related to the signal repetition rate, Nyquist's sampling theorem (which states maximum recoverable signal bandwidth is half the sampling rate) does not apply in terms of setting the bandwidth of this measurement. Instead, the bandwidth is determined by the sampling pulsewidth, the relative jitter between sampling pulses, and the interaction time between the pulse and the signal. These factors are discussed in detail in Section 3.2.

The frequency domain description of equivalent-time sampling is known as *harmonic mixing*. The time domain signal detected by the photodiode receiver, proportional to the product of the laser signal and the measured signal in the time domain, has a frequency spectrum determined by the spectrum of the laser *convolved* with the spectrum of the measured signal [35]. In the frequency domain

$$\mathcal{F}\{P_{\text{out}}(t)\} = \mathcal{F}\{P(t)\} * \left[\delta(f) + \frac{\pi \mathcal{F}\{V(t)\}}{V_{\pi}} \right] \quad (13)$$

where \mathcal{F} is the Fourier transform operator, $P_{\text{out}}(t)$ is the intensity out of the polarizer, $P(t)$ is the laser intensity, $\delta(f)$ is the delta function, and $*$ represents the convolution operation. Figure 11 shows a schematic representation of this convolution for a mode-locked laser spectrum and a single microwave frequency signal. Scaled replicas of the signal appear in the laser intensity spectrum as amplitude-modulation sidebands around each laser harmonic. The magnitude and phase of the signal is recovered from the baseband harmonic with a low-frequency photodiode and a synchronous detector.

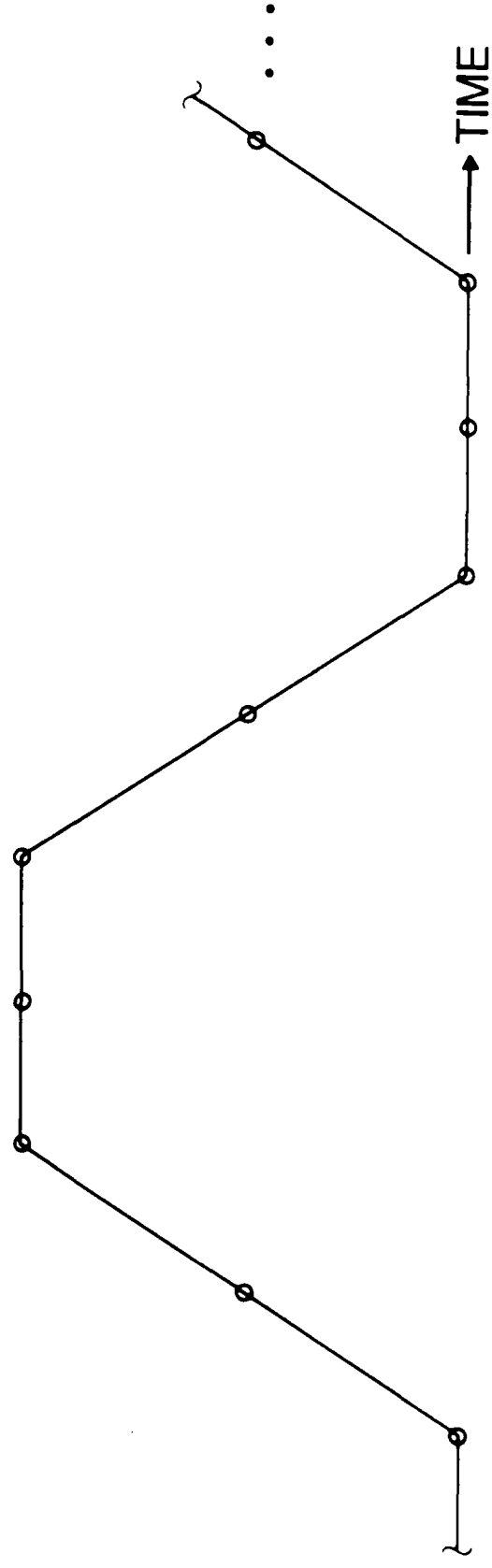
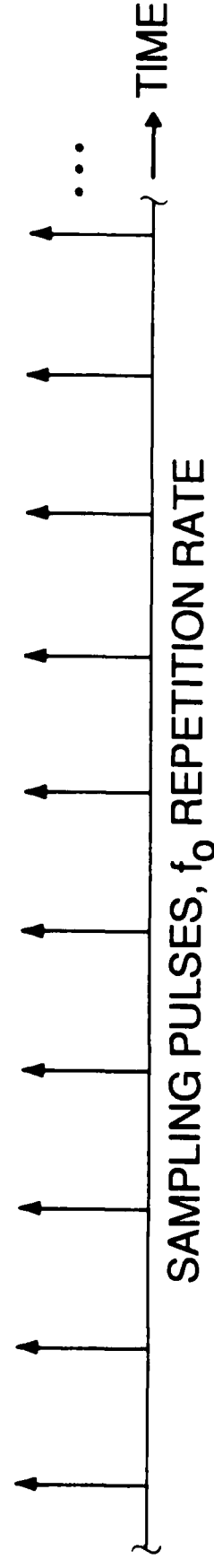
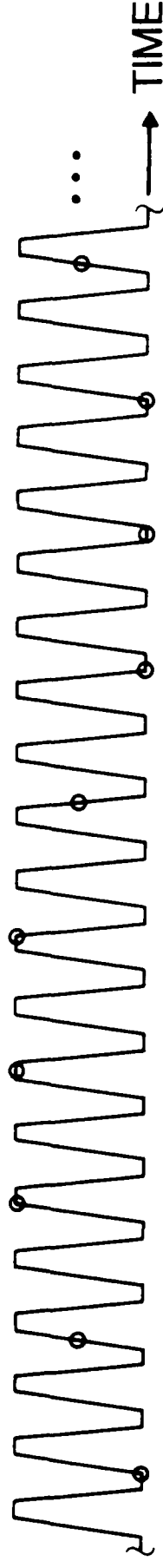
3. System performance

3.1. System description

The sampling system, shown schematically in Fig. 12, can be grouped into three sections; the laser system for optical pulse generation, the microwave instrumentation for driving the IC under test, and the receiver system for signal processing and data acquisition. The laser system consists of a mode-locked Nd:YAG laser, a fiber-grating pulse compressor, and a timing stabilizer feedback system. The Nd:YAG laser produces $1.06 \mu\text{m}$, 90 ps pulses at an 82 MHz rate with free-running pulse-to-pulse timing fluctuations of 4 ps rms, reduced to less than 300 fs rms by a phase-lock-loop feedback system [36,37] which synchronizes and stabilizes the laser pulse timing with respect to the microwave synthesizer. The fiber-grating pulse compressor shortens the pulses to 1.5 ps FWHM (full width at half maximum) [38,39,40]. The beam passes through a polarizing beamsplitter and two waveplates to adjust its polarization, then is focused through the IC substrate with a microscope objective to a $3 \mu\text{m}$ spot on the probed conductor (backside probing) or a $10 \mu\text{m}$ spot on the ground plane beneath and adjacent to the probed conductor (frontside probing.) The reflected light is analyzed by the polarizing beamsplitter and detected by a photodiode connected to a vector receiver.

To drive the IC, a microwave synthesizer generates either sinusoidal excitation for microwave circuits, or the clock/data signals for digital circuits. For wafer-level testing of IC's the drive signal is delivered with a microwave probe station

SIGNAL WAVEFORM, $N * f_0 + \Delta f$ REPETITION RATE (N=2)



SAMPLED WAVEFORM, Δf REPETITION RATE

Figure 10: Equivalent-time sampling. Typically, $f_0 = 82$ MHz, $0 \leq N < 500$, and $\Delta f \approx 10$ Hz

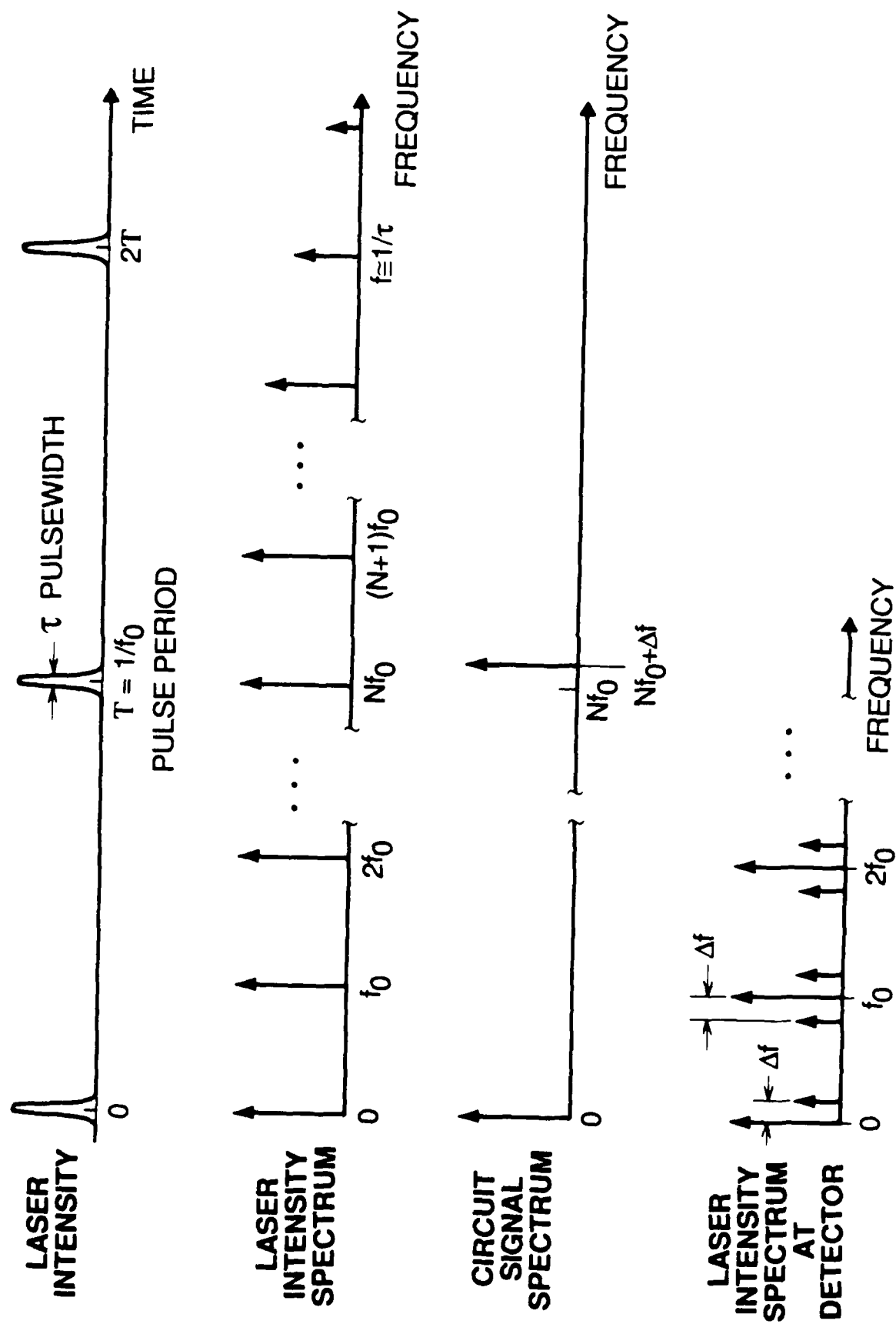


Figure 11: Electrooptic harmonic mixing.

Electrooptic Sampling System

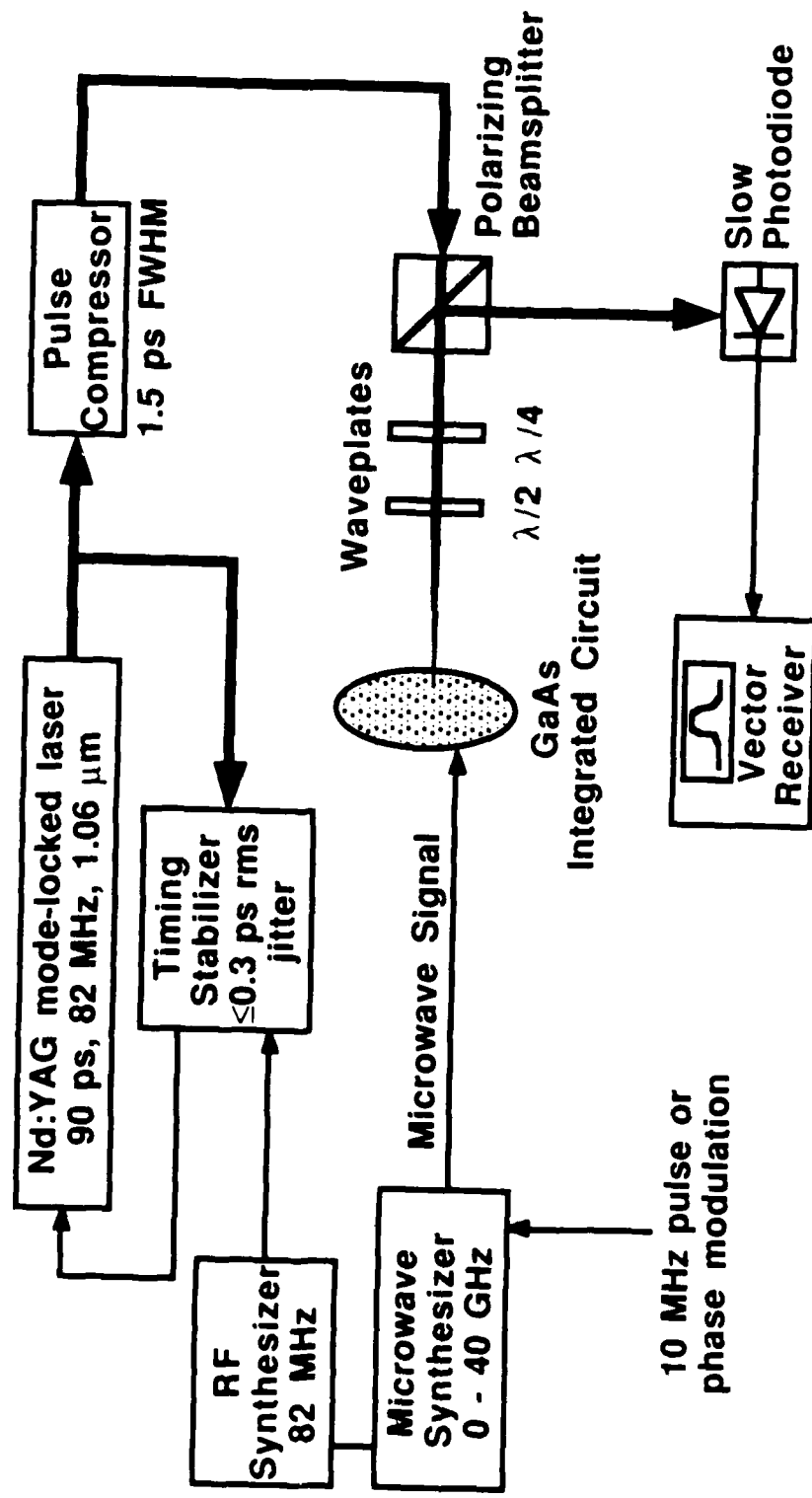


Figure 12: System for direct electrooptic sampling.

(Cascade Microtech Model 42, Figs. 13&14) modified to allow for backside electrooptic probing. The transmission line probes used with this test station allow for launching a signal on the IC with repeatable, low reflection connections in a 50 Ω environment to 40 GHz.

Signal processing is critical to achieve accurate, shot-noise limited measurements. Harmonic mixing is used for vector voltage measurements. The synthesizer is set to an exact multiple of the laser repetition rate plus a 1-10 MHz frequency offset, and the receiver is configured as a synchronous detector (i.e. an RF lock-in amplifier) to measure the magnitude and phase of the received signal at the frequency offset. Equivalent-time sampling is used to view time waveforms. The synthesizer is set to an exact multiple of the laser repetition rate (82 MHz), plus a small frequency offset Δf (1-100 Hz.) Pulse modulation, phase modulation, or fast offset/averaging signal processing as described in section 3.3 is required to suppress laser intensity noise. The resulting signal varies at the slow offset rate Δf in proportion to the detected signal.

Direct electrooptic sampling has also been demonstrated using a mode-locked or gain-switched InGaAsP injection laser to generate sampling pulses of 10-20 ps pulsewidth [41,42]. This system uses two synthesizers, referenced to a master clock, to drive the laser and to supply a signal to the IC. The longer pulsewidths of the injection laser decrease the system's time resolution compared to the 1.5 ps pulsewidths generated using the Nd:YAG/pulse compressor, but the injection laser pulses have sub-picosecond timing jitter and the laser is a very compact and stable optical source with a continuously tunable pulse repetition rate. This system has also been used to measure electrical signals in InP (indium phosphide) IC's [43].

3.2. Bandwidth

The system's bandwidth or time resolution is determined by the optical pulsewidth, the pulse-to-pulse timing jitter of the laser with respect to the microwave synthesizer driving the circuit, the interaction time of the probe pulse and the electrical signal, and the effective receiver response time. We assume Gaussian distributions for each term for simplicity. The overall time resolution is the root-mean-square sum of these values

$$\sigma_{\text{total}} = \sqrt{\sigma_{\text{PW}}^2 + \sigma_{\text{J}}^2 + \sigma_{\text{IT}}^2 + \sigma_{\text{REC}}^2} \quad (14)$$

where σ_{PW} is the rms optical pulsewidth, σ_{J} is the rms pulse-to-pulse timing jitter, σ_{IT} is the rms interaction time of the pulse through substrate, and σ_{REC}^2 is the effective receiver impulse response time.

The relation between the time resolution and the frequency bandwidth for the optical pulse is given by

$$\sigma_{\text{FWHM}} = \frac{0.312}{f_{3\text{dB}}} \quad (15)$$

where for a Gaussian pulseshape $\sigma_{\text{FWHM}} = 2.35 * \sigma_{\text{rms}}$ is the full width at half-maximum (optical pulsewidth is typically measured in terms of its FWHM, not its rms value), and $f_{3\text{dB}}$ is the half power frequency. This time-bandwidth product is reduced by a factor of $1/\sqrt{2}$ from the time-bandwidth product of 0.441 due to the square-law

photodiode detector, i.e. the optical intensity of the pulse is converted to a voltage in the receiver with a resulting power spectrum related to the square of this voltage.

The 90 ps pulsewidth from the Nd:YAG laser results in a bandwidth of 3.5 GHz, clearly not suitable for high bandwidth circuit measurements. To reduce the pulsewidth, a fiber-grating pulse compressor is used [38,39,40]. This system, based on the Kerr effect or self-phase modulation in a single-mode optical fiber, generates a frequency chirp on the laser pulse as it propagates through the fiber. The light emerging from the fiber is red-shifted on its leading edge and blue-shifted on its trailing edge with the frequency varying across the pulse duration in proportion to the *derivative* of the intensity envelope. For a Gaussian intensity pulseshape (characteristic of mode-locked lasers) the frequency chirp is nearly linear over the center of the pulse. These new frequency components are recombined into a compressed pulse by passing the light through a grating pair, where the time-of-flight delay is linearly proportional to the light's wavelength, thus acting as a dispersive delay line where the red-shifted leading frequency components are delayed with respect to the blue-shifted trailing frequencies. The wavelength-dependent delay is adjusted by the separation of the gratings to match the frequency chirp of the light, producing a compressed pulse.

A number of effects limit the amount of pulse compression available with this technique; stimulated Raman scattering limits the maximum optical power focused into the fiber core, and deviation from a linear frequency chirp on the pulse due to non-ideal input pulseshapes can generate long pedestals on an otherwise short compressed pulse. Using a fiber length of 1 km in the pulse compressor, the group velocity dispersion enhances the region of linear frequency chirp [39], and the pulses from the mode-locked Nd:YAG laser are routinely compressed to 1.5 ps, a factor of 60:1. Using two-stage optical compression, pulses as short as 200 fs at 1.06 μm have been generated [34].

The compressed pulsewidth, as measured with an optical autocorrelator, deviates from the autocorrelation of an ideal Gaussian pulseshape as evidenced by slight "wings" or pedestals on the pulse due to the non-ideal frequency chirp of input pulse (Fig. 15). The group velocity dispersion of the relatively long 1 km fiber reduces the pulse pedestals compared to shorter fiber lengths [39]. A Gaussian pulse of 1.4 ps FWHM duration has spectral content extending past 200 GHz, while the spectral content of the compressed pulse deviates from an ideal Gaussian pulse, where the power spectral density is determined by numerically Fourier transforming the autocorrelation (Fig. 16) [35]. The wings on the compressed pulse may be further reduced by "spectral windowing" [44] to remove part of the nonlinear frequency chirp or polarization discrimination of the compressed pulse [45].

Timing jitter influences both bandwidth and sensitivity; the impulse response of the sampling system is the convolution of the optical pulseshape with the probability distribution of its arrival time (neglecting optical transit time), while those Fourier components of the jitter lying within the detection bandwidth of the receiver introduce noise proportional to the time derivative of the measured waveform (section 3.3). Stabilization of the laser timing is thus imperative for low-noise measurements of microwave or picosecond signals. The timing fluctuations of the laser are suppressed by phase-locking the laser to a high-stability reference oscillator [36,37]. Figure 17 shows the block diagram of the feedback system. A photodiode monitors the 82 MHz laser pulse train, and the phase of its fundamental component is compared with that of the reference oscillator, generating a phase error signal. The 41 MHz signal required for driving the laser's acousto-optic (A-O) cell is generated by frequency division from the 82 MHz standard; its timing (phase) is adjusted with a voltage-controlled phase-shifter controlled by the amplified and frequency-compensated phase error signal. Given an error-free phase detector, the laser timing fluctuations are suppressed in proportion to the loop gain of the feedback system. Figure 18 shows the measured phase noise of one harmonic of the laser with an HP 8662 low-phase noise synthesizer as the reference for the feedback system. From this measurement the time jitter is calculated (see section 3.3, equation 26) to be less than 300 fs rms.



Figure 13: Cascade [6] microwave wafer probe station modified for electrooptic sampling.
a) Wafer, wafer stage, microwave wafer probes, and viewing objective.

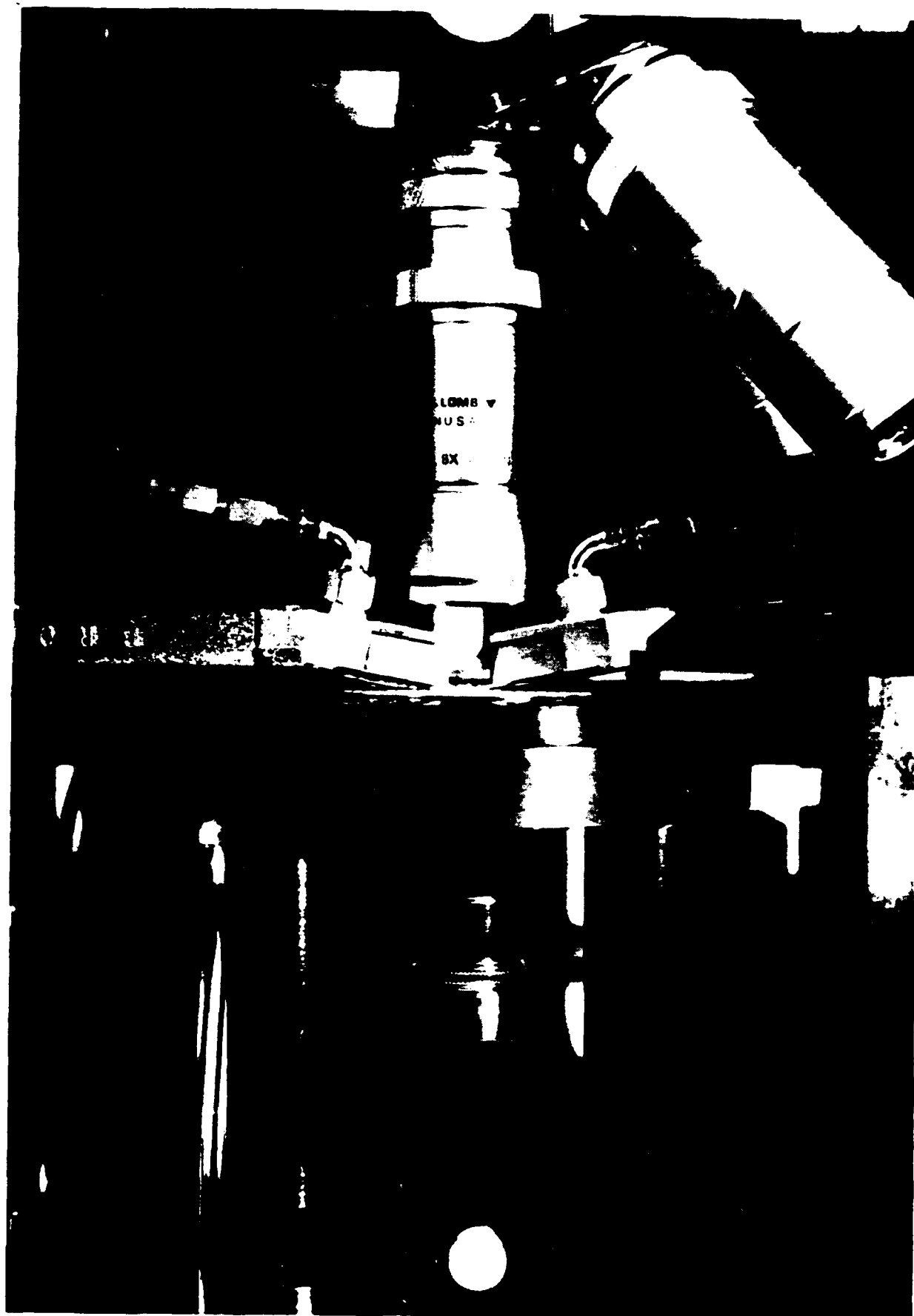


Figure 13: Cascade [6] microwave wafer probe station modified for electrooptic sampling.
b) View showing probe beam focusing objective below the wafer stage.
The probe beam is focused on the IC through a hole or a sapphire window in the wafer stage.

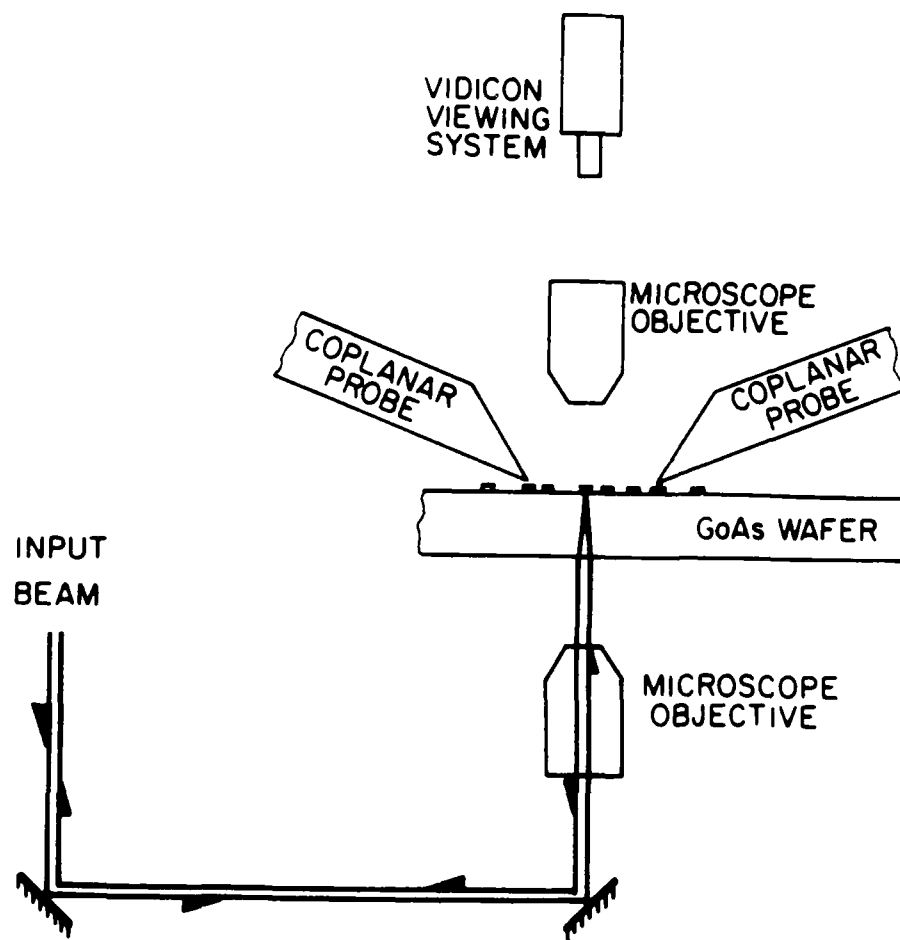


Figure 14: Schematic diagram of the beam path through the Cascade probe station.

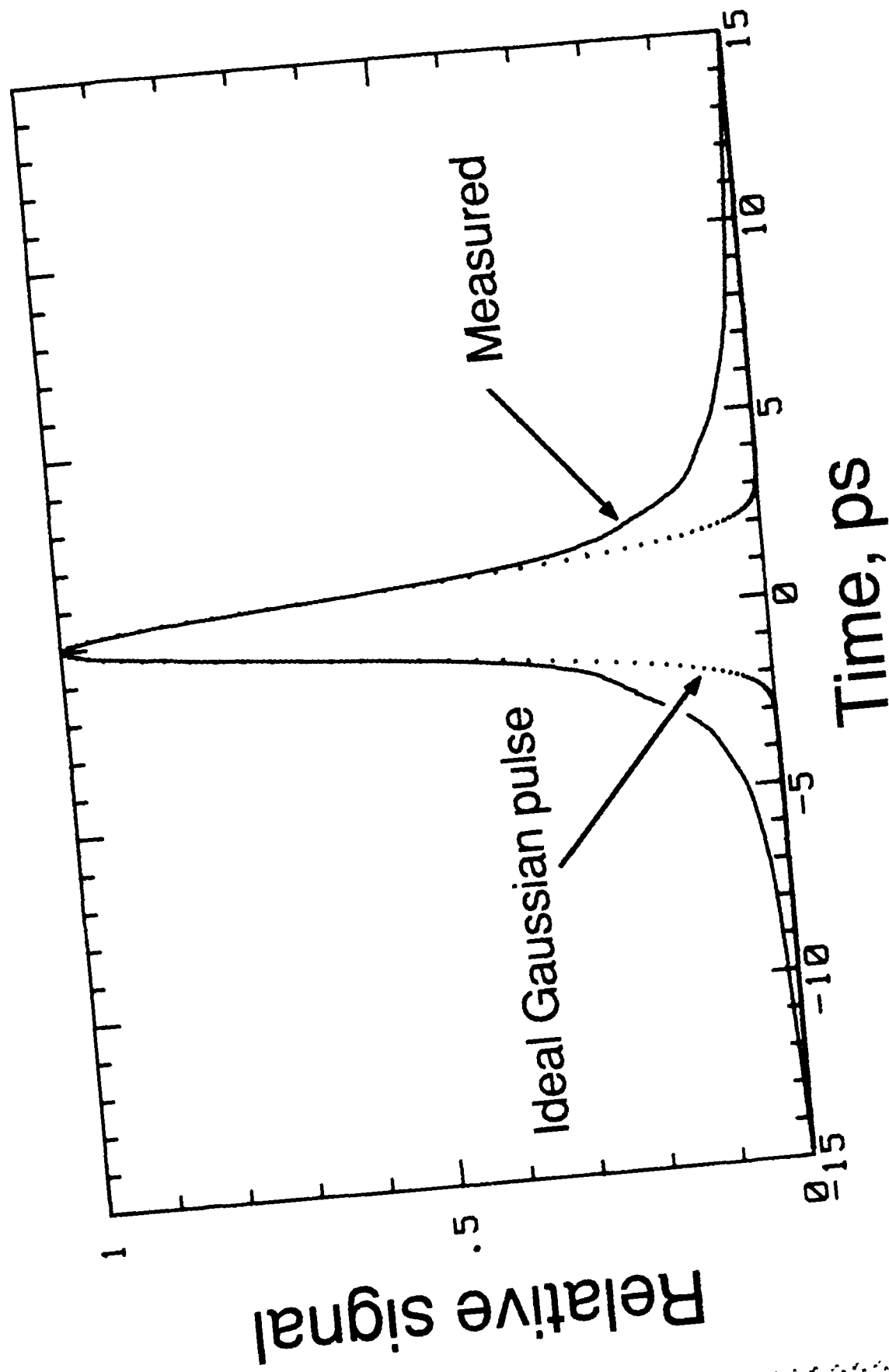


Figure 15: Autocorrelation of the 1.4 ps FWHM compressed pulse (solid line) and the autocorrelation of an ideal Gaussian pulse (dashed line.)

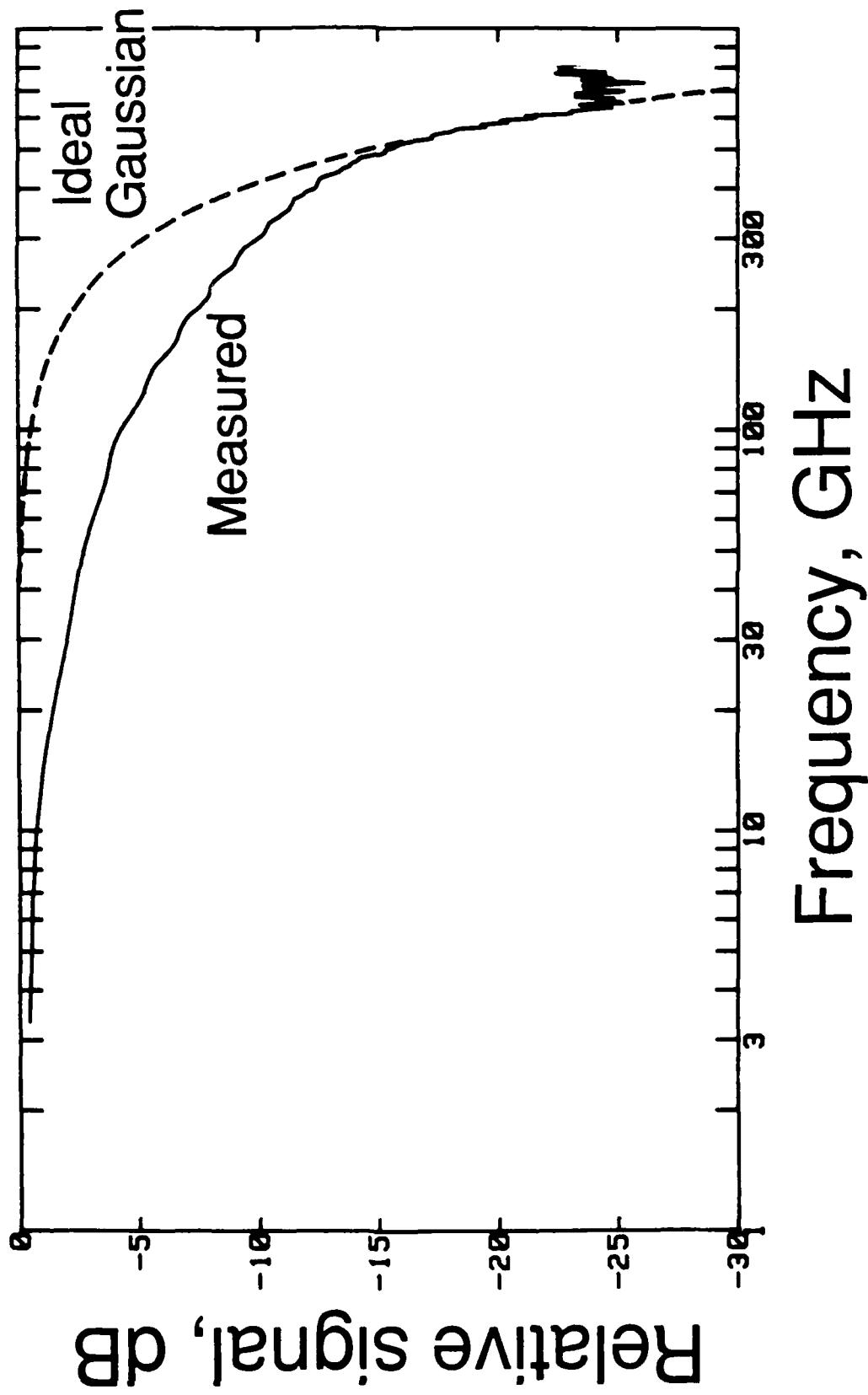


Figure 16: Power spectral density of the compressed pulse (solid line) and an Gaussian pulse (dashed line). The power spectral density is the Fourier transform of the autocorrelation.

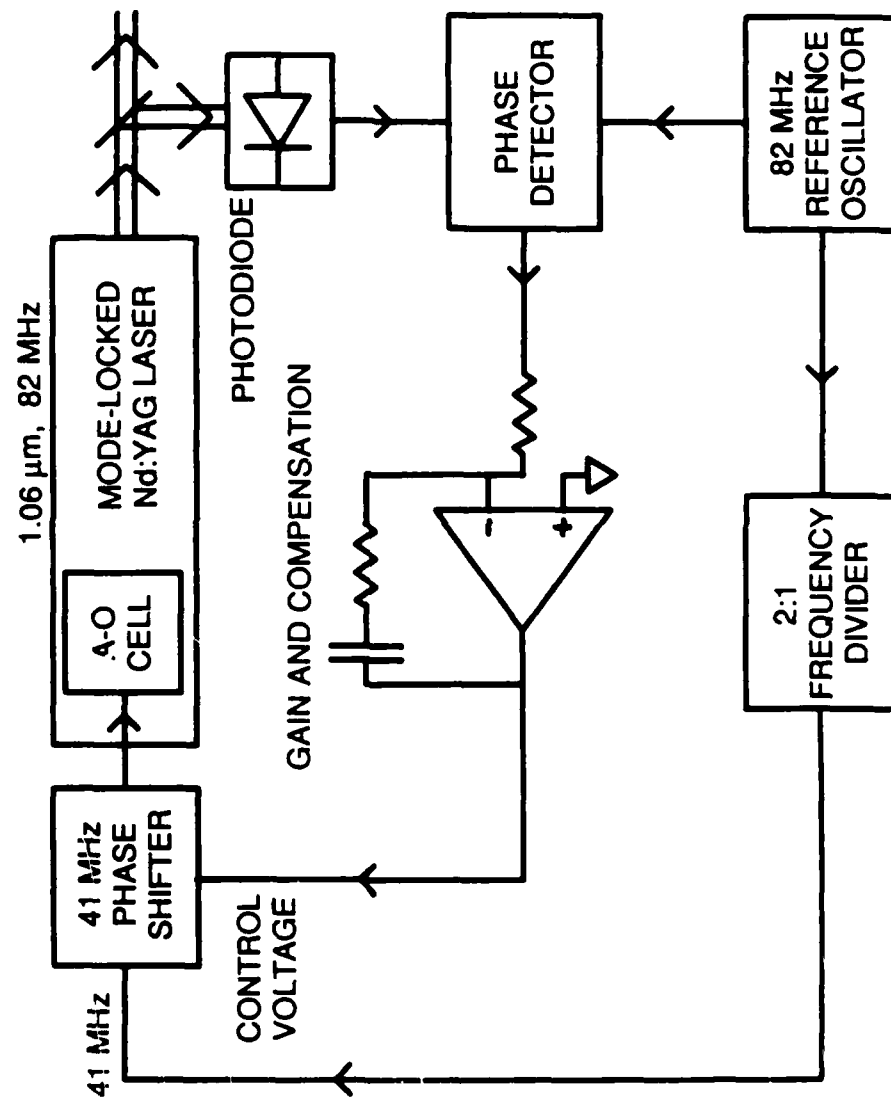


Figure 17: Block diagram of the phase-lock-loop timing stabilizer feedback system.

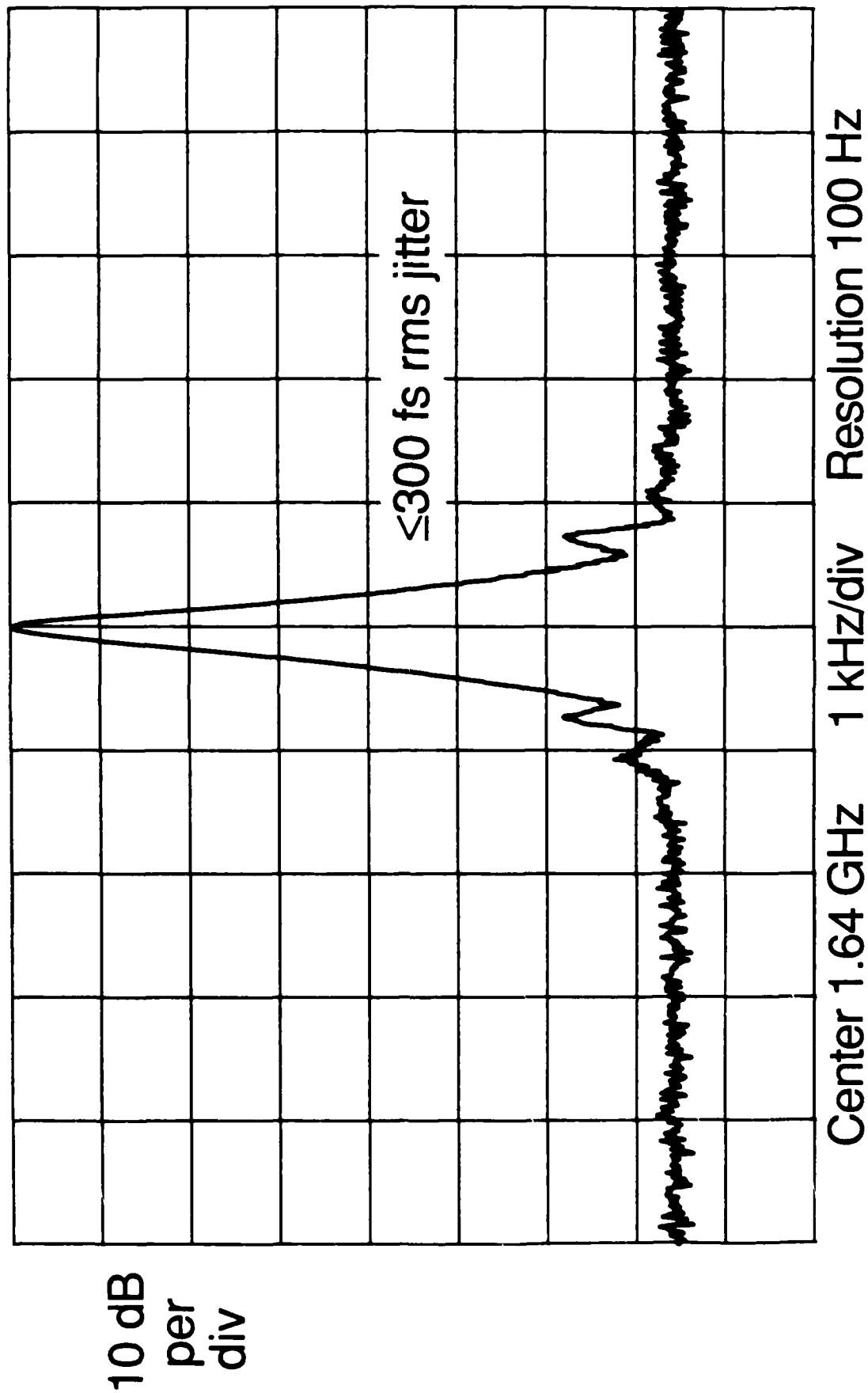


Figure 18: Laser phase noise at the 20th harmonic of the pulse repetition rate, measured with a photodiode and a spectrum analyzer. The noise floor of this measurement is instrumentation limited, giving an upper limit for the timing jitter of 300 fs rms.

The interaction time of the optical pulse and electrical signal in the GaAs substrate comes from several factors; the response time of the electrooptic effect, the electrical transit time, and the optical transit time. The electrooptic effect in GaAs arises primarily from its electronic polarizability and is intrinsically very fast (see Auston, this issue), with a response time on the order of 10 femtoseconds. The electrical transit time is the propagation time of the electrical signal as it traverses the spatial extent of the probe beam. For typical IC values this time is on the order of 60 fs [27]. The optical transit time is the propagation time of the optical pulse as it traverses the electric fields within the GaAs substrate. For frontside probing of microstrip lines, where the field is uniform though the substrate, the optical transit time is proportional to the substrate thickness. For backside probing of coplanar transmission lines or planar interconnections, the electric field is not uniform in the substrate and the characteristic depth of the electric fields is on the order of the conductor spacing; in this case the optical transit time is not a function of substrate thickness, but is proportional to the conductor spacing. Because the optical and microwave dielectric constants in GaAs are nearly equal, microwave transmission lines have a cutoff frequency for higher-order modes roughly equal the inverse of the optical transit time. Well-designed microwave circuits operate at frequencies well below the multimode cutoff frequency. Only when measuring interconnects near or above the cutoff frequency (where dispersive characteristics are of interest) must the optical transit time be considered. For example, the optical transit time for a 125 μm thick substrate, typical of MMIC's operating at frequencies below 40 GHz, is 3 ps, corresponding to a 3 dB response rolloff of >100 GHz.

The effective receiver impulse risetime arises from the constraint put on the receiver bandwidth by the required system sensitivity. We assume for analysis the receiver has a Gaussian impulse response

$$h(t) = \frac{1}{\sqrt{2\pi}\sigma_t} \exp\left(-\frac{t^2}{2\sigma_t^2}\right) \quad (16)$$

where σ_t is the rms duration. Then, the receiver frequency response

$$H(f) = \exp\left(-\frac{f^2}{2B_{\text{acq}}^2}\right) \quad (17)$$

has an rms signal acquisition bandwidth $B_{\text{acq}} = 1/2\pi\sigma_t$. Because the sampled signal at frequency Nf_0 is translated to a lower frequency Δf at the receiver (Eqn. 12), the effective receiver impulse response for synchronous sampling is

$$\sigma_{\text{REC}} = \frac{\Delta f}{Nf_0} \sigma_t = \frac{\Delta f}{Nf_0 2\pi B_{\text{acq}}} \quad (18)$$

Given a required time resolution σ_{total} from the electrooptic sampling system, the scan rate Δf of the sampler must then be limited. With fixed time resolution, larger receiver bandwidths B_{acq} permit faster waveform scan rates, but degrade the measurement sensitivity.

3.3. Sensitivity

If the measurement bandwidth provided by the electrooptic sampler is to be useful, the instrument must also provide sufficient sensitivity to observe signal voltages typical of high-speed GaAs circuits. As in any system, sensitivity is determined by the signal to noise ratio; the instrument's sensitivity, or minimum detectable voltage, is the probed voltage which results in a measured signal equal to the measurement system's noise signal. Most noise sources have power spectral densities which are independent of frequency ("white" noise), resulting in a noise voltage proportional to the square root of the signal acquisition bandwidth B_{acq} and a minimum detectable voltage expressed in units of volts per root Hertz ($V/\sqrt{\text{Hz}}$). Smaller minimum detectable voltages permit more rapid measurement acquisition for fixed measurement accuracy. With appropriate system design and signal processing, the various sources of noise in the electrooptic sampler can be reduced or eliminated, permitting low-noise voltage measurements with fast data acquisition.

The fundamental limiting noise source in electrooptic sampling is the shot noise of the probe beam (observed as shot noise of the photodiode quiescent current.) The signal generated by the photodiode (dropping the constant term I_0) from Eqn. 12 is

$$i_{out}(t) = \frac{I_0 \pi}{V_\pi} V \left(\frac{t \Delta f}{N f_0 + \Delta f} \right) + i_{SN} \quad (20)$$

The shot noise, i_{SN} , associated with the DC component of the photodiode current has a variance given by

$$\overline{i_{SN}^2} = 2qI_0 B_{eq} \quad (21)$$

where q is the electron charge, the horizontal bar denotes the statistical expectation, and

$$B_{eq} = \sqrt{\pi/2} B_{acq} \quad (22)$$

is the receiver's equivalent noise bandwidth. Setting the signal current $I_0 \pi V_{min} / V_\pi$ equal to the shot noise current, and normalizing to $B_{eq} = 1$ Hz acquisition bandwidth, the minimum detectable voltage is

$$V_{min} = \frac{V_\pi}{\pi} \sqrt{\frac{2q}{I_0}} \quad \frac{\text{Volts}}{\sqrt{\text{Hz}}} \quad (23)$$

For the reflection-mode probing geometries, $V_\pi \approx 5$ kV, while the average photocurrent I_0 is typically 1 mA. Then, the minimum detectable voltage is

$$V_{min} \approx 30 \mu\text{V}/\sqrt{\text{Hz}} \quad (24)$$

Typically, $V_{min} \approx 70 \mu\text{V}/\sqrt{\text{Hz}}$ is observed experimentally due to ≈ 10 dB of residual noise from the system (dominated by excess amplitude noise from the pulse compressor); this sensitivity is sufficient to acquire measurements at scan rates of 10-100 Hz with a noise floor of a few millivolts. The actual measurement system has a number of additional excess noise sources to contend with to achieve $70 \mu\text{V}/\sqrt{\text{Hz}}$ sensitivity. These include timing jitter of the laser (phase noise), intensity noise of the probe beam from low frequency laser fluctuations and from the pulse compressor, and receiver noise.

Low-frequency fluctuations in the mode-locked laser introduce noise into the received photocurrent. Fluctuations in the mode-locked Nd:YAG laser include variations in both pulse intensity and pulse timing. The laser produces a train of pulses approximated by

$$P(t) = \frac{P_0}{f_0} [1 + N(t)] \sum_{m=-\infty}^{+\infty} \delta[t - m/f_0 - J(t)] \quad (25)$$

where $N(t)$ is the normalized pulse intensity fluctuation and $J(t)$ is the pulse timing fluctuation. The laser intensity then has a power spectral density $S_P(f)$ approximated to second order in $mf_0\sigma_J$ by

$$S_P(f) \approx P_0^2 \sum_{m=-\infty}^{+\infty} \left\{ \left[1 - (2\pi m f_0 \sigma_J)^2 \right] \delta(f - m f_0) + \left[1 - (2\pi m f_0 \sigma_J)^2 \right] S_N(f - m f_0) + (2\pi m f_0)^2 S_J(f - m f_0) \right\} \quad (26)$$

where $S_N(f)$ is the power spectral density of $N(t)$ and $S_J(f)$ is the power spectral density of $J(t)$. The spectrum of the laser intensity is a series of discrete spectral lines at multiples of f_0 , plus spectra resulting from the timing and amplitude fluctuations, referred to as amplitude-noise sidebands [$S_N(f - m f_0)$] and phase-noise sidebands [$(2\pi m f_0)^2 S_J(f - m f_0)$]. By monitoring the laser intensity with a spectrum analyzer and measuring the relative powers of the laser harmonic and its noise sidebands as a function of the order of the harmonic, the spectral densities of $N(t)$ and $J(t)$ are measured.

With these amplitude and timing fluctuations, the received photocurrent $i_{out}(t)$ is

$$i_{out}(t) = I_0 + \frac{I_0 \pi}{V_\pi} V \left(\frac{t \Delta f}{N f_0 + \Delta f} \right) + i_{laser,0} + i_{laser,1} + i_{phase} \quad (27)$$

where

$$i_{laser,0} = I_0 N(t) \quad (28)$$

is the zero-order (background) received noise current due to laser intensity fluctuations,

$$i_{laser,1} = N(t) \frac{I_0 \pi}{V_\pi} V \left(\frac{t \Delta f}{N f_0 + \Delta f} \right) \quad (29)$$

is a received noise current arising from the product of the laser intensity fluctuations and the signal voltage, and

$$i_{phase} = \frac{I_0 \pi}{V_\pi} J(t) V \left(\frac{t \Delta f}{N f_0 + \Delta f} \right) \quad (30)$$

is the noise arising from the laser timing fluctuations, where $V'(t)$ is the time derivative of $V(t)$. We have assumed that $\Delta f \ll Nf_0$, and have omitted terms in $N(t)J(t)$, as these are negligible.

The spectral density $S_N(f)$ of the laser intensity noise $N(t)$ is shown in Fig. 19. At frequencies below ≈ 1 kHz, the laser intensity noise is approximately 70 dB greater than the shot noise of a 0.5 mA receiver photocurrent. At higher frequencies the noise power decreases, reaching an asymptote 5-15 dB above the shot noise level at frequencies greater than ≈ 100 kHz. The excess noise at frequencies above 100 kHz arises from Raman scattering and polarization noise in the optical pulse compressor. If the sampled signal were detected at a low frequency, the zero-order laser intensity noise $i_{\text{laser},0}$ would contribute a $10^3:1$ degradation to the minimum detectable voltage. To suppress the zero-order laser intensity noise, the excitation to the circuit under test is modified so that the received photocurrent $i_{\text{out}}(t)$ has a spectral component, with amplitude proportional to the probed voltage, at a frequency above the 100 kHz $1/f$ noise corner frequency. One method is pulse modulation (chopping) of the drive signal. The received photocurrent then has a spectral component at the chopping rate whose amplitude varies in proportion to the sampled point on the signal waveform. The chopping frequency is set from 1-10 MHz, well above the $1/f$ noise corner frequency, to achieve near-shot-noise limited detection.

Driving digital IC's requires modification of the pulse modulation scheme, since most digital circuits require *continuous* drive signals for their clocks. One alternative is phase modulation of the drive signal, corresponding to controlled jitter in time, at the chopping frequency. The received photocurrent then has a component at the chopping frequency whose amplitude is proportional to the time derivative of the sampled signal, and is recovered by integration [46]. The drawbacks to this technique are circuit sensitivity to clock jitter (usually negligible) and a reduction in the signal-to-noise ratio (due to the differentiation) by a factor of the square root of the acquisition bandwidth. A second signal recovery scheme, termed fast offset and averaging, relies on increasing the frequency offset Δf to a rate above the low-frequency laser noise, 100 to 200 KHz. The signal is recovered by high-pass filtering to remove the low-frequency laser noise, then by signal averaging at the offset rate Δf . If the received signal is averaged at the scan rate, the sensitivity using fast averaging is the same as for simple synchronous sampling with the same measurement acquisition time. Commercial digitizing oscilloscopes have limited averaging rates; at scan rates of 100-200 kHz, most instruments can average a maximum of only 100-200 scans per second, corresponding to a signal-to-noise reduction of 30 dB from averaging at the fast scan rate. Even so, we have demonstrated the feasibility of this technique using a commercial digitizing oscilloscope, and the signal-to-noise reduction, compensated for by increased measurement acquisition time, is justified for testing IC's that are sensitive to signal chopping.

The two remaining noise terms arising from laser low-frequency fluctuations, $i_{\text{laser},1}$ and i_{phase} , are not suppressed by signal chopping or signal phase modulation. Because these noise terms arise from the products $N(t)V(\alpha t)$ and $J(t)V'(t)$, their power spectra are proportional to the convolutions $S_N(f) * S_V(f/\alpha)$ and $S_J(f) * f^2 S_V(f/\alpha)/\alpha^2$, respectively, where $S_V(f)$ is the power spectrum of $V(t)$. Pulse-modulation or phase-modulation of $V(t)$ at a frequency f_{mod} results in a received photocurrent having spectral components at f_{mod} arising from both $V(t)$ and from the multiplicative laser amplitude noise $i_{\text{laser},1}$ and the received phase noise i_{phase} . Instead, these noise terms must be suppressed by laser stabilization. The laser timing stabilizer reduces $S_J(f)$ by 20-25 dB at frequencies lying within typical receiver bandwidths B_{acq} of 10 Hz-1 kHz. Fig 20 shows the resulting suppression of received phase noise on a 20 GHz sampled signal. The multiplicative amplitude noise $i_{\text{laser},1}$ can be suppressed by feedback stabilization of the laser intensity [47]. As the multiplicative amplitude noise scales with the signal voltage $V(t)$, without laser amplitude stabilization it is a significant source of measurement error in the electrooptic sampling system for signal voltages larger than ≈ 1 V.

Additional noise arises from the receiver, which has an equivalent input noise current

Low-frequency Laser Intensity Noise Spectrum

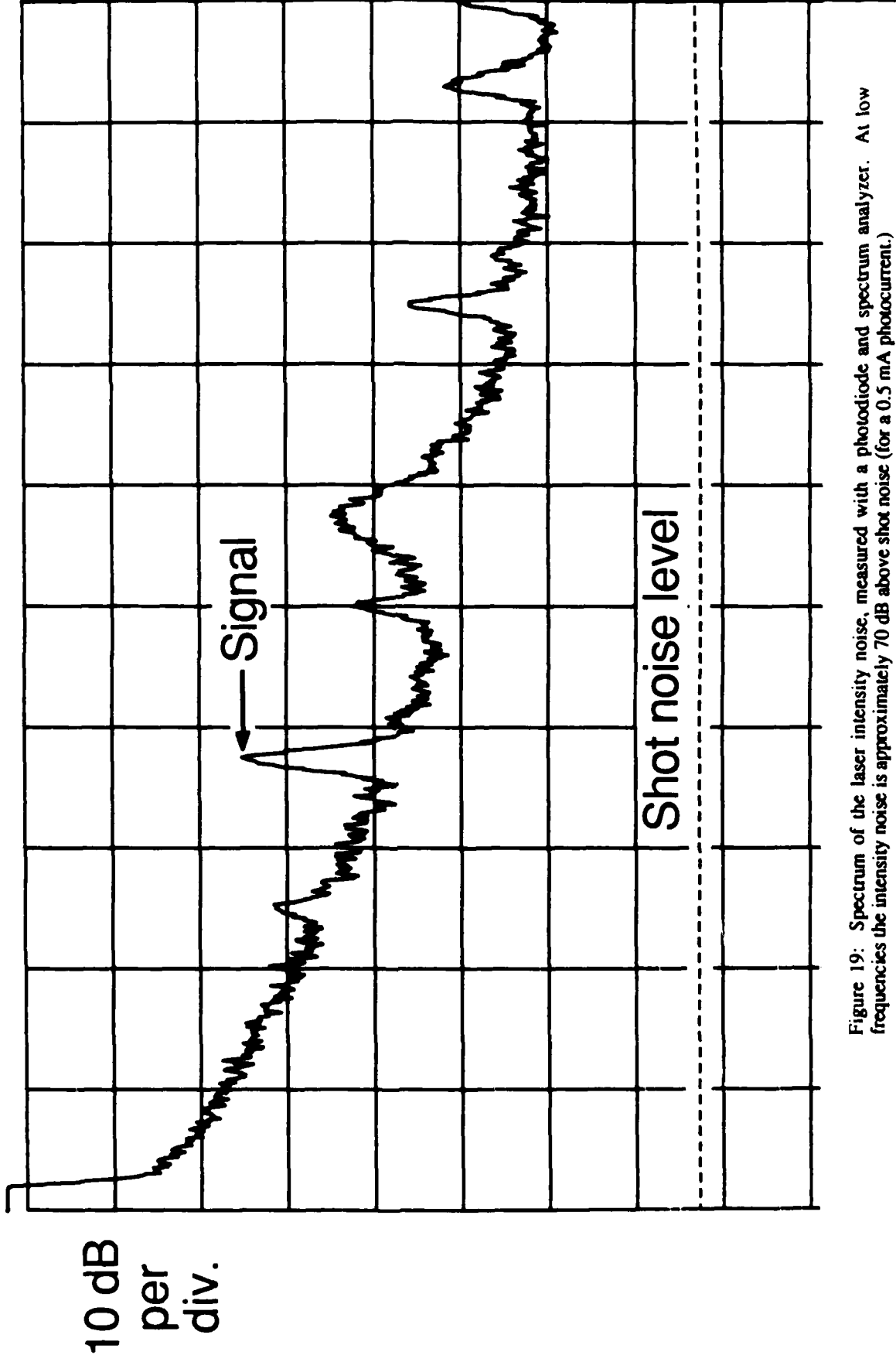


Figure 19: Spectrum of the laser intensity noise, measured with a photodiode and spectrum analyzer. At low frequencies the intensity noise is approximately 70 dB above shot noise (for a 0.5 mA photocurrent.)

Start 0 KHz 10 kHz/div Resolution 1 KHz Stop 100 KHz

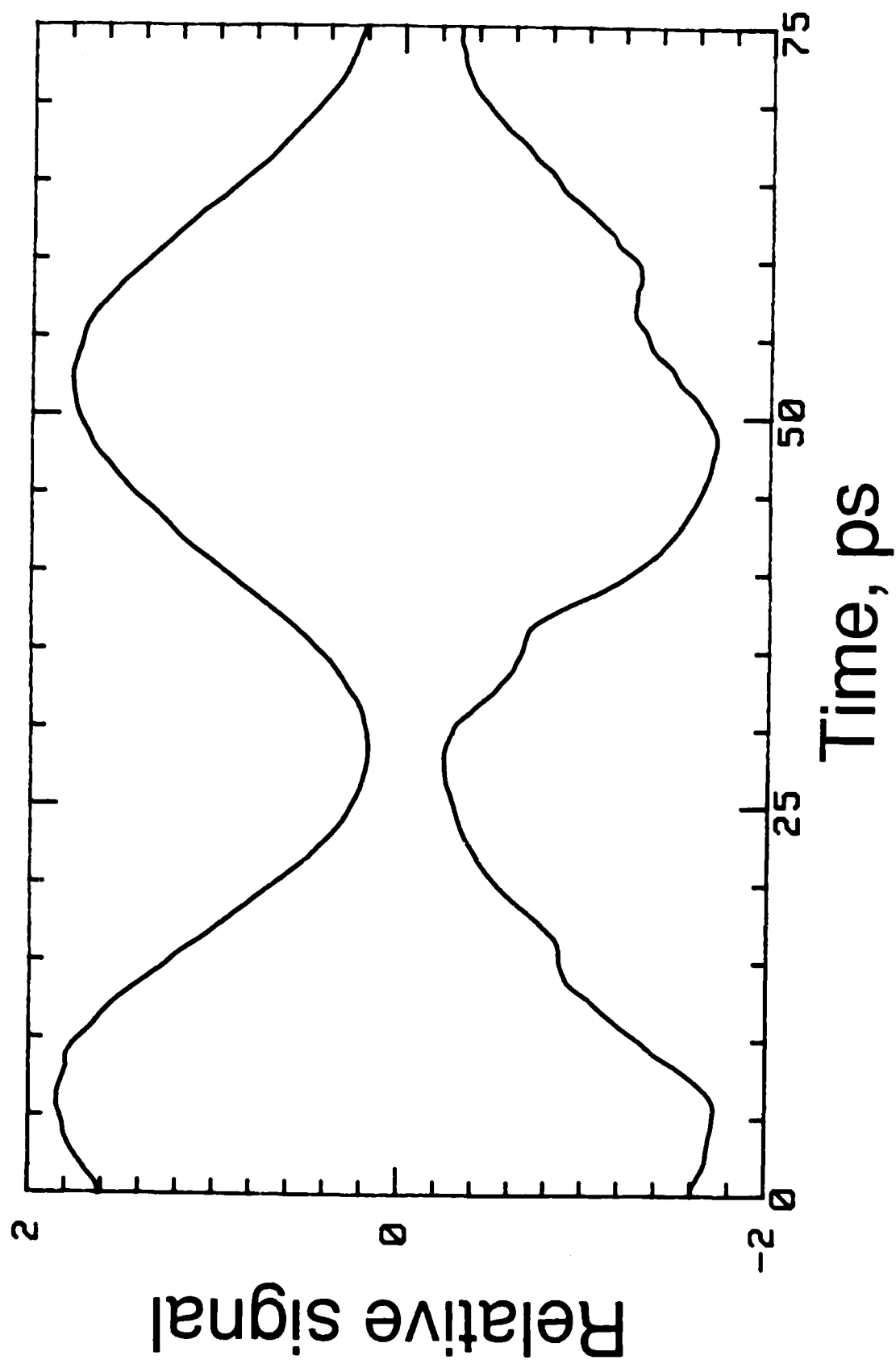


Figure 20: 20 GHz sampled signal with (upper trace) and without (lower trace) timing stabilizer.

$$\overline{i_{\text{receiver}}^2} = \frac{4kTB_{\text{eq}}}{R_L} + \overline{i_{\text{amp}}^2} + \frac{1}{R_L^2} \overline{v_{\text{amp}}^2} \quad (31)$$

where k is Boltzmann's constant, T is the absolute temperature, and R_L is the photodiode load resistor. The first term is the Johnson or thermal noise of the load resistor, and $\overline{i_{\text{amp}}^2}$ and $\overline{v_{\text{amp}}^2}$ are the equivalent input noise current and equivalent input noise voltage of the amplifier following the photodiode. Receiver noise is reduced to a level below the shot noise limit by appropriate receiver design; R_L is made large in comparison with $2kT/qI_0$ so that Johnson noise is well below shot noise and the photodiode amplifier is selected for low input noise.

The pulse compressor introduces excess amplitude noise due to stimulated Raman scattering (SRS) and temperature-induced polarization drift in the non-polarization-preserving fiber [48]. We observe the broadband background amplitude noise increase dramatically (20-40 dB) above the shot noise limit as the input power to the fiber approaches the Raman threshold. A periodic structure to the noise spectrum (Fig. 21) corresponds to the free spectral range of the 1 km fiber. We attribute this effect to a parasitic synchronously pumped fiber-Raman laser formed by the 4% Fresnel reflection at each fiber end facet and the high gain of the 1.06 μm pumped SRS [49,50]. Self-phase modulation (SPM) occurs over the entire length of the fiber while the interaction length for SRS is set by the dispersion-induced walkoff between the input and Stokes-shifted wavelengths, approximately 60 meters. This dispersion also causes the 1.06 μm pump and the 1.12 μm Raman pulse to separate by 1.8 ns over the length of the 1 km fiber. If the weakly reflected Raman pulse is synchronized to within 1.8 ns of a pump pulse it is further amplified after its first round trip through the fiber. With this condition the Raman threshold with the 1 km fiber is 400 mW average power from the fiber output. Trimming the fiber length a few inches defeats this synchronism and increases the Raman threshold to 700 mW. We routinely obtain 60X compression ratios at power levels (350 mW average power from the fiber output) well below the Raman threshold.

In addition to SRS the fiber generates broadband polarization noise, possibly arising from guided acoustic wave Brillouin scattering [51] or intensity-induced polarization fluctuations [45]. The polarization noise is converted to amplitude noise after passing through the grating pair in the compressor. Adjusting the polarization from the fiber to maximize transmission through the grating path results in second-order intensity variations due to polarization fluctuations, reducing this excess noise to a level approaching the shot noise limit (Fig. 22). However, the pulse compressor with the relatively long 1 km fiber typically contributes 5 to 15 dB of excess amplitude noise. To suppress polarization drift, the non-polarization-preserving fiber is placed in a temperature-stabilized environment.

3.4. Spatial resolution

The spatial resolution of the probe is set by diffraction-limited focusing of the 1.06 μm wavelength beam. The minimum achievable spot diameter (full-width half maximum) for diffraction limited optics is

$$d_0 \equiv \frac{\lambda \sqrt{1-NA^2}}{2NA} \quad (32)$$

where λ is the optical wavelength and NA is the numerical aperture of the focusing lens. With a high NA lens spot sizes approaching the optical wavelength are possible. Standard microscope objectives (focal length of 8 mm and NA of 0.4, for example) routinely achieve spot sizes of 3 μm , suitable for probing most IC interconnects but not for probing very small features such as sub-micron gate lines.

3.5. Linearity

Because typical circuit voltages are small compared to the half-wave voltage V_{π} , the probe beam intensity modulation is small and very nearly linear with respect to the probed voltage. An analysis of the linearity and dynamic range of the probe due to the sinusoidal dependence of the probe intensity with respect to signal voltage [27] shows the probe is linear to within 1% for signal voltages ≤ 200 volts with the system set at the quarter-wave bias (the linear region of the sinusoidal transmission) as in Eqn. 8.

3.6. Invasiveness

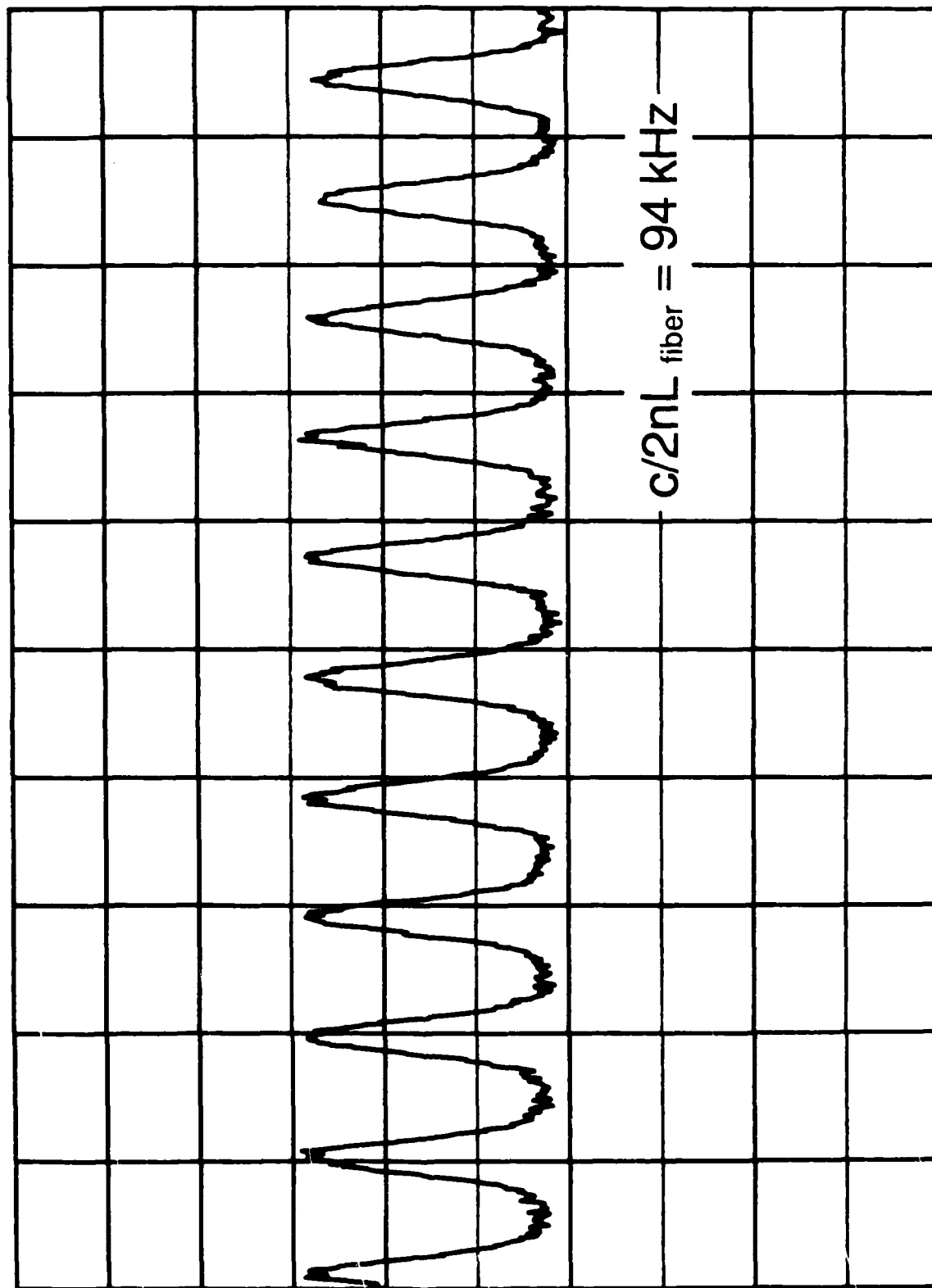
One important feature of optical probing of IC's is the non-contact, non-destructive nature of the technique. Compared to conventional electrical probes, the optical probe makes no mechanical contact to the IC, avoiding physical damage to the circuit, does not require the test point to drive a 50 Ω load impedance, and has no parasitic impedances. The lack of parasitic impedances is an important characteristic for measurement frequencies in the upper microwave and millimeter-wave region, where even the small parasitic impedances of well-designed electrical probes become significant. The optical probe can perturb the circuit either by photoconductively generating carriers, which then change the substrate conductivity and generate photorefractive or photovoltaic potentials, or by the inverse electrooptic effect or optical rectification. Direct band-to-band absorption of the probe is avoided because the photon energy of the 1.06 μm optical probe, 1.17 eV, is well below the bandgap energy, 1.42 eV, of GaAs. However, the presence of impurities in the GaAs results in deep levels, i.e. the presence of allowed electron states at energies near mid-bandgap. The deep levels, primarily the EL2 level, absorb some of the 1.06 μm light in the GaAs and generate free carriers. Absorption can also occur if the probe beam is too intense. With tight beam focusing and short pulse duration, probe beams of average intensities approaching 100 mW have peak pulse intensities sufficient for two-photon band-to-band absorption.

On circuits, we observe changes of approximately 0.1 dB in the forward gain (S_{21}) of microwave distributed amplifiers with an intense 125 mW probe beam at 1.06 μm wavelength. Focusing *directly* within the active FET channel causes significant changes in drain current. However, the probe is not focused within the device for circuit measurements, but on the adjacent metal interconnects. For testing digital circuits probe beam intensities are kept below ~ 50 mW typically. Probe beam intensities can be reduced by a factor of ten, reducing the photogenerated carrier concentration by a similar factor, without severe degradation of the system sensitivity (Eqn. 23). Residual invasiveness of the probe can also be reduced by increasing the probe beam wavelength from 1.06 to 1.3 μm , where the absorption due to the EL2 deep level is reduced by a factor of 5 [52,53].

4. Circuit measurements

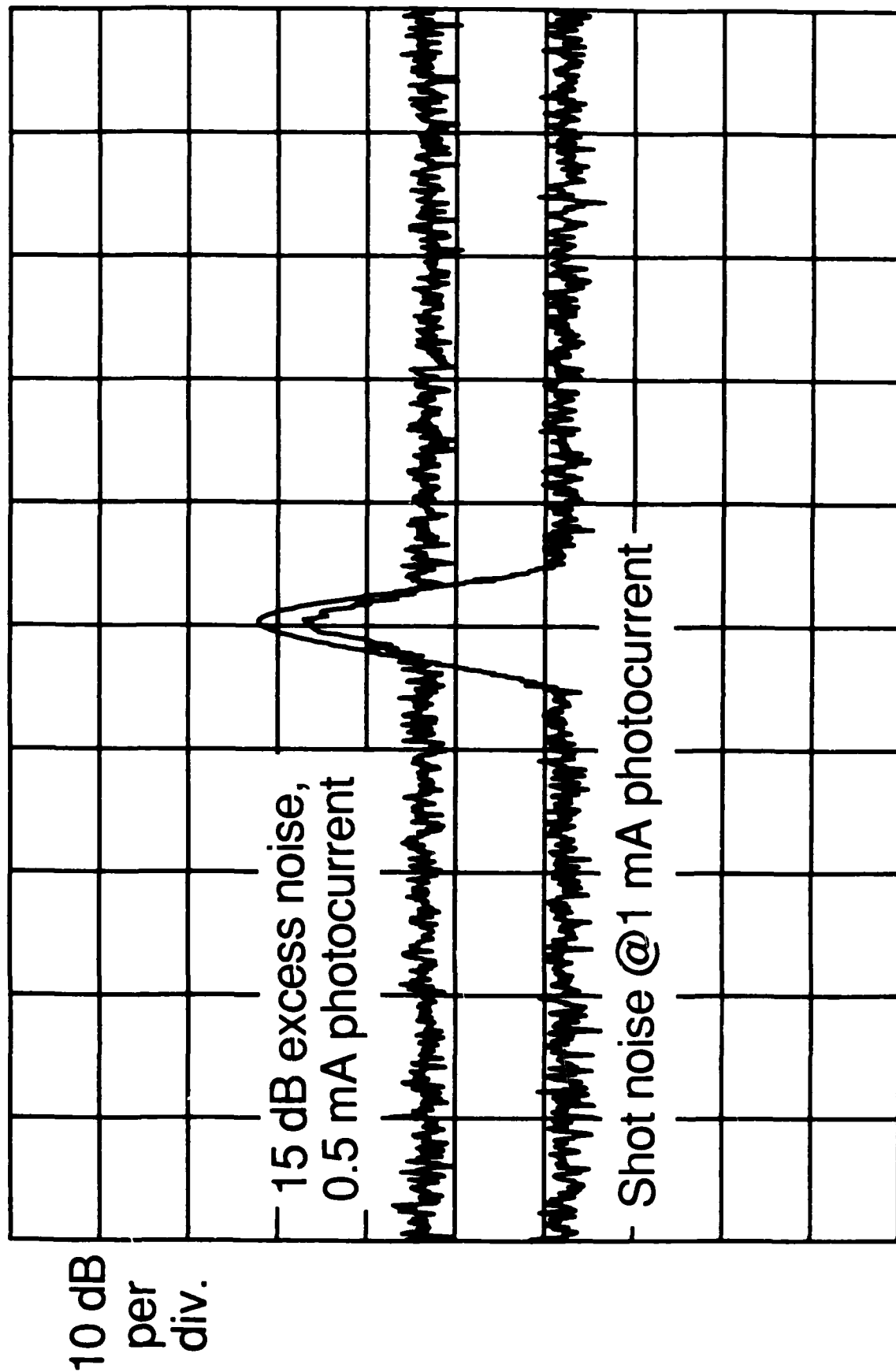
4.1. Realistic circuit testing conditions

Optical probing, providing access to the high-impedance internal nodes of IC's with picosecond time resolution and micron spatial resolution, permits direct measurements of the performance of state-of-the-art microwave and digital GaAs circuits. To permit meaningful evaluations of a circuit's performance and to provide meaningful comparisons between competing circuit technologies, these measurements must be made under realistic circuit operating conditions



Center 10 MHz 5 kHz/div Resolution 1 KHz

Figure 21: Periodic noise spectrum indicative of a parasitic fiber-Raman laser for the pulse compressor operated near the stimulated Raman threshold.



Center 10 MHz 5 kHz/div Resolution 1 KHz

Figure 22: Excess amplitude noise due to misadjustment of the polarization from the output of the pulse compressor fiber.

The propagation delay of switching devices in simple test circuits, measured by either electrooptic sampling or by conventional methods, are used to project the maximum clock frequency of these devices used in digital systems. Unless the test circuit provides representative switching voltages, interface impedances, and fan-outs, the measured delays will not correlate well with the maximum clock frequency of circuits such as shift registers, binary multipliers, and memory. For example, the response of a transistor driven by a low-impedance photoconductor and loaded by a low-impedance, 50 Ω transmission line is in general much faster than the response of a logic gate driven by the normal output impedance of a driving gate and loaded by the normal input capacitances of cascaded gates. If the test circuit is constructed in hybrid form with wire bonds between the tested device and the transmission lines, the interconnect parasitics may dominate the circuit response.

Ring oscillators and inverter strings, the simplest digital test structures, are often used as benchmarks of circuit speed. These circuits load the gates with unity fan-out and tend to give optimistically small delay measurements. Ring oscillators often operate small-signal, without full logic-level swings, while inverter strings operate with full logic-level swings. Master-slave flip-flops, connected as binary frequency dividers, operate with logic signal levels and with each gate loaded by a fan-out of two, and serve as better performance indicators.

For microwave/analog circuits such as distributed amplifiers, appropriate test signals are swept-frequency sinusoids for small-signal transfer function measurements, or single-frequency signals set to larger amplitudes for large-signal and saturation measurements. Signal sources and terminations should have 50 Ω impedances to eliminate source and load reflections.

4.2. Digital circuit measurements

Ring oscillators provide a measure of a gate delay from the rate of a free-running signal propagating around an odd-numbered ring of inverters, i.e. the repetition period corresponds to product of the average gate delay and the number of gates. These free-running circuits are not readily clocked with an external signal, making synchronization to the probe pulses for electrooptic sampling difficult. Inverter chains, however, consisting of series of cascaded inverting logic gates, must be clocked with an external signal, permitting the synchronization of probe pulses for electrooptic measurements and assuring full logic-level switching of the gates. Typically, average gate delays are measured with sampling oscilloscopes; the propagation delay of the entire chain is measured and divided by the number of inverters to obtain the average delay of an individual inverter. For electrooptic testing the input inverter is switched with a microwave synthesizer, generating a square wave that ripples through the test structure. The first several inverters condition the input signal, sharpening the switching transients until the signal risetimes and falltimes reach a steady-state value. The optical probe is then positioned from node-to-node, measuring directly the propagation delays and signal risetimes at gate input and output nodes and at nodes internal to the gate.

Fig. 23 shows a gate delay measurement on an inverter chain implemented in 1 μm gate-length buffered-FET logic MESFETS, with Fig. 24 showing an SEM picture of one inverter. The delay between curves A and B of Fig. 23 is the propagation delay of the inverting common-source stage, 60 ps, while the delay between curves B and C is the delay of the source-follower buffer and diode level-shifter, 15 ps. The inverter chain from Lawrence Livermore National Labs [54] consisted of 20 gates each with a fan-in and fan-out of unity.

The timing of inverter chains has also been examined by Zhang, *et al.* [55], optically triggering an inverter in the chain and using electrooptic sampling to measure the circuit response and gate propagation delays in a pump/probe configuration. A frequency-doubled portion of the probe beam (at $\lambda=532$ nm) focused on the gate region of a FET

photoconductively generates carriers, turning on the FET and generating a switching transient that propagates down the test structure. The probe beam, positioned at a node after the switched gate, is successively delayed with respect to the switching pulse to map the transient waveform. This technique offers an all-optical approach, avoiding microwave connection to the IC, which is suitable for testing of simple IC test structures. However, optical triggering is an impractical method for generating the multiple clock and data signals required to drive large scale IC's.

A higher-level test circuit for IC performance is the static frequency divider, consisting of two flip-flops in a master-slave divide-by-two arrangement [4]. The maximum clock frequency of the divider, set by the propagation delays through the master-slave feedback path, provide an indirect measure of the devices' speed. Testing this circuit is normally accomplished by increasing the clock rate of the divider until its divide-by-two output fails.

The schematic of such a frequency divider is shown in Fig. 25. The circuit, from Hughes Research Laboratories (see Fig. 26), uses 0.2 μm e-beam written gates, molecular-beam epitaxy grown channels, air-bridge interconnects, and optimized feedback to achieve high frequency clock rates. The dividers were implemented in two circuit families, buffered-FET logic (BFL) and capacitively enhanced logic (CEL). Conventional testing, using transmission line probes to drive the circuit and monitor its output on a spectrum analyzer indicated correct circuit operation to 18 GHz. However, the spectrum analyzer gives inconclusive evidence of correct divider operation, since it measures only the output frequency and not the time waveforms. By direct waveform measurements using electrooptic sampling, correct divide-by-two operation was verified, gate propagation delays of 20-30 ps were measured and correlated to maximum clock frequencies (Fig. 27), and the internal delays through the inverting and source-follower stages of individual BFL gates were identified [56]. Note that while the scaled 0.2 μm gate-length FET's had significantly shorter delay through the inverting stage, the delay through the buffer stage was comparable to the 1 μm BFL from LLNL. These data suggest the speed limitation through the buffer stage is no longer *transistor* limited but limited by the resistance-capacitance time constant of the level-shifting diode resistance and the input capacitance of the cascaded gates.

The spatial resolution of the electrooptic sampler permits probing of MSI GaAs digital IC's to determine signal rise-times and relative timing. Fig. 28 shows serial output waveform probed on a 2 μm conductor internal to the output buffer in a 2.7 GHz 8-bit multiplexer/demultiplexer from Tri-Quint Semiconductor [57] and Fig. 29 shows the 8-phase clock waveforms probed on 4 μm metal interconnects. Similar measurements have recently been made on gigahertz logic flip-flops and counters [58].

4.3. Microwave circuit measurements

At microwave and millimeter-wave frequencies, where conductor lengths and circuit element sizes often become large with respect to the electrical wavelength, direct measurements of conductor voltages and currents are difficult, particularly with conventional electrical test instrumentation. Directional couplers and directional bridges separate the forward and reverse waves on a transmission line; standard microwave test instruments use these to measure the incident and reflected waves at the ports of a microwave device or network. The relationship between these waves is expressed as the wave scattering matrix S known as the *scattering parameters* [59]. The electrooptic sampler directly measures voltages, but not currents, preventing a direct measure of 2-port parameters. Measuring the voltage as a function of position with the optical probe [60], similar to a slotted-line measurement, permits calculation of the incident and reverse waves on the transmission lines connecting to devices. From this information the network scattering parameters can then be determined.

AD-A191 379

INSTRUMENTATION FOR ULTRAFAST ELECTRONICS(U) STANFORD
UNIV CA EDWARD L GINZTON LAB OF PHYSICS D M BLOOM
3 NOV 87 AFOSR-TR-88-0000 AFOSR-87-0032

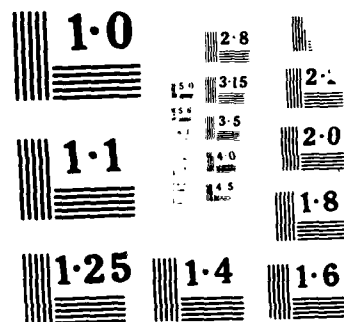
2/2

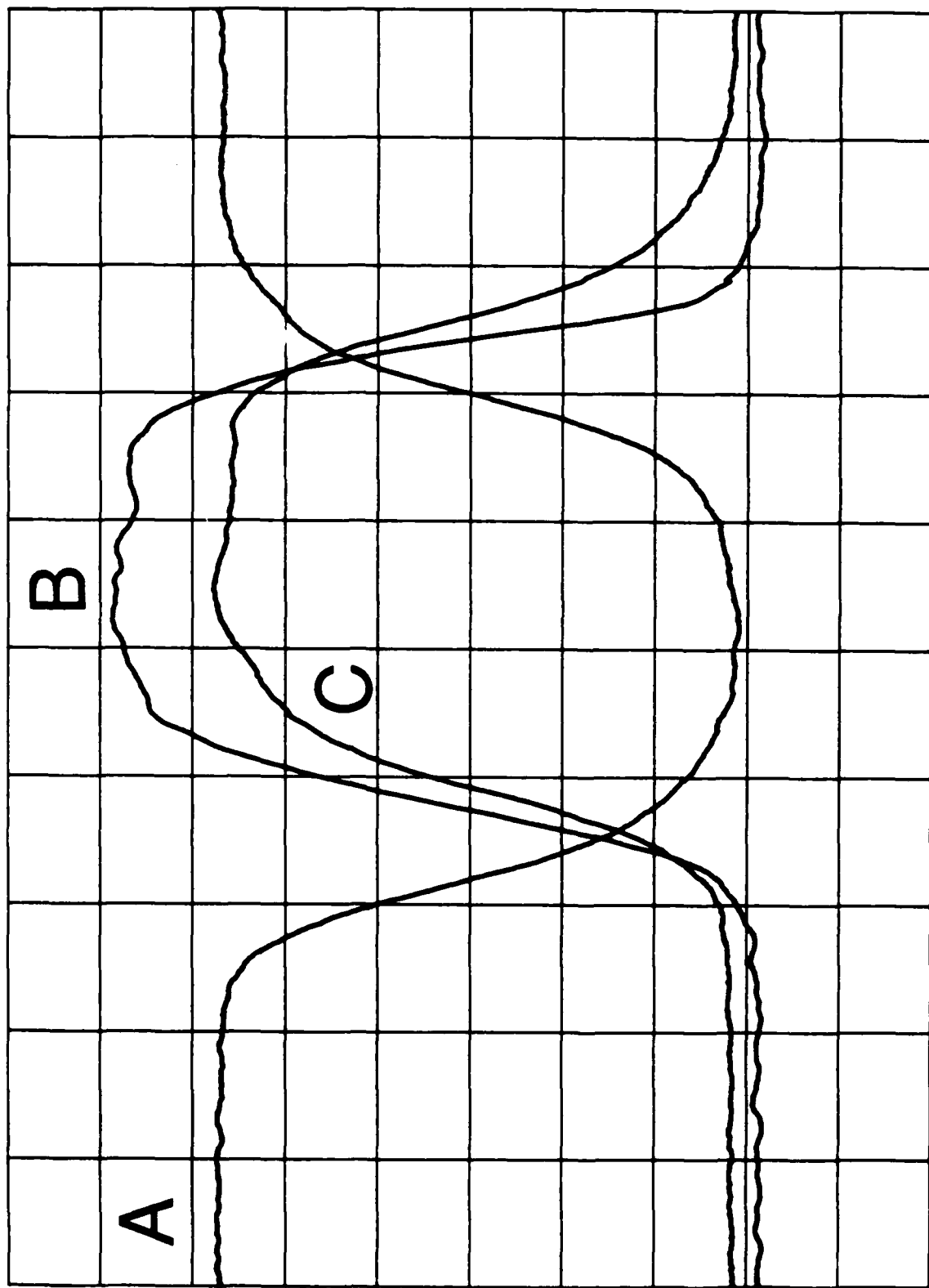
UNCLASSIFIED

F/G 9/1

NL







100 ps/div

Figure 23: Voltage waveforms at the input (a), source-follower gate (b), and output (c) of GaAs buffered-FET-logic inverter gate [46].

GAS SAM2
INV 12 MICRON

B

A

C

052115 25KV X1.00K 30um

Figure 24: A single inverter within the buffered-FET-logic inverter chain [54]. Photo courtesy S. Swierkowski, Lawrence Livermore National Labs.

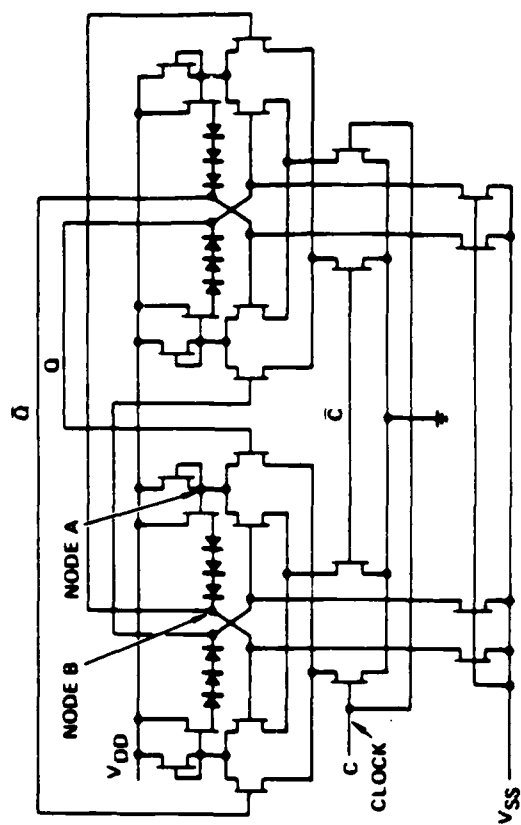


Figure 25: Schematic diagram of a static frequency divider using buffer-FET logic. The labeled points refer to the electrooptically measured data in Fig. 27

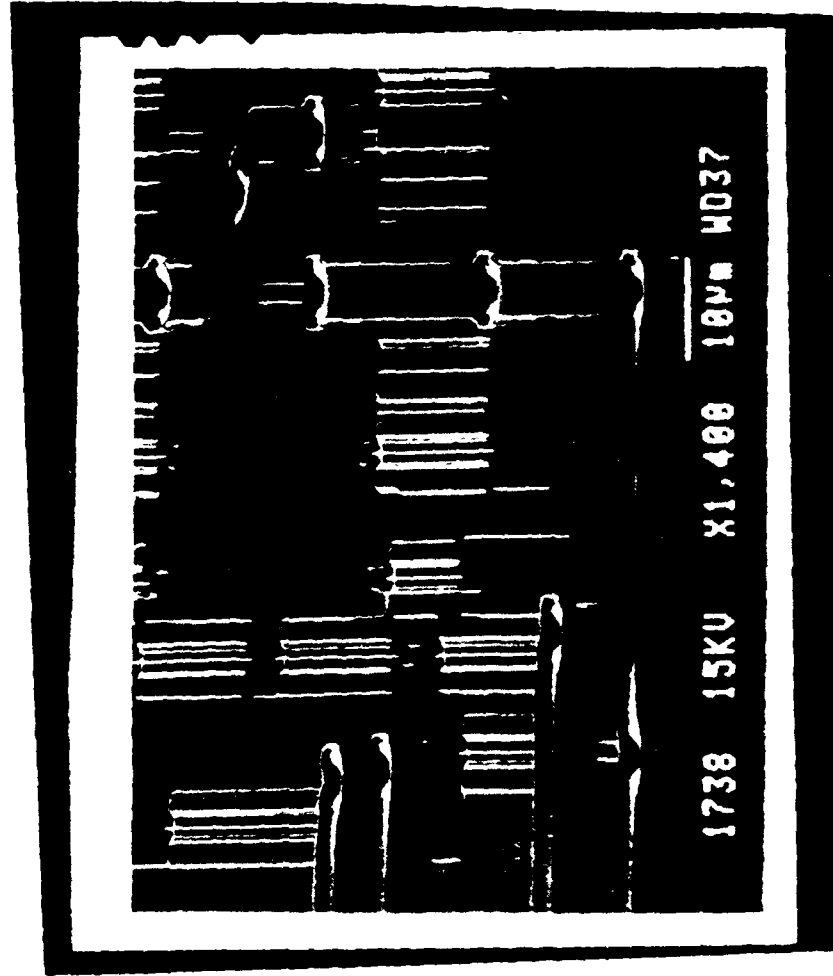


Figure 26: Scanning-electron microscope picture of a section of an 18 GHz static frequency divider [4], courtesy of J.F. Jensen, Hughes Research Laboratories. The circuit uses 0.2 μm e-beam written gates, molecular-beam epitaxy-grown channels, air bridge lines to reduce interconnect capacitance, and optimized feedback to achieve high frequency clock rates

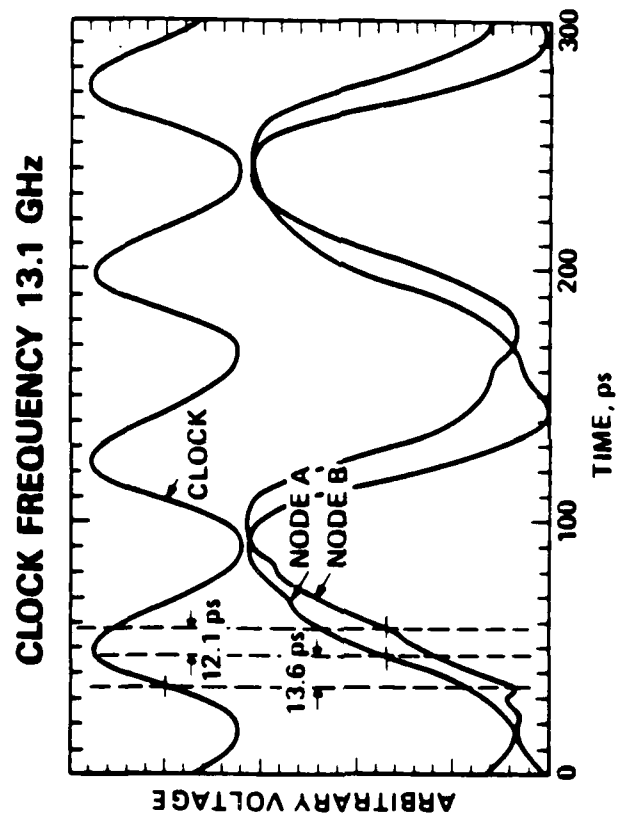
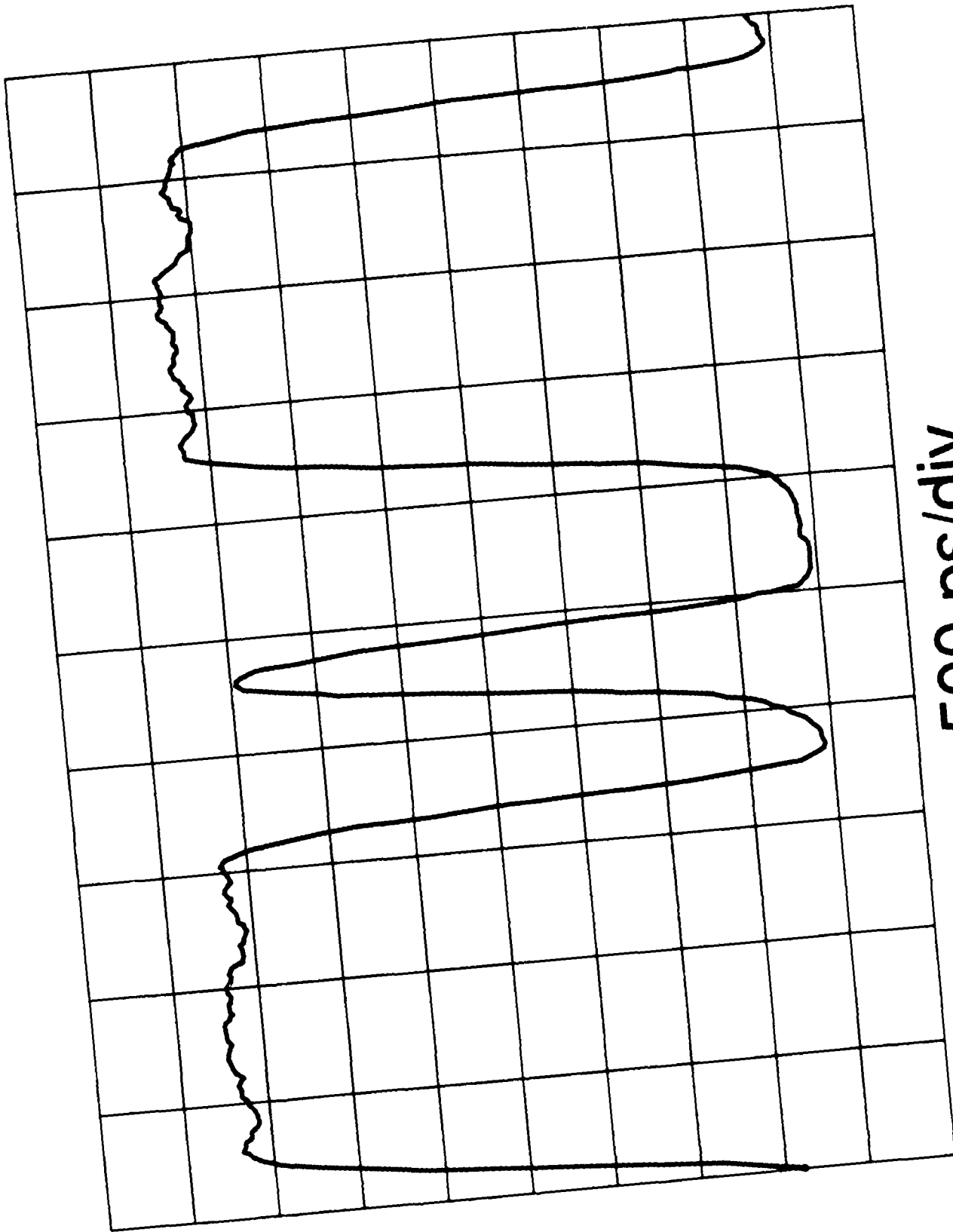
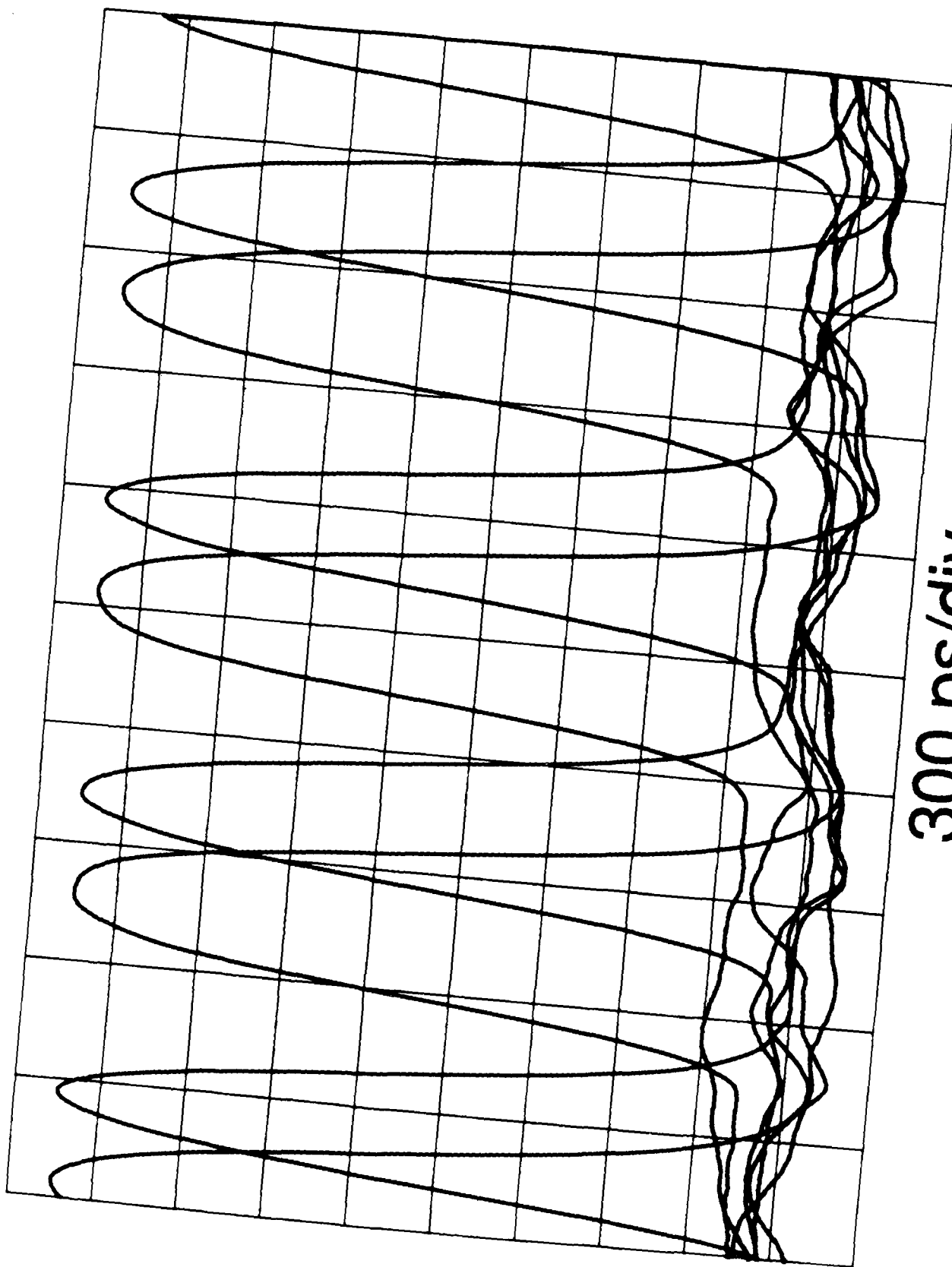


Figure 27: Clock signal and divide-by-two waveforms measured with direct electrooptic sampling. The test points are indicated in Fig. 25.



500 ps/div

Figure 28: Serial output waveform of a 2.7 GHz, 8-bit multiplexer/demultiplexer[57] measured by electrooptic sampling. The output word is 1110100.



300 ps/div

Figure 29: 8-phase clock waveforms in 2.7 GHz multiplexer. An asymmetrical 2.7 GHz clock input results in timing skew in the 8-phase counter.

The vector voltage due to the sum of the forward and reverse traveling waves on a lossless transmission line conductor is

$$V(z) = V^+ \exp(-j\beta z) + V^- \exp(+j\beta z) \quad (33)$$

where V^+ and V^- are the forward and reverse traveling wave coefficients, β is the wavenumber $2\pi/\lambda$, and z is the position. The traveling-wave coefficients are calculated by measuring this vector voltage as a function of position along a conductor using the optical probe then solving for these coefficients. For a one-port transmission line the ratio of the traveling wave coefficients V^+ and V^- is the reflection coefficient Γ , or S_{11} , the return loss. An example of such a measured vector standing wave and the calculated reflection coefficient for an unterminated CPW transmission line at a drive frequency of 40 GHz is shown in Fig. 30, and a similar measurement with an unmatched load terminating the line at 20 GHz is shown in Fig. 31. Extending this technique to calculate the incident and reflected waves on the input and output ports of a network allows for calculation of the S-parameters with a reference plane defined on the integrated circuit.

On GaAs microwave amplifiers and similar MMIC's, the propagation of microwave signals internal to the circuit can be measured. Figure 32 is a monolithic 2-18 GHz MESFET distributed amplifier from Varian Research Labs [61,62] with coplanar-waveguide transmission line interconnects. The circuit diagram is shown in Fig. 33. In a distributed amplifier, a series of small transistors are connected at regular spacings between two high-impedance transmission lines. The high-impedance lines and the FET input and output capacitances together form synthetic transmission lines of 50 Ω characteristic impedance. Series stubs are used in the drain circuit, equalizing the phase velocities of the two lines and providing partial matching between the low impedance of the output line and the higher output impedances of the FET's at high frequencies, thereby peaking the gain. Measurements of interest include the relative drive levels to the individual FET's as influenced by the loss and cutoff frequency of the synthetic gate line, the small-signal voltage at the drain of each FET, and identification of the saturation mechanisms leading to amplifier gain compression.

Figure 34 shows the small-signal gate voltages versus frequency for the amplifier of Fig. 32; several features can be noted. The rolloff beyond 18 GHz is the cutoff frequency of the periodically-loaded gate line, the slow rolloff with frequency is the gate line attenuation arising from the real part of the FET input admittance, and the ripples are standing waves resulting from mistermination of the gate line (i.e. the load resistance not equal to the synthetic line's characteristic impedance.)

Similar measurements can be made on MMIC's using microstrip transmission lines. Figures 35 and 36 show the small-signal drain voltages versus frequency for a distributed amplifier with microstrip transmission lines (Fig. 37, also from Varian Associates.) The strong variation with frequency and position results from interference of the forward and reverse waves on the drain transmission line.

Used in the synchronous sampling mode, the electrooptic sampler can measure the voltage waveforms at internal nodes under conditions of circuit saturation, permitting identification of the saturation mechanisms. Figure 38 shows the voltage waveforms at drains 4 and 5 of the microstrip distributed amplifier operating at 10 GHz and 7 dBm input power, corresponding to the 1 dB gain compression point. For this amplifier, at frequencies above 5 GHz, gain saturation arises predominantly from drain saturation (i.e. reduction of V_{dg} to the point where the drain end of the channel is no longer pinched off) of the fourth and fifth FET's. Saturation at drive frequencies as high as 21 GHz can be observed (Fig. 39). Even if the probed points had been accessible with electrical probes, these measurements would not be pos-

sible with sampling oscilloscopes (due to limited bandwidth), spectrum analyzers (magnitude response only), or network analyzers (small-signal response only).

5. Conclusion

A variety of new probing techniques for high-speed integrated circuits have been investigated, with the objective of providing an instrument with bandwidth greater than that of the tested device, a spatial resolution sufficient to permit access to finely spaced conductors within these circuits, measuring their potential independent of the potential of nearby conductors, and with negligible degradation of measurement accuracy from circuit perturbation. The techniques discussed in the introduction use either electron or optical beams to measure electrical signals on an IC, and all have some degree of tradeoff between achieving best time resolution, spatial resolution, and perturbation of the circuit operation. Direct electrooptic sampling uses the substrate of the GaAs IC itself as the electrooptic modulator, eliminating external electrooptic elements and their invasive aspects, and permitting access to arbitrary points within the circuit without physical contact to a resolution limited by the diameter of the focused infrared probe beam. With the substrate serving as the electrooptic element, the optical properties of the circuit must be considered (polishing of the substrate backside and metallization reflectivity), and probe beam absorption through deep levels in the GaAs substrate may affect circuit operation. Reducing the probe beam intensity or using a longer wavelength beam reduces this perturbation. The sections on system bandwidth and sensitivity describe limits on the instrument's time resolution and accuracy. Since the intensity modulations due to the electrooptic effect are small, full understanding of the noise sources in the system and methods for their suppression is crucial if the system is to provide useful circuit measurements. The resulting system has a time resolution of less than 2 ps, a corresponding bandwidth greater than 100 GHz, a sensitivity of $70 \mu\text{V}/\sqrt{\text{Hz}}$, and a spatial resolution of less than 3 microns.

The direct electrooptic sampling system has several aspects critical for IC testing in addition to internal node testing. Synchronization of the laser probe pulses to the signal generator driving the IC permits operation of the circuit in its normal fashion, driven by microwave or digital signals from electronic sources. Integration of the electrooptic sampling system with a microwave wafer probe station permits wafer-level optical probing of high-speed IC's. Measurement results on a variety of GaAs analog microwave and high-speed digital integrated circuits have been presented, such as gate propagation delay and logic timing measurements of an 8-bit multiplexer/demultiplexer clocked at 2.6 GHz, a 20 gate inverter chain using $1\mu\text{m}$ MESFET technology, 18 GHz static frequency dividers using $0.2 \mu\text{m}$ MESFET technology on digital IC's, internal signal measurements on 2-18 GHz microstrip and coplanar waveguide traveling-wave amplifiers, and voltage standing wave and reflection coefficient measurements on transmission lines at frequencies to 40 GHz. Extending the standing-wave measurements to two-port devices will permit on-wafer millimeter-wave scattering parameter measurements with the reference planes located at the device terminals on the IC.

6. Acknowledgments

The authors thank J.F. Jensen of Hughes Research Laboratories (Malibu), M. Riazat of Varian Research Center, K.R. Gleason of Cascade Microtech and TriQuint Semiconductor, Inc., and S. Swierkowski of Lawrence Livermore National Labs for their assistance with the GaAs circuits. Thanks to T. Baer and J.D. Kafka of Spectra-Physics, inc., for their assistance with the optical pulse compressor. We acknowledge the generous equipment donations of Cascade Microtech, Inc., Tektronix, Inc, and the Hewlett-Packard Co. K.J. Weingarten acknowledges a Newport Research Award and M.J.W. Rodwell acknowledges an IBM Pre-doctoral Fellowship. Our research was sponsored by the Air Force Office of Scientific Research under grant F49620-84-K-0139, by the Joint Services Electronic Program under grant N00014-84-K-0327, and by Wright-Patterson Air Force Base Avionics Laboratory under contract F33615-86-C-1126.

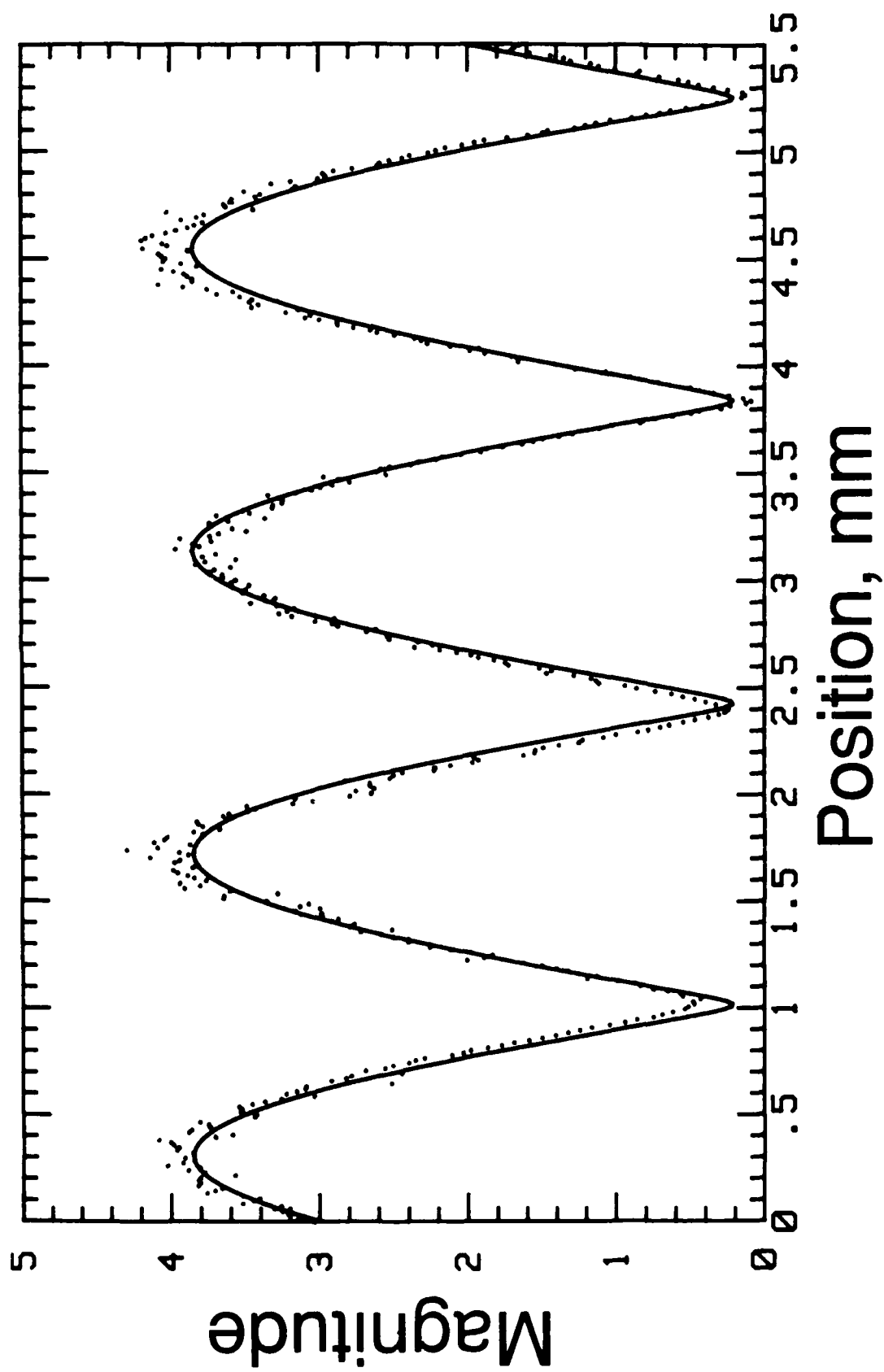
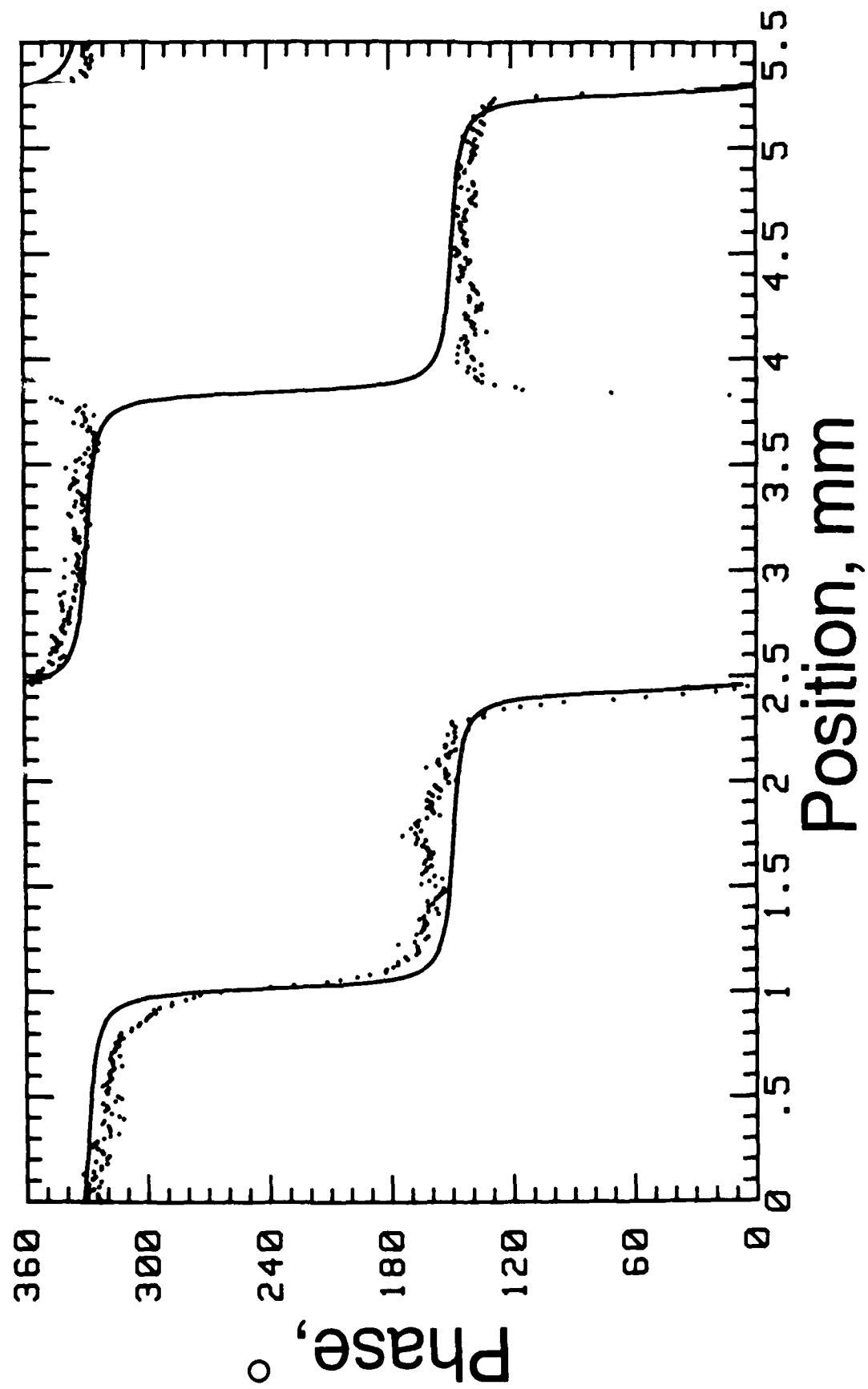


Figure 30: Magnitude (a) and phase (b) of a 40 GHz voltage standing wave on an open-terminated GaAs coplanar waveguide transmission line. The points are the data and the solid line is the fitted curve. From this measurement a reflection coefficient of 0.90 @ -80° is calculated. Each division of 10° in phase corresponds to 0.7 ps in time.



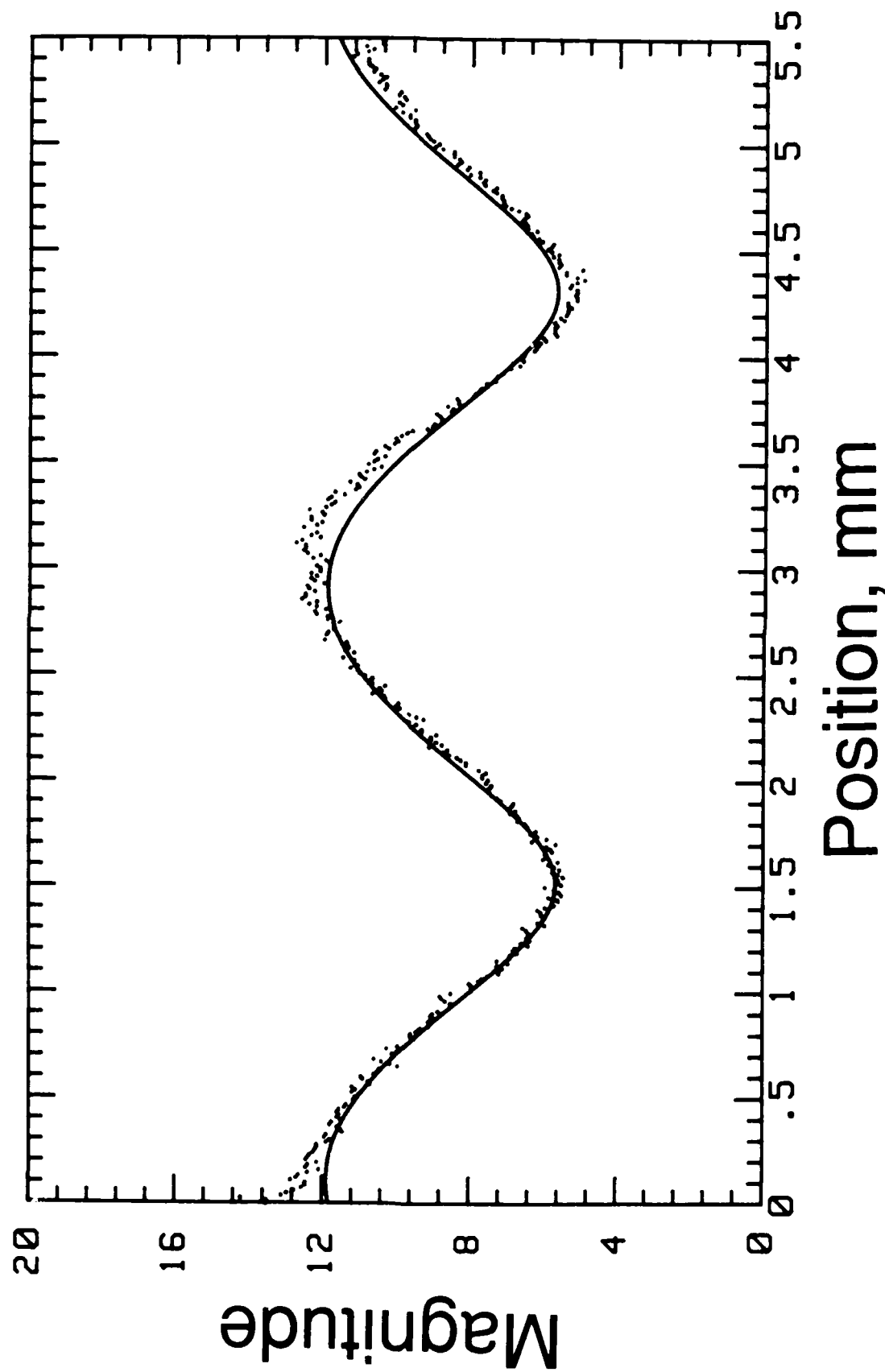
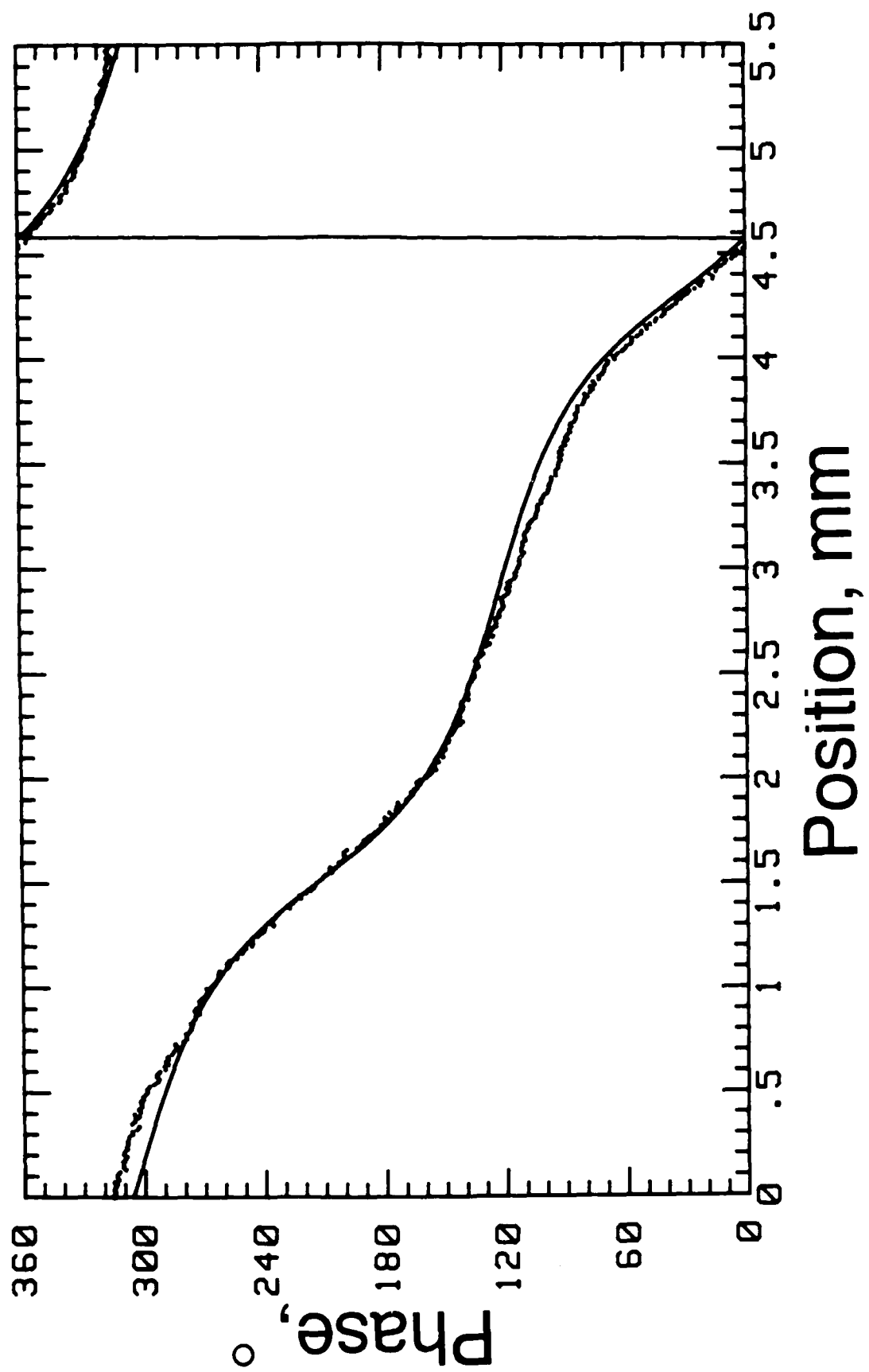


Figure 31: Magnitude (a) and phase (b) of a 20 GHz voltage standing wave on a GaAs coplanar waveguide transmission line with a mismatched termination. The points are the data and the solid line is the fitted curve. From this measurement a reflection coefficient of 0.35 @ -15° is calculated.



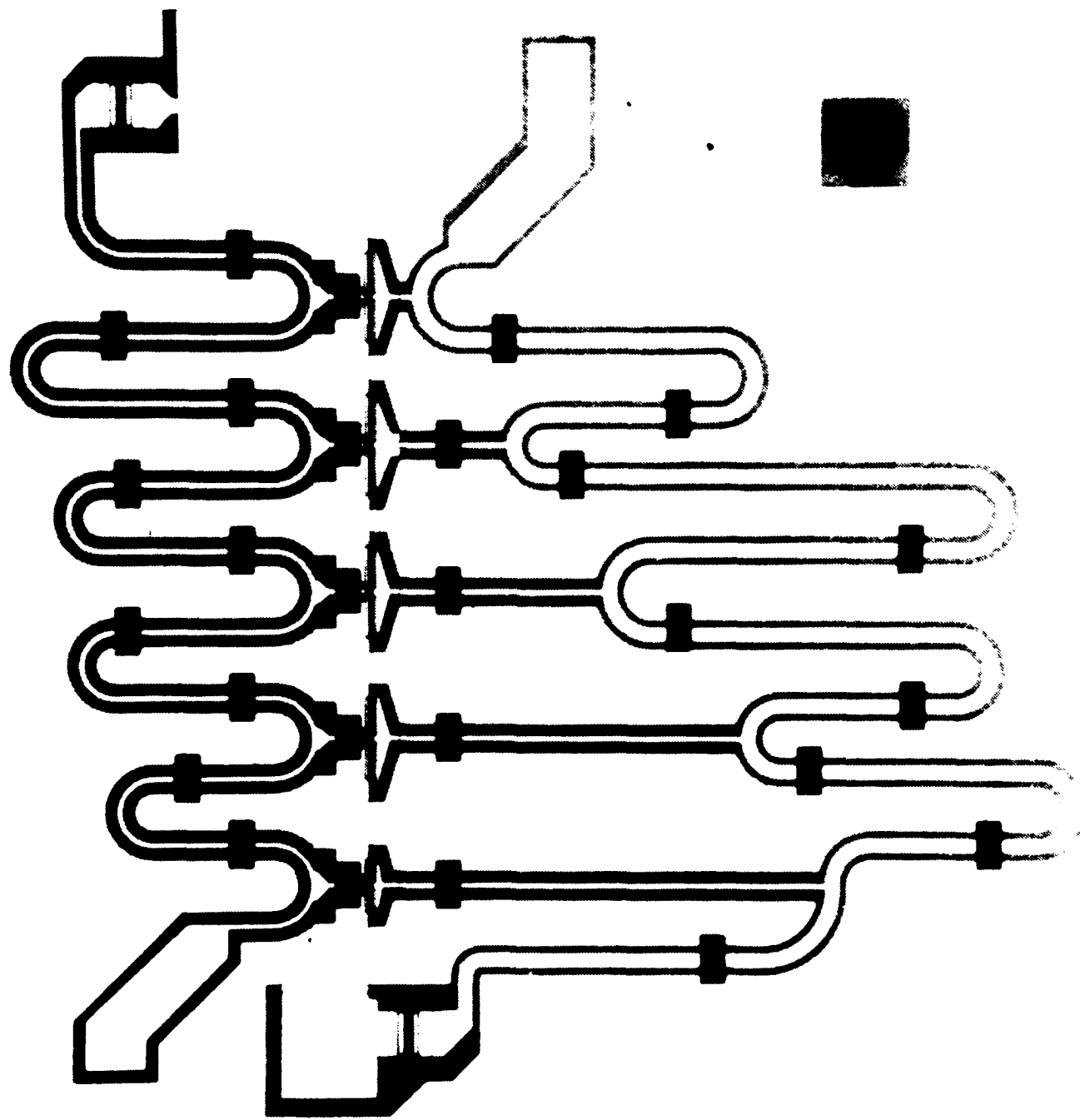


Figure 32: Traveling-wave amplifier using coplanar waveguide transmission-line interconnects [62].
Photo courtesy of M. Riazat, Varian Research Center.

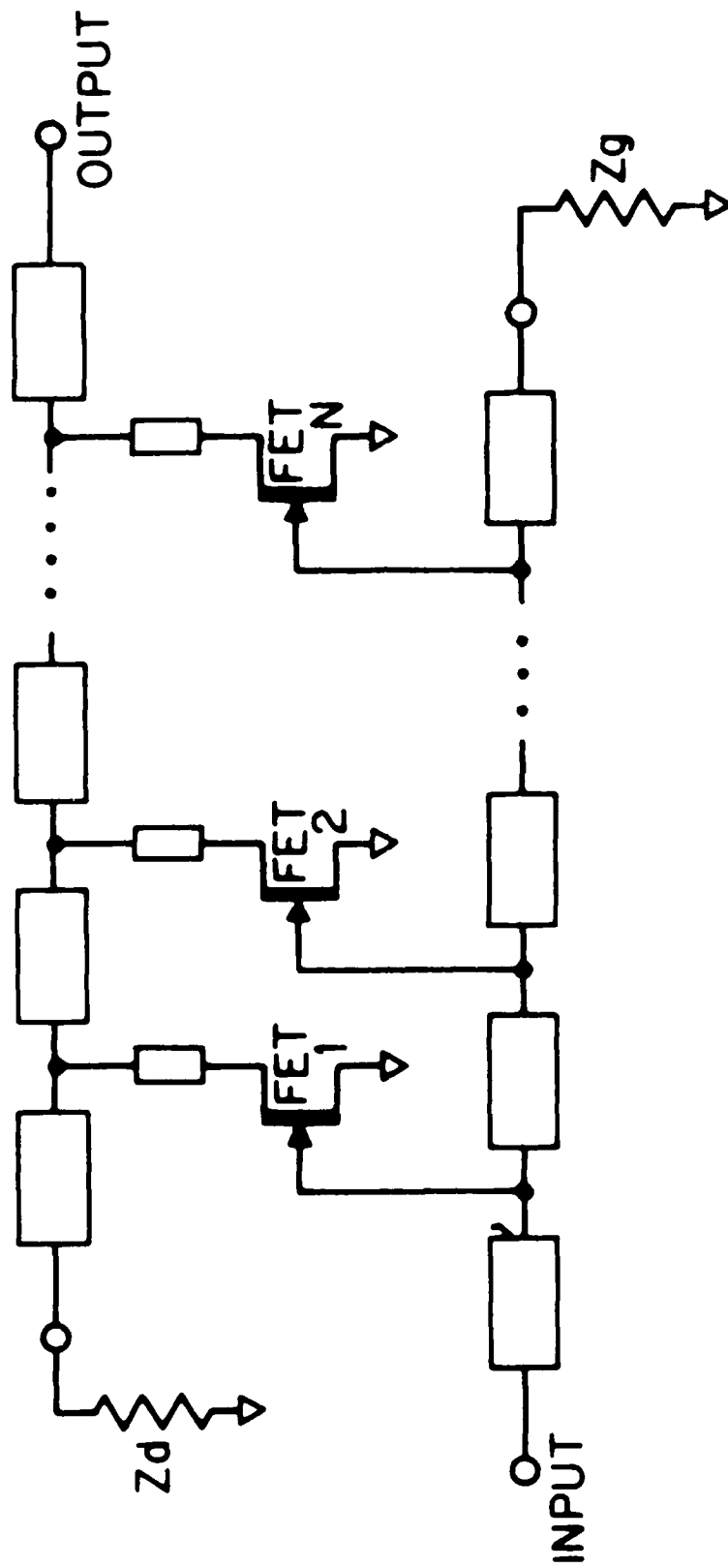


Figure 33: Circuit diagram of distributed amplifier.

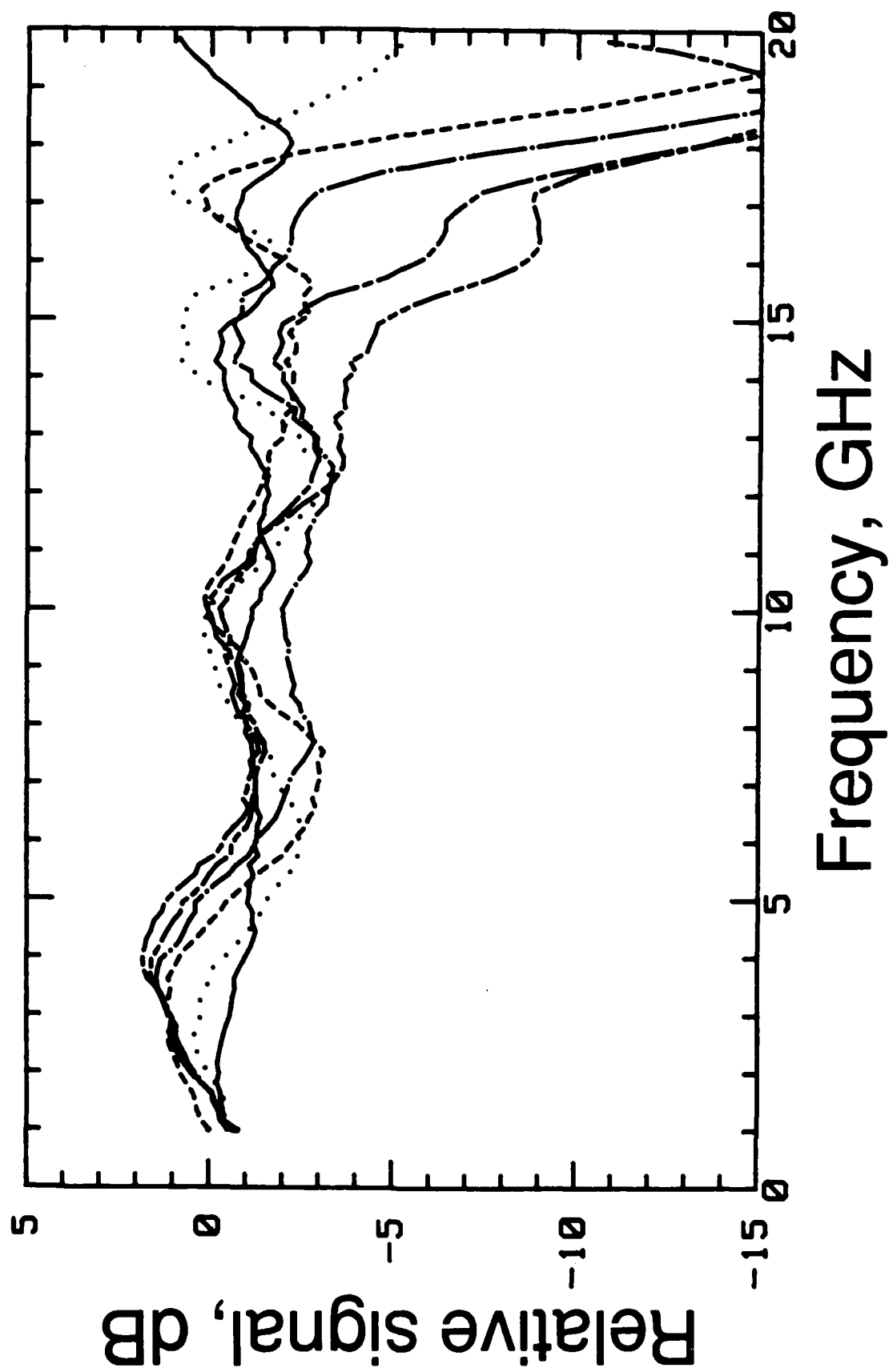


Figure 34: Small-signal voltages at the five gates and at the gate line termination resistor in the coplanar 2-18 GHz distributed amplifier of Fig. 23.

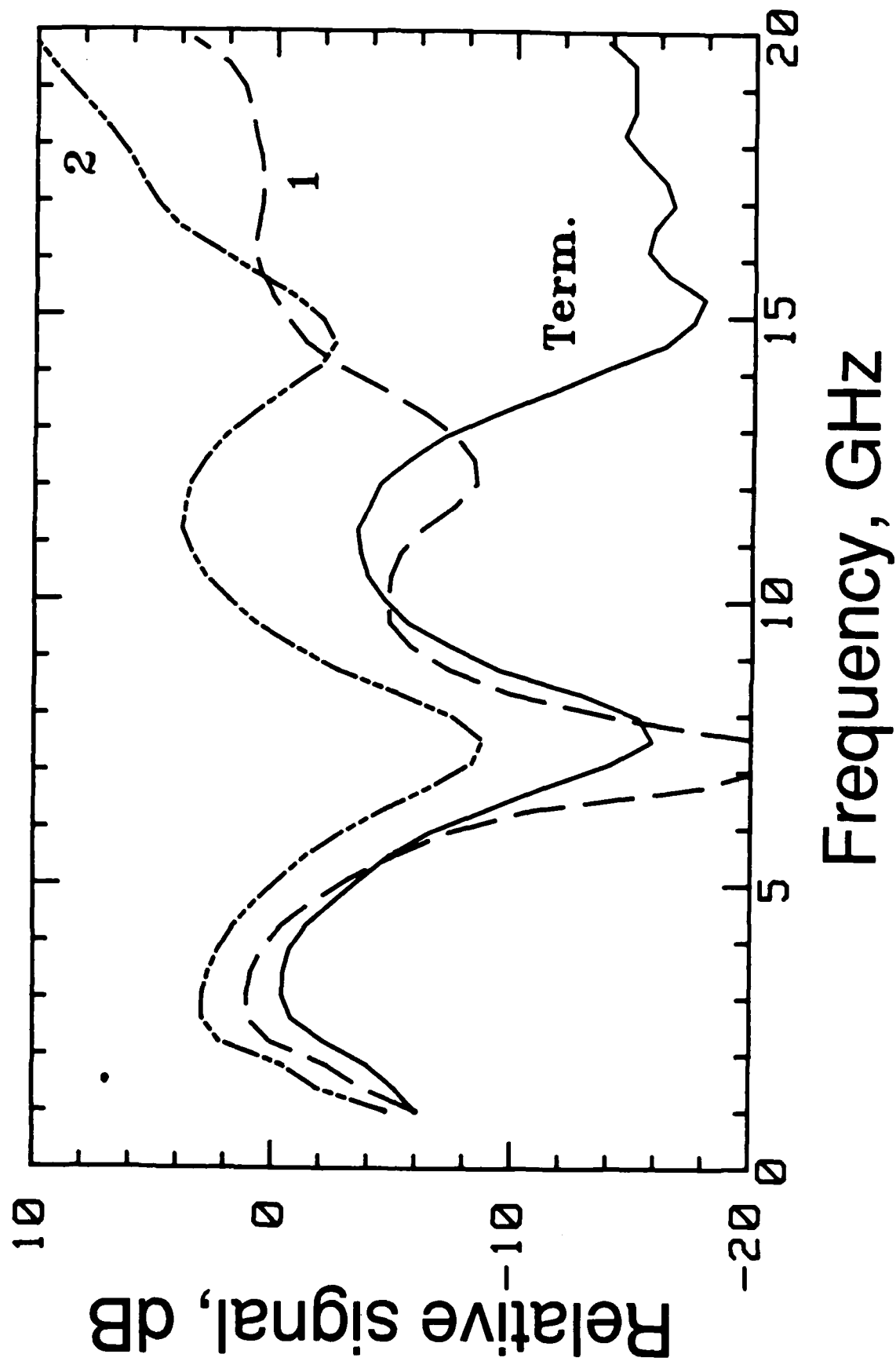


Figure 35: Small-signal voltages at the first and second drains, and at the drain line reverse termination resistor, in a 2-18 GHz distributed amplifier using microstrip transmission lines [61].

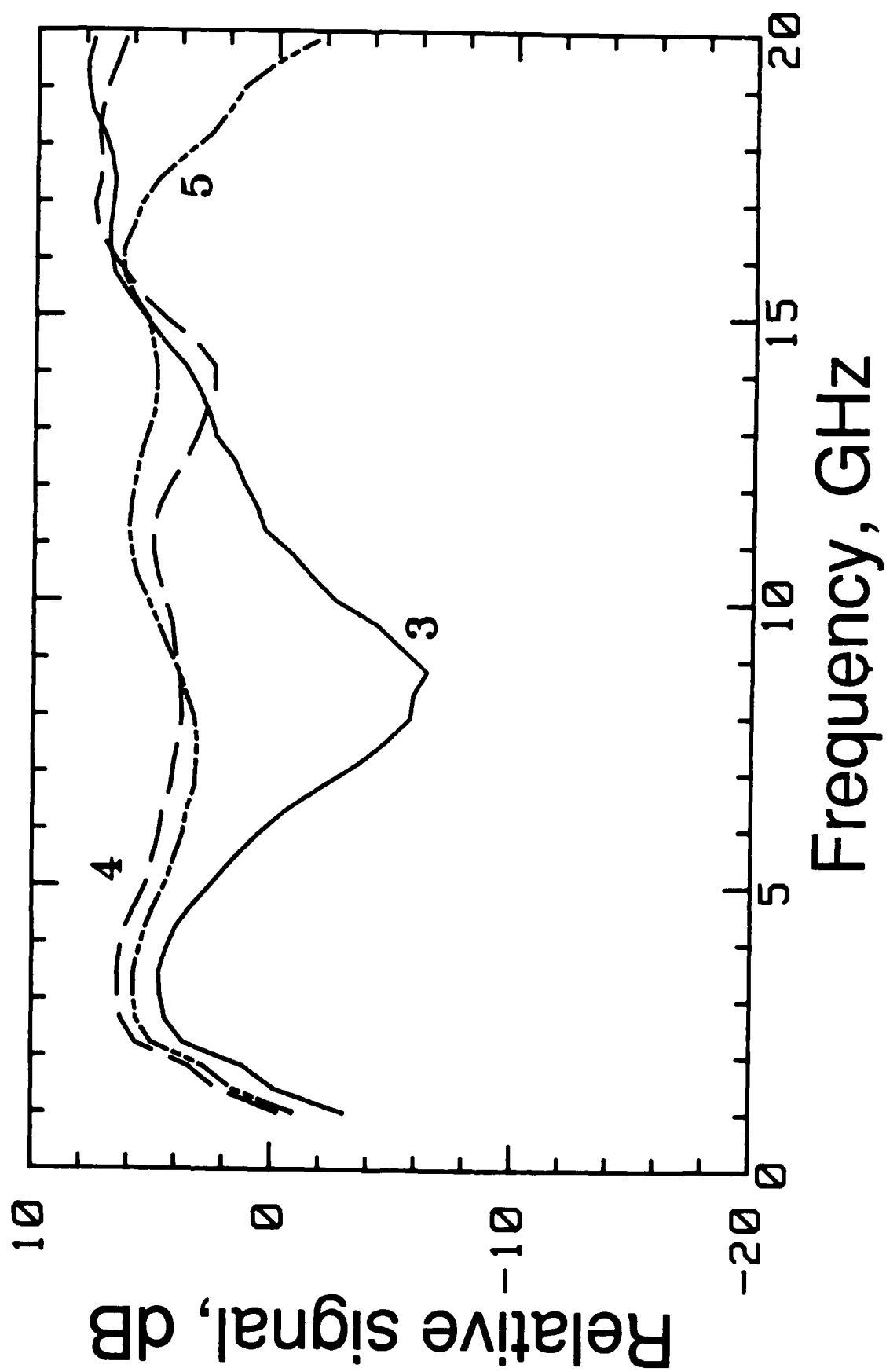


Figure 36: Small-signal voltages at drains 3, 4, and 5 of the microstrip distributed amplifier.

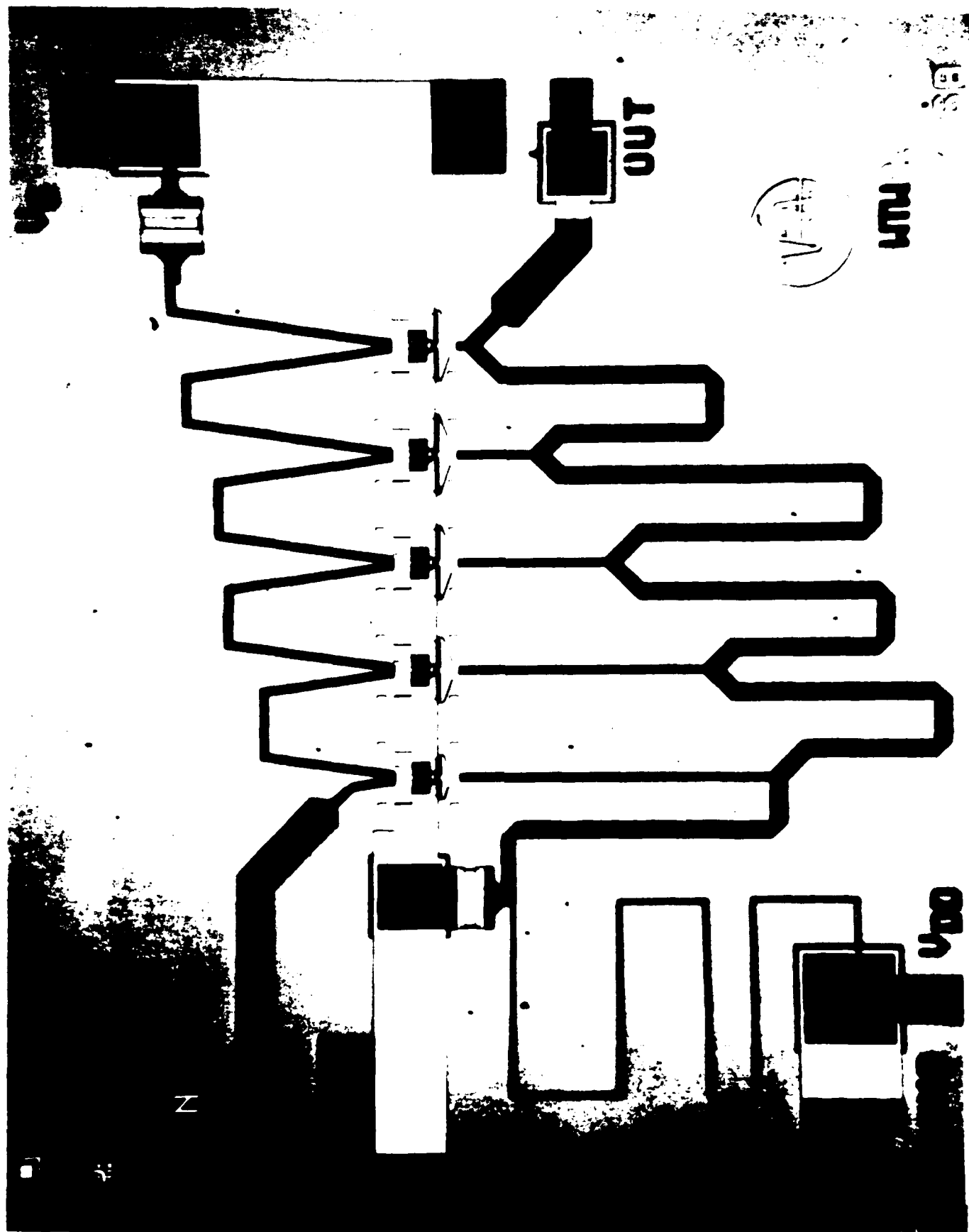


Figure 37: Traveling-wave amplifier using microstrip transmission line interconnects [62]. Photo courtesy of R. LaRue, Varian Research Center.

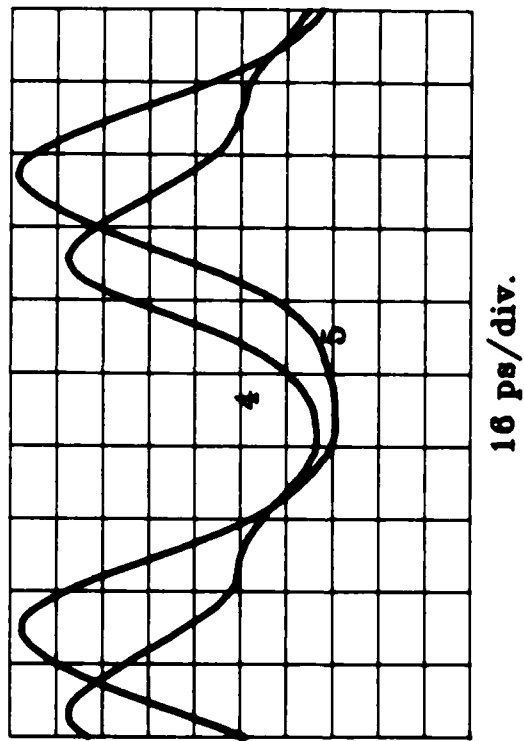
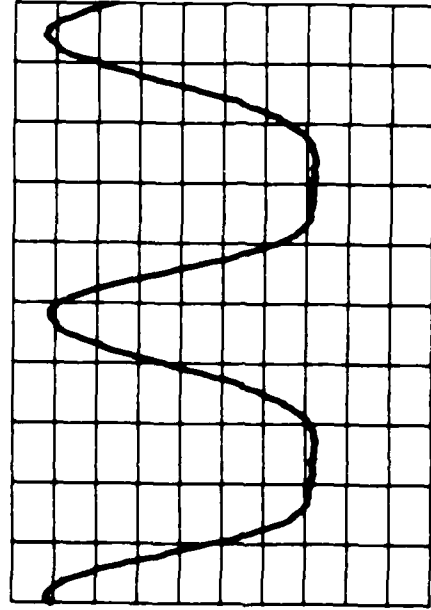


Figure 38: Saturation at drains 4 and 5 of the microstrip distributed amplifier at 10 GHz and 7 dBm input power, the 1 dB gain compression point.



10 ps/div.

Figure 39: Saturation at drain 3 of the microstrip distributed amplifier at 21 GHz drive frequency.

7. References

1. H.Q. Tserng and B. Kim: "110 GHz GaAs FET Oscillator," *Elec. Lett.*, vol. 21, pp. 178-179, 1985
2. T. Henderson, M.I. Aksun, C.K. Peng, Hadis Morkoc, P.C. Chao, P.M. Smith, K.-H. G. Duh, and L.F. Lester: "Microwave performance of a Quarter-Micrometer Gate Low-Noise Pseudomorphic InGaAs/AlGaAs Modulation-Doped Field Effect Transistor," *IEEE Elect.Dev. Lett.*, vol. EDL-7, pp. 649-651, 1986
3. T.C.L.G. Sollner, E.R. Brown, W.D. Goodhue, and H.Q. Le: "Observation of millimeter-wave oscillations from resonant tunneling diodes and some theoretical considerations of ultimate frequency limits", *Appl. Phys. Lett.*, vol. 50, pp. 332-334, 1987
4. J.F. Jensen, L.G. Salmon, D.S. Deakin, and M.J. Delaney: "Ultra-high speed GaAs static frequency dividers," Technical Digest of the 1986 International Electron Device Meeting, p. 476-479
5. E.W. Strid, K.R. Gleason, and T.M. Reeder: "On-wafer measurement of gigahertz integrated circuits," *VLSI Electronics: Microstructure Science, Vol 11*, New York: Academic Press, 1985, pp. 265-287
6. Cascade Microtech, Inc., P.O. Box 2015, Beaverton, OR 97075
7. Hypres, Inc., 175 Clearbrook Rd., Elmsford, NY 10523
8. "Electron-beam testing of VLSI chips gets practical," *Electronics*, March 24, 1986, pp. 51-54
9. R. Iscoff: "E-beam probing systems: filling the submicron gap," *Semiconductor International*, Sept. 1985, pp. 62-68
10. P. May, J.-M. Halbout, and G. Chiu: "Laser pulsed E-beam system for high speed IC testing," to be published in *Picosecond Electronics and Optoelectronics*, New York: Springer-Verlag, 1987
11. R.B. Marcus, A.M. Weiner, J.H. Abeles, and P.S.D. Lin: "High-speed electrical sampling by fs photoemission," *Appl. Phys. Lett.*, vol. 49, pp. 357-359, 1986
12. J. Bokor, A.M. Johnson, R.H. Storz, and W.M. Simpson: "High-speed circuit measurements using photoemission sampling," *Appl. Phys. Lett.*, vol. 49, pp. 226-228, 1986
13. A.M. Weiner, R.B. Marcus, P.S.D. Lin, and J.H. Abeles: "Photoemissive testing of high-speed electrical waveforms," to be published in *Picosecond Electronics and Optoelectronics*, New York: Springer-Verlag, 1987
14. H.K. Heinrich, D.M. Bloom, and B.R. Hemenway: "Noninvasive sheet charge density probe for integrated silicon devices," *Appl. Phys. Lett.*, vol. 48, pp. 1066-1068, 1986

-
15. H.K. Heinrich, B.R. Hemenway, K.A. McGroddy, and D.M. Bloom: "Measurement of real-time digital signals in a silicon bipolar junction transistor using a noninvasive optical probe," *Elec. Lett.*, vol. 22, pp. 650-652, 1986
 16. J.A. Valdmanis, G.A. Mourou, and C.W. Gabel: "Picosecond electro-optic sampling system," *Appl. Phys. Lett.*, vol. 41, pp. 211-212, 1982
 17. B.H. Kolner, D.M. Bloom, and P.S. Cross: "Electro-optic sampling with picosecond resolution," *Elect. Lett.*, vol. 19, 574-575, 1983
 18. J.A. Valdmanis, G.A. Mourou, and C.W. Gabel: "Subpicosecond electrical sampling," *IEEE J. Quantum Elect.*, vol. QE-19, 664-667, 1983
 19. J.A. Valdmanis and G. Mourou: "Subpicosecond electrooptic sampling: principles and applications," *IEEE J. Quantum Elect.*, vol. QE-22, pp. 69-78, 1986
 20. D.R. Dykaar, R. Sobolewski, J.F. Whitaker, T.Y. Hsiang, G.A. Mourou, M.A. Hollis, B.J. Clifton, K.B. Nichols, C.O. Bozler, and R.A. Murphy: "Picosecond characterization of ultrafast phenomena: new devices and new techniques," *Ultrafast Phenomena V*, ed. by G.R. Fleming and A.E. Siegman, Springer Ser. Chem. Phys., Vol. 46, New York:Springer-Verlag, 1986 pp. 103-106
 21. J.A. Valdmanis and S.S. Pei: "A non-contact picosecond prober for integrated circuit testing," To be published in *Picosecond Electronics and Optoelectronics*, New York: Springer-Verlag, 1987
 22. J.A. Valdmanis and S.S. Pei: "Picosecond non-contact electrooptic probing for integrated circuits," *Technical Digest of the 1987 Conference on Lasers and Electrooptics*, pp. 352-353
 23. J.A. Valdmanis: Presentation FN3 at the 1987 Conference on Laser and Electrooptics, and private communication
 24. I.P. Kaminow, *An Introduction to Electro-Optic Devices*. New York: Academic Press, 1974
 25. I.P. Kaminow and E.H. Turner: "Electrooptic light modulators," *Proc. IEEE*, 54, 1374-1390 (1966)
 26. B.H. Kolner and D.M. Bloom: "Direct electrooptic sampling of transmission-line signals propagating on a GaAs substrate," *Elect. Lett.*, vol. 20, 818-819, 1984
 27. B.H. Kolner and D.M. Bloom: "Electrooptic sampling in GaAs integrated circuits," *IEEE J. Quant. Elect.*, vol. QE-22, 79-93, 1986
 28. A. Yariv and P. Yeh: *Optical Waves in Crystals*, New York: New York: John Wiley & Sons, Inc, 1984, pp. 286-287
 29. *Ibid*, p. 230

-
30. J.L. Freeman, S.K. Diamond, H. Fong, and D.M. Bloom: "Electrooptic sampling of planar digital integrated circuits," *Appl. Phys. Lett.*, vol. 47, 1083-1084, 1985
 31. W.H. Knox, R.L. Fork, M.C. Downer, R.H. Stolen, and C.V. Shank: "Optical pulse compression to 8 fs at a 5-kHz repetition rate," *Appl. Phys. Lett.*, vol. 46, 1120-1121, 1985
 32. C.H. Brito-Cruz, R.L. Fork, and C.V. Shank: "Compression of optical pulses to 6 fs using cubic phase distortion compensation," *Technical Digest of the 1987 Conference on Lasers and Electrooptics*, pp. 12-13
 33. A.S. Gouveia-Neto, A.S.L. Gomes, and J.R. Taylor: "Generation of 33-fsec pulses at 1.32 μm through a high-order soliton effect in a single-mode optical fiber," *Optics Letters*, vol. 12, 395-397, 1987
 34. B. Zysset, W. Hodel, P. Beaud, and H.P. Weber: "200-femtosecond pulses at 1.06 μm generated with a double-stage pulse compressor," *Optics Letters*, vol. 11, 156-158, 1986
 35. R.N. Bracewell, *The Fourier Transforms and its Applications*, New York: McGraw-Hill, 1978
 36. D. Cotter, "Technique for highly stable active mode-locking," *Ultrafast Phenomena IV*, D.A. ed. by Auston and K.B. Eisenthal, New York: Springer-Verlag, 1984, p. 78-80
 37. M.J.W. Rodwell, K.J. Weingarten, D.M. Bloom, T. Baer, and B.H. Kolner: "Reduction of timing fluctuations in a mode-locked Nd:YAG laser by electronic feedback," *Optics Letters*, vol. 11, 638-640, 1986
 38. E.B. Treacy: "Optical pulse compression with diffraction gratings," *IEEE J. Quant. Elect.*, vol. QE-5, 454-458, 1969
 39. D. Grischkowsky and A.C. Balant: "Optical pulse compression based on enhanced frequency chirping," *Appl. Phys. Lett.*, vol. 41, 1-3, 1982
 40. J.D. Kafka, B.H. Kolner, T. Baer, and D.M. Bloom: "Compression of pulses from a continuous-wave mode-locked Nd:YAG laser," *Opt. Lett.*, vol. 9, 505-506, 1984
 41. A.J. Taylor, J.M. Wiesenfeld, G. Eisenstein, R.S. Tucker, J.R. Talman, and U. Koren: "Electrooptic sampling of fast electrical signals using an InGaAsP injection laser," *Elec. Lett.*, vol. 22, 61-62, 1986
 42. A.J. Taylor, J.M. Wiesenfeld, R.S. Tucker, G. Eisenstein, J.R. Talman, and U. Koren: "Measurement of a very high-speed InGaAs photodiode using electrooptic sampling," *Elec. Lett.*, vol. 22, 325-327, 1986
 43. J.M. Wiesenfeld, R.S. Tucker, A. Antreasyan, C.A. Burrus, and A.J. Taylor: "Electrooptic sampling measurements of high-speed InP integrated circuits," *Appl. Phys. Lett.*, vol. 50, 1310-1312, 1987
 44. J.P. Heritage, R.N. Thurston, W.J. Tomlinson, and A.M. Weiner: "Spectral windowing of frequency-modulated optical pulses in a grating compressor," *Appl. Phys. Lett.*, vol. 47, 87-89, 1985

-
45. N.J. Halas and D. Grischkowsky: "Simultaneous optical pulse compression and wing reduction," *Appl. Phys. Lett.*, vol. 48, 823-825, 1986
 46. M.J.W. Rodwell, K.J. Weingarten, J.L. Freeman, and D.M. Bloom: "Gate propagation delay and logic timing of GaAs integrated circuits measured by electro-optic sampling," *Elect. Lett.*, 22, 499-501, 1986
 47. J.D. Kafka and T. Baer: "Intensity fluctuations in optical pulse compression," *Technical Digest of the 1987 Conference on Lasers and Electrooptics*, pp. 276-277
 48. K.J. Weingarten, M.J.W. Rodwell, and D.M. Bloom: "Picosecond sampling of GaAs integrated circuits," To be published in *Picosecond Electronics and Optoelectronics*, New York: Springer-Verlag, 1987
 49. M.N. Islam, L.F. Mollenauer, and R.H. Stolen: *Ultrafast Phenomena V*, ed. by G.R. Fleming and A.E. Siegman, Springer Ser. Chem. Phys., Vol. 46, New York: Springer-Verlag, 1986, pp. 46-50
 50. J.D. Kafka and T. Baer: "Fiber Raman soliton laser pumped by a Nd:YAG laser," *Optics Letters*, vol. 12, 181-183, 1987
 51. R.M. Shelby, M.D. Levenson, and P.W. Bayer: "Guided acoustic-wave Brillouin scattering," *Phys. Rev. B*, vol. 31, 5244-5252, 1985
 52. G.M. Martin, "Optical assessment of the main electron trap in bulk-semi-insulating GaAs," *Appl. Phys. Lett.*, vol. 39, 747-748, 1981
 53. P. Dobrilla and J.S. Blakemore, "Experimental requirements for quantitative mapping of midgap flaw concentration in semi-insulating GaAs wafers by measurement of near-infrared transmittance," *J. Appl. Phys.*, vol. 58, 208-218, 1985
 54. S. Swierkowski, K. Mayeda, and C. McGonaghy: "A sub-200 picosecond GaAs sample-and-hold circuit for a multi-gigasample/second integrated circuit," *Technical Digest of the 1985 International Electron Devices Meeting*, pp. 272-275
 55. X.-C. Zhang and R. K. Jain: "Measurement of on-chip waveforms and pulse propagation in digital GaAs integrated circuits by picosecond electro-optic sampling," *Elect. Lett.*, vol. 22, 264-265, 1986
 56. J.F. Jensen, K.J. Weingarten, and D.M. Bloom: To be published in *Picosecond Electronics and Optoelectronics*, New York: Springer-Verlag, 1987
 57. G.D. McCormack, A.G. Rode, and E.W. Strid: "A GaAs MSI 8-bit Multiplexer and Demultiplexer," *Proceedings of the 1982 GaAs IC Symposium*, pp. 25-28

-
58. X.-C. Zhang, R.K. Jain, and R.M. Hickling: "Electrooptic sampling analysis of timing patterns at critical internal nodes in GigaBit GaAs multiplexers/demultiplexers," To be published in *Picosecond Electronics and Optoelectronics*, New York: Springer-Verlag, 1987
 59. R.E. Collins, *Foundations of Microwave Engineering*, New York: McGraw-Hill, 1966
 60. K.J. Weingarten, M.J.W. Rodwell, J.L. Freeman, S.K. Diamond, and D.M. Bloom: "Electrooptic sampling of gallium arsenide integrated circuits," *Ultrafast Phenomena V*, ed. by G.R. Fleming and A.E. Siegman, Springer Ser. Chem. Phys., Vol. 46, New York: Springer-Verlag, 1986, pp. 98
 61. M.J.W. Rodwell, M. Riazat, K.J. Weingarten, B.A. Auld, and D.M. Bloom: "Internal microwave propagation and distortion characteristics of travelling-wave amplifiers studied by electro-optic sampling," *IEEE Trans. Microwave Theory Tech.*, vol. MTT-34, 1356-1362, 1986
 62. G. Zdasiuk, M. Riazat, R. LaRue, C. Yuen, and S. Bandy: "Enhanced performance ultrabroadband distributed amplifiers," To be published in *Picosecond Electronics and Optoelectronics*, New York: Springer-Verlag, 1987

END
DATE
FILMED
5-88
DTIC